Rice University

The synthesis, characterization, and application of iron oxide nanocrystals in magnetic separations for arsenic and uranium removal

by

John Thomas Mayo

A THESIS SUBMITTED
IN PARTIAL FULFILLMENT OF THE
REQUIREMENTS FOR THE DEGREE

Doctor of Philosophy

APPROVED, THESIS COMMITTEE:

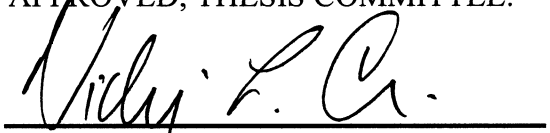

Vicki L. Colvin, Kenneth S. Pitzer-Schlumberger Professor of Chemistry

Mason B. Tomson, Professor of Civil and Environmental Engineering

Kenton H. Whitmire, Professor of Chemistry

HOUSTON, TEXAS
August 2011

ABSTRACT

The synthesis, characterization and application of iron oxide nanocrystals in magnetic separations for arsenic and uranium removal

by

John Thomas Mayo

Arsenic and uranium in the environment are hazardous to human health and require better methods for detection and remediation. Nanocrystalline iron oxides offer a number of advantages as sorbents for water purification and environmental remediation. First, highly uniform and crystalline iron oxide nanocrystals (nMAG) were prepared using thermal decomposition of iron salts in organic solutions; for the applications of interest in this thesis, a central challenge was the adaptation of these conventional synthetic methods to the needs of low infrastructure and economically disadvantaged settings. We show here that it is possible to form highly uniform and magnetically responsive nanomaterials using starting reagents and equipment that are readily available and economical. The products of this approach, termed the 'Kitchen Synthesis', are of comparable quality and effectiveness to laboratory materials. The narrow size distributions of the iron oxides produced in the laboratory synthesis made it possible to study the size-dependence of the magnetic separation efficiency of nanocrystals; generally as the diameter of particles increased they could be

removed under lower applied magnetic fields. In this work we take advantage of this size-dependence to use magnetic separation as a tool to separate broadly distributed populations of magnetic materials. Such work makes it possible to use these materials in multiplexed separation and sensing schemes. With the synthesis and magnetic separation studies of these materials completed, it was possible to optimize their applications in water purification and environmental remediation. These materials removed both uranium and arsenic from contaminated samples, and had remarkably high sorption capacities – up to 12 wt% for arsenic and 30 wt% for uranium. The contaminated nMAG is removed from the drinking water by either retention in a sand column, filter, or by magnetic separation. The uranium adsorption process was also utilized for the enhanced detection of uranium in environmental matrices. By relying on α-particle detection in well-formed and dense nMAG films, it was possible to improve soil detection of uranium by more than ten-thousand-fold. Central for this work was a detailed understanding of the chemistry at the iron oxide interface, and the role of the organic coatings in mediating the sorption process.

ACKNOWLEDGEMENTS

I would like to thank Dr. Vicki L. Colvin, my PhD. advisor and chair of my thesis committee, for valuable instruction and her efforts to provide my research with constant funding. Obviously, without her, none of this would be possible. I would also like to thank Dr. Mason B. Tomson and Dr. Kenton H. Whitmire for participating as my thesis committee.

I would like to thank my past and current fellow group members: Dr. Cafer Yavuz, Dr. John Fortner, Dr. Arjun Prakash, Dr. William Yu, Dr. Joshua Falkner, Denise Benoit, Seung Soo Lee, Dr. Huiguang Zhu, Dr. Carolina Avendaño, Dr. Feng Li, Zuzanna Lewicka, Chris Jones, Natalia Gonzalez-Pech, Dr. Jennifer Jamison, Yihua Yu, Dr. Karl Krueger, Dr. Tushar Prasad, Adina Boyd, Elizabeth Quevedo-Contreras, Erika Bryant, Aniway Lomeda, Hema Puppala, Min Jung Cho, Dr. Ali Al-Somali, Dr. Yunping Liu, Dr. Christie Sayes, Dr. Qingbo Zhang, Jackson Myers, Camila Zies, Dr. Junyan Zhang, Jieying Jing, Dr. Jing Li, Dr. Rajeev Wahi, and Dr. Rajesh Rengarajan. I would also like to thank the undergraduate researchers that have contributed to this project: Helen D'Couto, Lauren Harrison, Wayne Lin, Louis Chen, David Morse, Angelina Tran, Arely Cantu, Carmen Sucheki, Jessica Cox, Jennifer Wang, Courtney Payne, Edward Larkin, Andy Caughey, Raymond Verm, Roger Basu, Bertram Shih.

I would like to thank some of my collaborators at Rice University: Dr. Mason B. Tomson, Dr. Douglas Natelson, Dr. Stephan Link, Dr. Sujin Yean, Dr. Lili Cong, Dr. Sungbae Lee, Dr. Alexandra Fursina, Dr. Alexei Tcherniak, Dr. Jesse Farrell, Dr. Heather Shipley, and Dr. Amy Kan. I would also like to thank all of those at Rice University that have given me significant guidance: Teresa Champion, Dr. Jonathan Brege, Dr. Mary McHale, Brittany Oliva, Dr. Gongmin Fu, Ping Zhang, Dr. Bo Chen, Dr. Angelo Benedetto,

Dr. Wenhua Guo, Dr. Rizia Bardhan-Pint, Alvin Orbaek, Dr. Erika Bakota, Dr. Chris Hamilton, Dr. Chris Crouse, Seunghyun Lee, Sophia Phounsavath, Dr. Dell Doyle, Jorge Fallas, Dr. Liling Zeng. I would also like to thank some of the professors at University of St. Thomas, my undergraduate university, for their previous guidance: Dr. Thomas Malloy, Dr. Gerald Gries, Dr. John Palasota, Dr. William Tinnerman, Dr. Michelle Stieger, Fr. Patrick Braden, Dr. Paul Knopp, Dr. Sheila Waggoner, and Dr. Louie Galloway.

I would like to thank my family for always believing in me and for enabling and encouraging me to seek out what I want from this life and not be swayed by what others would want me to do. I feel that even though I have been somewhat isolated from them for these past years, they have been very accommodating to me when I am available to see them. I would specifically like to thank my mother, Rita Mayo, for the dedication of her life to me and for constant guidance with the unfamiliar. I would like to thank my father, Thomas Mayo, for the wisdom that he has taught me throughout my life. I would like to thank my sister, Leslie Tullos, for always thinking of me and never letting her little brother go without when in need. I would especially like to thank Courtney Payne, my loving fiancée, for always being there for me and for tolerating me during my efforts to complete my graduation requirements.

And finally I would like to thank all of the organizations that have provided financial support for my research, without them none of this could be possible: the National Science Foundation through the Center for Biological and Environmental Nanotechnology, the Robert A. Welch Foundation, and the United States Environmental Protection Agency.

TABLE OF CONTENTS

ABSTRACT ii
ACKNOWLEDGEMENTS iv
TABLE OF CONTENTS vi
LIST OF FIGURES AND TABLES ix
DEDICATION xii
CHAPTER 1 : INTRODUCTION 1
1.1 Magnetite 1
1.2 History of Magnetite 2
1.3 Magnetite in Nature 2
1.4 Nanoscale Magnetite 3
1.5 Improvement of Drinking Water 3
CHAPTER 2 : LITERATURE REVIEW 6
2.1 Introduction 6
2.2 Magnetism 6
2.3 Uses of Nanoscale Magnetite 10
2.4 Magnetic Applications of Magnetite and Magnetic Separations 11
2.5 Arsenic as a World Health Issue 12
2.6 Uranium as a World Health Issue 12
2.7 Batch Isotherms for Adsorption 13
2.8 Adsorption Applications of Nanoscale Magnetite 14
2.9 Biomedical Applications of Nanoscale Magnetite 15
2.10 Biomedical Applications of Nanoscale Magnetite Utilizing Magnetic Separation 16
2.11 Improving the Synthesis of CdSe Quantum Dots 18
CHAPTER 3 : NANOPARTICLE SYNTHESIS AND SURFACE MODIFICATION 19
3.1 Introduction 19
3.2 Experimental Methods 21
3.2.1 Instrumentation 21
3.2.2 Materials 22
3.2.3 Synthesis and Preparation of Nanoscale Magnetite 23
3.2.4 Synthesis and Preparation of Cadmium Selenide Quantum Dots 24
3.3 Results and Discussion 27
3.4 Conclusion 37
CHAPTER 4 : KITCHEN SYNTHESIS OF nMAG 39
4.1 Introduction 39
4.2 Experimental Methods 44
4.2.1 Instrumentation 44
4.2.2 Materials 44
4.2.3 Synthesis and Preparation of Soap from Edible Oils 44
4.2.4 Synthesis and Preparation of FAM from Soap 45
4.2.5 Synthesis and Preparation of nMAG from FAM and Rust 45
4.2.6 Transferring the nMAG into Water 46
4.3 Results and Discussion 47
4.4 Conclusion 62

CHAPTER 5 : MULTIPLEX HIGH GRADIENT MAGNETIC SEPARATION 63
5.1 Introduction 63
5.2 Experimental Methods 65
5.2.1 Instrumentation 65
5.2.2 Materials 66
5.2.3 Synthesis and Preparation of Nanoscale Magnetite 66
5.2.4 Magnetic Separations of Nanoscale Magnetite 67
5.2.5 Separation of Magnetite by Size through Magnetic Separation 68
5.2.6 Analysis of Separation Data 69
5.2.7 Sharpening Nanoscale Iron Oxide Size Distributions 69
5.3 Results and Discussion 69
5.4 Conclusion 79
CHAPTER 6 : nMAG SIZE DEPENDENCE FOR ARSENIC ADSORPTION 80
6.1 Introduction 80
6.2 Experimental Methods 82
6.2.1 Instrumentation 82
6.2.2 Materials 83
6.2.3 Synthesis and Preparation of Magnetite Nanocrystals 83
6.2.4 Magnetic Separations 84
6.2.5 Sorption 85
6.2.6 Desorption 86
6.2.7 Arsenic Adsorption and the Dispersion of Materials 87
6.3 Results and Discussion 87
6.4 Conclusion 97
CHAPTER 7 : nMAG FOR THE DETECTION AND REMEDIATION OF URANIUM IN ENVIRONMENTAL MATRICES 98
7.1 Introduction 98
7.2 Experimental Methods 102
7.2.1 Instrumentation 102
7.2.2 Materials 103
7.2.3 Synthesis and Preparation of Magnetite Nanocrystals 104
7.2.4 nMAG Characterization 104
7.2.5 Uranium Analysis 105
7.2.6 Uranium Sorption Behavior (Isotherms) 106
7.2.7 Soil Preparation and Extractions 106
7.2.8 Deposition Characterization 108
7.3 Results and Discussion 109
7.4 Conclusion 120
CHAPTER 8 : URANIUM ADSORPTION CHEMISTRY AT THE nMAG SURFACE .. 122
8.1 Introduction 122
8.2 Experimental Methods 123
8.2.1 Instrumentation 123
8.2.2 Materials 123
8.2.3 Synthesis and Preparation of Magnetite Nanocrystals 124
8.2.4 Uranium Adsorption Study Utilizing Igepal CO-series Surfactants 126
8.2.4 Characterization of Adsorbed Uranium on nMAG 126

8.3 Results and Discussion 128
8.4 Conclusion 143
REFERENCES 144

LIST OF FIGURES AND TABLES

Figure 1.1 Inverse spinel unit cell of magnetite 1
Figure 2.1 M-H curves for diamagnetic and paramagnetic materials 8
Figure 2.2 Components of a ferromagnetic M-H curve 9
Figure 2.3 M-H curves for ferromagnetic and superparamagnetic materials 9
Figure 2.4 Effect of diameter on coercivity 10
Figure 2.5 Results from other alterations in reaction conditions and components 18
Figure 3.1 Tuning the diameter of magnetite nanoparticles by reaction time and molar ratio 20
Figure 3.2 PerkinElmer Optima 4300 DV inductively coupled plasma-optical emission spectrometer 22
Figure 3.3 Molecular structures of the surfactants used in this work 23
Figure 3.4 Schematic of the quantum dot reaction setup 26
Figure 3.5 Magnetite sample library 28
Figure 3.6 DLS data from three magnetite samples 29
Figure 3.7 Cryo-TEM image of Igepal CO-630 coated magnetite 30
Figure 3.8 Thermal decomposition of iron oleate in the self-assembly of magnetite nanoparticles 31
Figure 3.9 Mixing and settling of magnetite in the phase transfer into water 33
Figure 3.10 FEG-TEM images of magnetite nanoparticles coated with the Igepal CO-series 34
Figure 3.11 DLS results from magnetite nanoparticles coated with the Igepal CO-series 34
Figure 3.12 TEM image of CdSe quantum dots 35
Figure 3.13 CdSe quantum dot solutions excited by UV light 36
Figure 3.14 Alterations on the synthetic method reactions 36
Figure 4.1 Schematic of the kitchen synthesis process 46
Figure 4.2 Synthesis of magnetite nanocrystals from everyday chemicals 48
Figure 4.3 Chemical structures of four fatty acids that can be derived from edible oils 49
Figure 4.4 TEM image of kitchen synthesis magnetite 52
Figure 4.5 X-ray diffraction and selected area electron diffraction of kitchen synthesis magnetite 53
Figure 4.6 TEM image of kitchen synthesis magnetite with some laboratory chemicals 54
Figure 4.7 Temperature dependence of kitchen synthesis of magnetite nanocrystals 55
Figure 4.8 Visual cues from kitchen synthesis 57
Figure 4.9 Magnetic purification of magnetite 58
Figure 4.10 Magnetite-sand column 59
Figure 4.11 Kitchen synthesis nano-magnetite adsorption of As(V) 60
Figure 4.12 Cadmium selenide quantum dots from the kitchen synthesis 61
Figure 5.1 S.G. Frantz Canister Separator (model L-1CN) 65
Figure 5.2 TEM images of nanoscale magnetite 67
Figure 5.3 Schematic of the gravity feed HGMS experimental setup 68
Figure 5.4 Size-dependent response of nanoscale magnetite to magnetic fields 70
Figure 5.5 TEM image of tetramodal nanoscale magnetite sample 72
Figure 5.6 TEM of separated tetramodal nanoscale magnetite sample 73
Figure 5.7 Size distributions of separated nanoscale magnetite samples 74
Figure 5.8 Polydisperse magnetite sample 78

Figure 5.9 Magnetite sample with improved size distribution from magnetic separation..... 78
Figure 6.1 Inner sphere arsenic complexes with iron oxides..... 81
Figure 6.2 Schematic of magnetic separator..... 85
Figure 6.3 Comparison of magnetite nanomaterials by TEM..... 88
Figure 6.4 Magnetic separation of nanoparticles..... 89
Figure 6.5 The magnetic field dependence of particle retention. 89
Figure 6.6 Plot of arsenic(III) and arsenic (V) adsorption on different magnetite nanoparticles (i.e., 12, 20, and 300 nm). 91
Figure 6.7 Adsorption and desorption of arsenic(III) and arsenic(V) to 20 nm Fe_3O_4 at pH 6.1..... 92
Figure 6.8 Image of aggregated magnetite nanopowder in an aqueous solution..... 94
Figure 6.9 Image of dispersed magnetite nanopowder in an aqueous 0.07 wt% Igepal CO-630 solution..... 94
Figure 6.10 TEM image of aggregated magnetite nanopowder from an aqueous solution.... 95
Figure 6.11 TEM image of dispersed magnetite nanopowder from an aqueous 0.07 wt% Igepal CO-630 solution..... 95
Figure 6.12 Comparison of arsenic adsorption isotherms from aggregated and well-dispersed magnetite..... 96
Figure 7.1 U-238 decay chain..... 99
Figure 7.2 Radioactive α-decay reaction 100
Figure 7.3 Inner sphere uranium complex with iron oxide..... 102
Figure 7.4 Comparison of uranyl extraction solutions..... 107
Figure 7.5 Process schematic for the extraction, adsorption, deposition, and analysis of uranium using magnetite..... 109
Figure 7.6 Images of iron oxide nanocrystals after uranium exposure..... 110
Figure 7.7 SAXS data for the oleic acid stabilized magnetite sample..... 111
Figure 7.8 The sorption isotherms for uranyl and iron oxide nanocrystals 113
Figure 7.9 EDS data for uranium coated magnetite..... 114
Figure 7.10 Morphology of concentrated deposits of uranium-loaded nanocrystals..... 116
Figure 7.11 Solid state scintillation counting of uranium-loaded nanocrystal films 117
Figure 7.12 α-particle self-absorption from nanoscale magnetite 118
Figure 8.1 FEG-TEM images of magnetite nanoparticles coated with the Igepal CO-series125
Figure 8.2 DLS results from magnetite nanoparticles coated with the Igepal CO-series..... 125
Figure 8.3 Analytical ultracentrifugation of uranium coated nMAG stabilized by Igepal CO-630..... 130
Figure 8.4 Fluorescence effected by the adsorption of uranium onto nMAG 131
Figure 8.5 Fluorescence intensity of the unbound uranium..... 132
Figure 8.6 EDS data from Igepal CO-850 coated nMAG with adsorbed uranium..... 133
Figure 8.7 EDS data of uranium on Igepal CO-610 coated nMAG..... 134
Figure 8.8 EDS data of uranium on Igepal CO-610 134
Figure 8.9 Uranium adsorption isotherms for nMAG with the Igepal CO-series surfactants 136
Figure 8.10 Maximum sorption capacities for magnetite coated with the Igepal CO-series of surfactants 137
Figure 8.11 Vibrational spectroscopy theory on determining the binding nature of uranium 138

Figure 8.12 Raman spectra of uranyl interactions with magnetite and Igepal CO-630..... 139
Figure 8.13 Raman spectra of uranyl interactions with 18-crown-6 and Igepal CO-630..... 141
Figure 8.14 Magnetite and surfactant effect on uranium oxidation state 142

Table 3.1 Alternate CdSe reaction conditions and components 27
Table 3.2 Molecular weight of each Igepal CO-series surfactant and the corresponding PEG chain length..... 32
Table 3.3 Comparison of surfactants for phase transfer of magnetite into water..... 32
Table 3.4 Alterations of synthetic method results 36
Table 4.1 Edible vegetable oils and their fatty acid compositions 50
Table 6.1 The effect of Fe_3O_4 size on arsenic removal efficiency..... 93
Table 8.1 Langmuir isotherm quality of fit for uranium adsorption isotherms 129

Equation 2.1 14
Equation 2.2 14
Equation 5.1 75
Equation 5.2 76
Equation 6.1 90
Equation 6.2 92
Equation 7.1 111
Equation 7.2 112
Equation 8.1 135

DEDICATION

This thesis is dedicated to the scientists that have devoted their lives to the fearless pursuit of truth.

CHAPTER 1: INTRODUCTION

1.1 Magnetite

Magnetite is a mixed-valent iron oxide, Fe_3O_4, consisting of two trivalent irons and one divalent iron.[1] Iron(II,III) oxide is its IUPAC name and ferrous-ferric oxide is its common name. It has an inverse spinel structure (Figure 1.1) with the trivalent iron in the tetrahedral sites and a combination of divalent and trivalent iron in the octahedral sites.[1] It naturally exists as a brittle, black crystal with a Mohs hardness of 5.5-6.5 and is commonly found with igneous and metamorphic rocks.[2] Magnetite has many interesting properties and applications because it is the strongest magnetic material found naturally on earth.[3] At room temperature, its bulk form is considered ferrimagnetic with a Curie temperature at 850 K.[1]

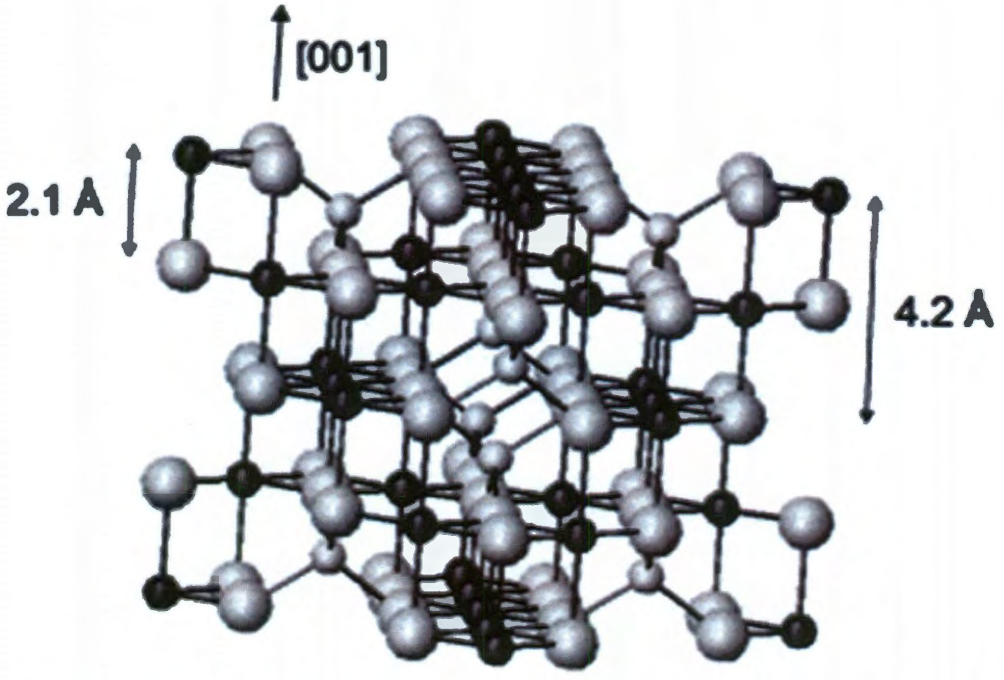

Figure 1.1 Inverse spinel unit cell of magnetite
The small black spheres represent the octahedral sites and the small gray spheres represent the tetrahedral sites. All tetrahedral sites contain trivalent iron while octahedral sites contain both trivalent and divalent iron. The large spheres represent oxygen. (Figured reprinted with permission[4])

1.2 History of Magnetite

Magnetite made its way into human society as a rare form of the mineral known as lodestone, and occurs naturally as a permanent magnet. The Greek philosopher Thales tried to explain the magnetic phenomenon that was observed with lodestone in 600 BC, and by 1000 AD, lodestone was being used by the Chinese as a magnetic compass needle.[5] Magnetite is more strongly magnetic than any other naturally occurring mineral,[3] and eventually induced scientific experiments on magnetism initially in 1269 AD by Petrus Peregrinus, and later in 1600 AD, a far more famous and thorough study of magnetism was performed by William Gilbert.[5]

1.3 Magnetite in Nature

Magnetite is formed naturally under inorganic soil formation as well as biogenically.[6] Magnetite is commonly found with metamorphic and igneous rocks.[7] But more interesting is the biogenic formation of magnetite. Magnetotactic bacteria produce strings of nanoscale magnetite particles that orient them along the Earth's magnetic field.[8, 9] Honey bees form superparamagnetic magnetite in their abdomens that help them orient themselves to the Earth's magnetic field, and appear to affect their dancing, comb building, and circadian rhythm.[10] Homing pigeons contain single domain magnetite crystals between the brain and the skull that appear to affect their navigation on cloudy days.[11] There is even evidence that humans have magnetite in bones around their sinus regions that could potentially play a role in direction orientation with respect to magnetic fields.[12]

1.4 Nanoscale Magnetite

When the size of materials decrease from bulk sizes to nanoscale many of their physical properties change.[13] Magnetite is no exception. It undergoes drastic changes with respect to its magnetic properties, going from ferrimagnetic to superparamagnetic.[14-16] While this transition is frustrating to developers of magnetic data storage due to a minimum size limit for particles to have significant remnant magnetization,[17] other technologies such as magnetic separation depend on the particle's ability to respond strongly to an externally applied magnetic field, yet become completely demagnetized upon the removal of the magnetic field.[18] Dispersed solutions of superparamagnetic nanoscale magnetite are also known as ferrofluids.[16] Several methods for top-down synthesis of nanoscale magnetite exist with several advantages, but are not generally preferred due to the lack of size control and mixture of phases.[19] Alternatively, there are many effective methods for the bottom-up synthesis of magnetite nanoparticles including co-precipitation,[20] and thermal decomposition.[21, 22] Many uses of magnetite nanocrystals require an organic molecule, polymer, or surfactant coating the particle to improve dispersion, prevent aggregation, or phase transfer the particles into other solutions.[23-25]

1.5 Improvement of Drinking Water

Access to clean drinking water is a challenge for most of the world's population; in particular, the remediation of heavy metals, such as arsenic and uranium, presents an urgent and challenging problem.[26, 27] Arsenic from both natural and manmade sources is a common contaminant in water,[28] and according to the EPA TENORM report, water is the primary carrier of uranium to the environment via uranium mines and tailings.[29] In addition, heavy metal associated health problems are often found in areas of the world that presently do not

have the resources to purify their water adequately. Several methods of metal removal are available including precipitation, adsorption, ion exchange, solvent extraction, nanofiltration, foam flotation, and (bio)sequestration.[30, 31] However, these technologies have proven difficult and/or inefficient in actual field trials. Several groups have shown in the past years that bulk iron oxides have high affinities for heavy metals, in particular for arsenic and uranium, making them good candidates for water treatment.[26, 27, 32] Engineered nanoscale materials have been of considerable environmental attention due to their small particle size and large surface area. Nanoscale sorbents offer greater sorption capacities than an equivalent mass of bulk materials due to their high surface areas, typically a two to three orders of magnitude increase in sorption capacity. Surface stabilized magnetite nanoparticles, which are homogeneously suspended in aqueous solutions, offer practical advantages for heavy metal removal in comparison to the bulk oxide materials.[33] In a similar manner, iron oxides act as known sorbents for aqueous uranium complexes.[34] Several EXAFS studies on the adsorption of uranium and arsenic on bulk or aggregated iron oxides have given insight into the coordination environment of the heavy metal ions after the adsorption process.[35, 36] However, the coordination environment of uranium or arsenic after adsorption on dispersed magnetic nanoparticles, which are surface stabilized in aqueous solution, remains to be studied.

To optimize the heavy metal sorption efficiencies with engineered iron oxide nanomaterials in water, many variables, including nanoparticle size and surfactant can be adjusted for improvements. Coordinated surfactant surface coatings can prevent material aggregation via steric or charge stabilization mechanisms allowing for well dispersed suspensions. Additionally, the chosen surfactants interact at the material interface to

maintain not only the effective surface area but also the available iron oxide surface needed for arsenic or uranium sorption.[33] Nevertheless, little is known regarding the role of the surfactant in the binding/sorption process. In addition, through avoiding aggregation, we are also interested in determining how size effects of nanoscale iron oxides, such as radius of curvature, play a role in the adsorption efficiencies and chemistries. We hope that through the employment of several analytical techniques we are able to elucidate the effect of the surfactant, the nanoparticle size, and the heavy metal concentration on the chemistry of adsorption of the heavy metal to the iron oxide surface. Understanding how uranium binds to the surface of the nanoscale iron oxides under these various conditions will allow for improved nano-iron oxide heavy metal adsorbents for water purification.

CHAPTER 2: LITERATURE REVIEW

2.1 Introduction

Nanoscale magnetite, along with its physical properties and potential applications, has recently been studied very actively and new developments are frequent. The literature consistently presents an abundance of new information on this remarkable material. A literature review of select aspects involving this fascinating material is presented here. An in-depth review of the material's properties and applications will also be discussed. Additionally, a brief discussion of another nanoparticle synthesis, CdSe quantum dots will be addressed.

2.2 Magnetism

Being the first known magnetic material[37] and the strongest naturally occurring magnet,[3] any discussion of magnetite must begin with magnetism. The magnetic properties of materials are generally characterized by their response to external magnetic fields and their magnetic moments.[38] Magnetic moments arise from unpaired electron spins in a material.[39] Ferromagnetic materials have magnetic moments even when no magnetic field is applied and are sometimes known as "permanent magnets".[38] Bulk magnetite experiences a similar but exotic magnetic property known as ferrimagnetism in which opposing magnetic moments exist in an antiparallel orientation but are not equivalent. Therefore, they do not completely cancel out the net magnetization, or the magnetic moment per unit volume.[38] Magnetic moments can also be induced by applying a magnetic field on the material.[39] If the magnetic field produced by this induced magnetic moment opposes the applied magnetic field, then the material is diamagnetic.[39] Alternatively, if the magnetic field produced by this

induced magnetic moment enhances the applied magnetic field, then the material is paramagnetic.[39]

A more detailed analysis of these magnetic characteristics is generally performed by producing M-H curves (magnetization vs. magnetic field) by applying an external magnetic field to the material and detecting its magnetization. Example M-H curves for diamagnetic and paramagnetic materials are shown in Figure 2.1. More relevant to this discussion is the M-H curve of a ferromagnetic material because it is very similar to that observed for bulk ferrimagnetic magnetite (Figure 2.2). M-H curves of ferromagnetic and ferrimagnetic materials produce a hysteresis. As an increasing external magnetic field is applied, the magnetization asymptotically reaches a maximum known as the saturation magnetization. At this point the magnetization is at its highest point and can no longer increase. As the external magnetic field decreases back to zero, the remaining magnetization that exists is known as the remanent magnetization. As the external magnetic field continues to decrease, the magnetic field necessary to reduce the magnetization back to zero is known as the coercivity.[15] Ferromagnetic and ferrimagnetic materials experience this hysteresis because of magnetic domain walls, grain boundaries, and intrinsic crystal properties.[16] As these particles get smaller and approach the single magnetic domain size, the coercivity increases due to a single domain ground state (Figure 2.3).[16] As the material becomes even smaller, the area within the hysteresis approaches zero along with the coercivity and superparamagnetism occurs (Figure 2.4). A superparamagnetic nanomaterial has magnetic moments that fluctuate freely with respect to thermal energy, but consists of individual aligned magnetic moments at the atomic level.[16] Superparamagnetic materials retain their ability to reach large saturation magnetization limits but due to their non-hysteretic nature

their coercivity is zero and they have no remenant magnetization at zero magnetic field. While superparamagnetism may be a limiting factor in some applications,[17] it is ideal for magnetic separation, as previously demonstrated, due to the ability to retain the materials under a magnetic field, but release them by removing the magnetic field because they have no remenant magnetization.[18, 33]

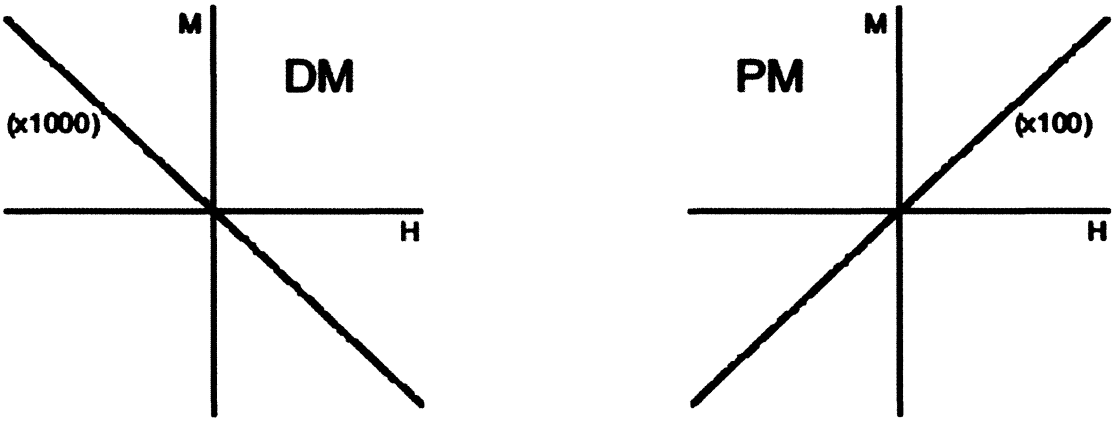

Figure 2.1 M-H curves for diamagnetic and paramagnetic materials
(DM) Diamagnetic and (PM) paramagnetic materials give decreasing and increasing linear M-H curves, respectively. (Figure adapted with permission[16])

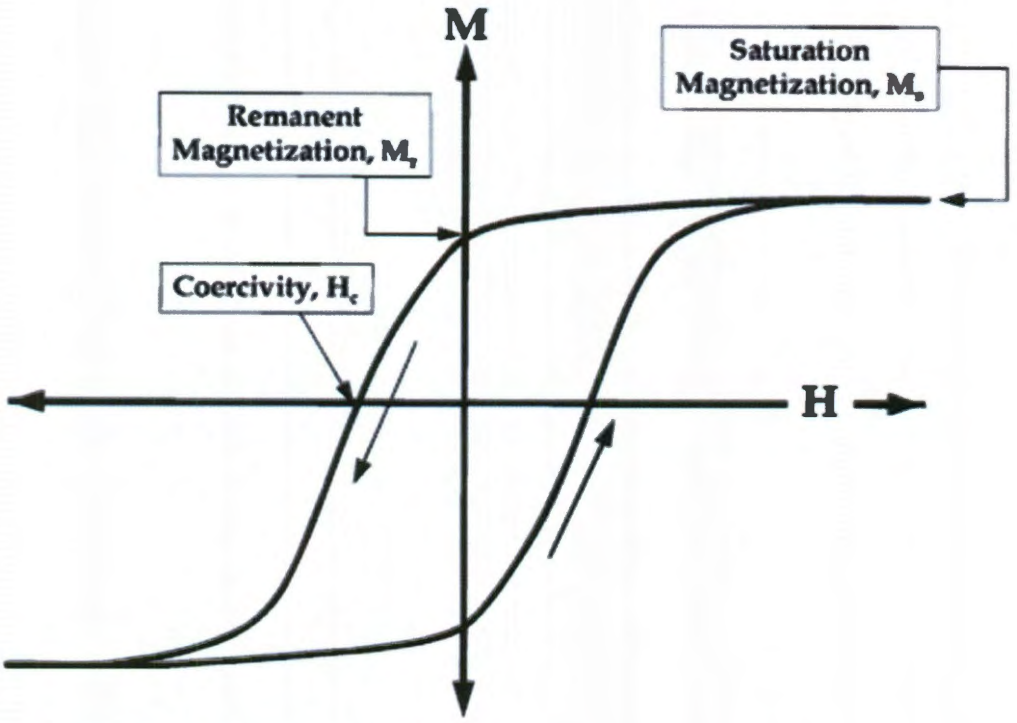

Figure 2.2 Components of a ferromagnetic M-H curve
M-H curves of ferromagnetic and ferrimagnetic materials produce a hysteresis. Where the magnetization asymptotically reaches a maximum at high magnetic fields is known as the saturation magnetization. The remaining magnetization that exists once the magnetic field is removed is known as the remanent magnetization. The magnetic field necessary to reduce the magnetization back to zero is known as the coercivity. (Figure reprinted with permission[15])

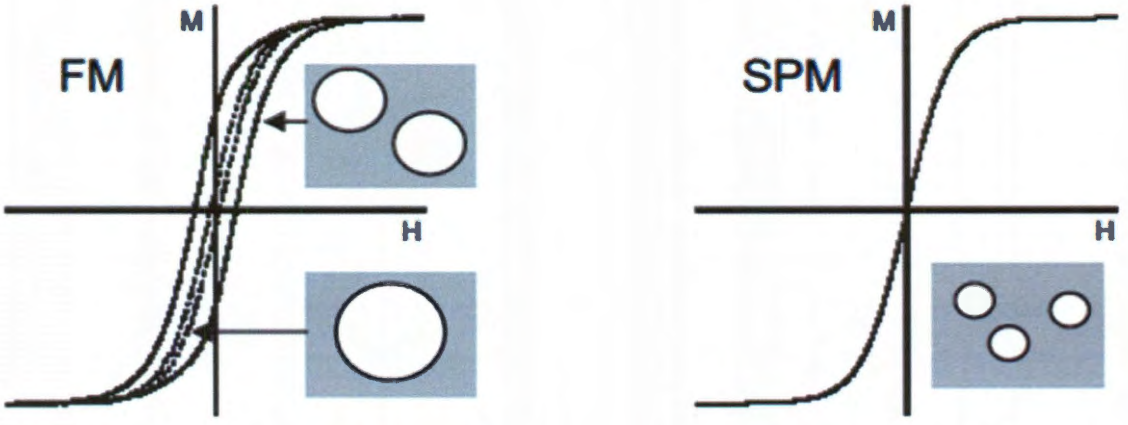

Figure 2.3 M-H curves for ferromagnetic and superparamagnetic materials
As particle sizes of (FM) ferromagnetic materials decrease from bulk to single domain, the coercivity increases. As the particle size continues to decrease to the (SPM) superparamagnetic limit, the coercivity reduces to zero. (Figure adapted with permission[16])

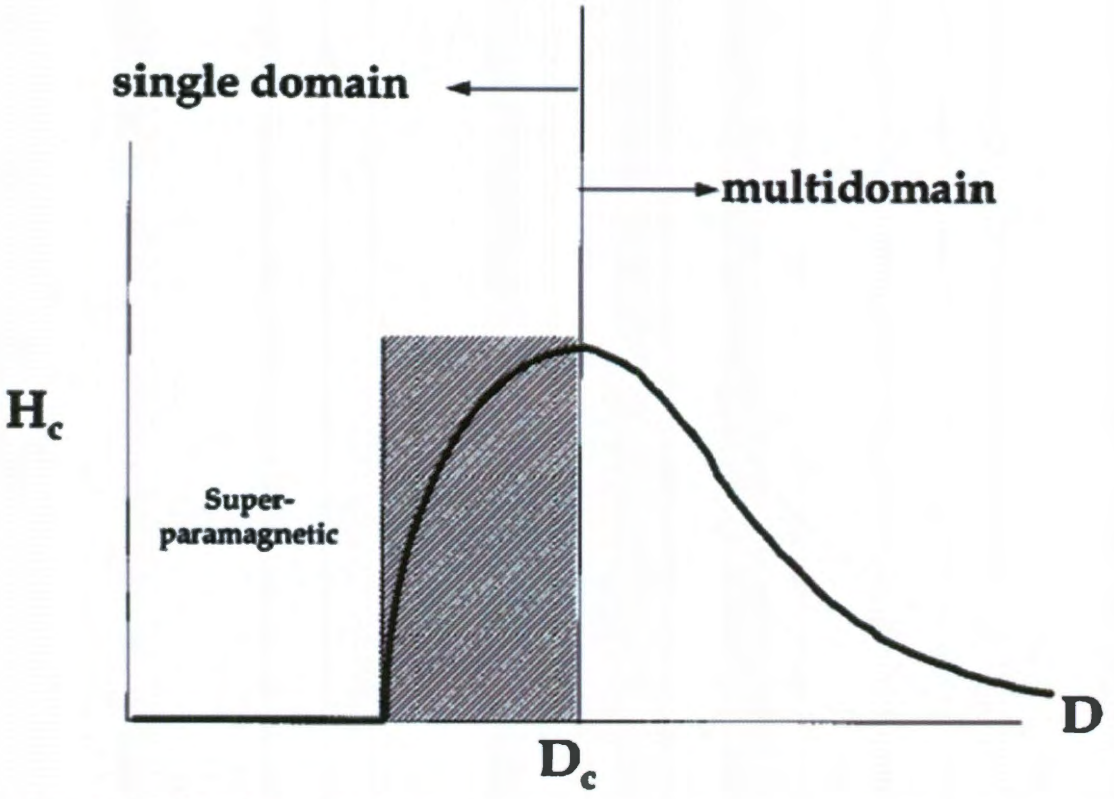

Figure 2.4 Effect of diameter on coercivity
Coercivity of particles ranging from multidomain to superparamagnetic are shown. Single domain particles demonstrate the largest coercivity while superparamagnetic nanoparticles demonstrate no coercivity. (Figure reprinted with permission[15])

2.3 Uses of Nanoscale Magnetite

Iron oxide nanocrystals have found wide applications ranging from medical imaging[40] to environmental remediation[27, 33] to on-demand drug delivery,[41] and cell culture transfection[42] due to their unique and size-dependent characteristics. The enhanced magnetic susceptibility that magnetite nanomaterials demonstrate is also central to their use in both data storage[43, 44] and magnetic separations.[18, 45] In addition to their magnetic features, magnetite (Fe_3O_4) in particular also possesses chemical properties useful for environmental technologies. While reactive iron oxide particles containing Fe(II) have been used to oxidize organic contaminants such as trichloroethylene (TCE),[46, 47] inorganic contaminants such as arsenic, lead, and uranium are sequestered at the nanoparticle interface.[33, 48, 49]

2.4 Magnetic Applications of Magnetite and Magnetic Separations

Many of magnetite's magnetic applications involve magnetic separations, and magnetite has been an essential material for magnetic separations since 1852.[45] Whitesides and coworkers have suggested that magnetic separations are an underutilized, but an extremely powerful tool for the separation of chemicals or materials that previously presented difficulty in purification or speed of separation.[50] Many magnetic separations are performed in a high gradient magnetic separator (HGMS). An HGMS consists of a magnetic field applied on a column packed with magnetically susceptible wires that dehomogenize the magnetic field and produce large magnetic field gradients that attract magnetic materials to the wires, thus separating them from the flow stream.[45, 51] Advantages of high gradient magnetic separations include minimal pressure differentiations, selective separations based on magnetic susceptibilities, and high rates of separation.[50] Magnetic separations, when compared to extended bed adsorption, has been shown to be over 10 times more productive in some bioprocessing applications.[52] Adriaens and coworkers have suggested in their immunomagnetic separations of mycobacteria that utilizing magnetite consistently demonstrates superior separations when compared to the previous standard, centrifugation.[53] Industrial scale magnetic separations are used in processes such as the purification of Kaolin clay from color impurities that also happen to be magnetic, removal of ferrous particulate materials from stack gases at iron working facilities to reduce pollution, removal of magnetic contaminants from waste waters, and removal of pyrite from coal reducing pollution by desulfurization.[45, 50]

It was previously believed that well-dispersed nanoscale magnetite below 50 nm in diameter would not be magnetically separable at low magnetic fields due to the large relative

forces of Brownian motion against a relatively low magnetic tractive force that is dependent on the particle volume.[54] However, when magnetite's diameter is less than 48 nm, non-aggregating particles can behave as single domain permanent magnets with a greatly enhanced magnetic moment.[55] Low-field magnetic separation of superparamagnetic magnetite nanoparticles below 50 nm has been demonstrated and attributed to larger magnetic moments and magnetically induced reversible aggregation, effectively making the nanoparticles act as larger particles in the presence of externally applied fields.[18, 56] The size-dependent magnetic separation of 4 and 12 nm magnetite has also been demonstrated.[18]

2.5 Arsenic as a World Health Issue

Arsenic is widespread in the earth's crust and affects millions globally via dissolution into groundwater from arsenic-containing minerals and ores in the subsurface.[57] The International Agency for Research on Cancer recognizes that long term exposure to arsenic in drinking water elevates cancer rates of the skin, lungs, urinary bladder, and kidneys, in addition to several skin diseases.[58] As a result of the growing body of knowledge on the effects of arsenic, the US EPA began enforcing a reduced maximum contaminant limit for arsenic of 10 μg/L in January of 2006.[59]

2.6 Uranium as a World Health Issue

Uranium has a natural occurrence in the Earth's crust of about 2 ppm making it the 48th most abundant element.[60] Uranium leaches into the drinking water supply by natural and anthropogenic sources.[61] Uranium in drinking water has been linked to various disorders of the kidney,[62] and long term exposure to radiological contamination of drinking water can lead to cancer.[63] According to the World Health Organization (WHO), a 15 ppb maximum

contaminant level has been given for uranium in drinking water. The WHO claims that this should be reduced to the health-based guideline value of 2 ppb, but the calculated guideline value is not practically achievable by currently available methods of remediation.[64] An example of the abundance of uranium in drinking water can be seen in the East African Rift Valley. About 78% of all water samples taken in this region would fail the European Union (EU) drinking water directives. However, the EU does not give maximum contaminant levels for uranium. If the suggested health-based guideline of 2 ppb were incorporated into the EU standards, 86% of these water samples would fail, and uranium would be the leading cause of these failures at 47%.[65] According to the WHO, uranium concentrations of up to 700 ppb have been measured in drinking water.[64]

2.7 Batch Isotherms for Adsorption

Batch isotherms serve as a rapid tool to assess the impact of water chemistry on adsorption to nanomagnetite.[66] They have been shown to work quite well to determine the arsenic remediation efficiency of magnetite as an adsorbent,[18, 27, 33] as well as aid in the studies of adsorption kinetics.[67, 68] In batch isotherm adsorption studies, the sorbent is added in an equal amount to a series of solutions containing various concentrations of sorbate, or contaminant, while all other conditions remain consistent. The adsorption isotherm plot produced by plotting sorption density, q, against the initial sorbate concentration can be fitted against several isotherm fits, depending on several adsorption characteristics. A fit to a Langmuir isotherm assumes that all adsorption sites are equivalent, the sorbate is immobilized upon adsorption, sorbates do not interact, and that there can be only a

monolayer of sorbate because adsorption can only occur once at each binding site.[69] The Langmuir isotherm is described by the equation:

Equation 2.1

$$q = \frac{b \times q^{max} \times C}{(1 + b \times C)}$$

where b is the sorption constant (L/μmol), q is the sorption density (μmol/g), C is a constant, and q^{max} is the maximum sorption density of the sorbent (μmol/g).[33]

A fit to a Freundlich isotherm is preferential when there is a multiple sorbate system.[70] The Freundlich isotherm is described by the equation:

Equation 2.2

$$q = K_F \times C^N$$

where K_F is the Freundlich constant, N is the Freundlich exponent, and C is the concentration of the dissociated sorbate.[33] These isotherm equations can be used to fit the data from batch isotherm data and give important sorbent information such as maximum sorption capacity.

2.8 Adsorption Applications of Nanoscale Magnetite

Large scale drinking water treatment plants can remove arsenic economically by relying on traditional $FeCl_3$ or alum coagulation and flocculation, followed by sedimentation or filtration.[71] However, that technology is not easily scaled down. Thus in the last decade, much research has been conducted on iron and iron-oxide based sorbents, that would enable arsenic treatment at smaller scales.[72]

Nanomagnetite is an iron-oxide sorbent which, displays high affinity for both As(III) and As(V) and, as the most magnetic natural mineral on earth, can be manipulated by a low-strength magnetic field.[3, 18] However, little has been done beyond batch studies to determine a more ideal design and operating conditions of a nanomagnetite-based treatment method that

could disseminate into wide use. Researchers at Rice University, with a focus on application, have advanced batch isotherm, lab-scale column, and pilot-scale field research for nanomagnetite enhanced sand filtration for removal of arsenic and other heavy metals from drinking water.

Uranium has been shown to be removed by many of the same techniques utilized for arsenic removal, such as coagulation, ion exchange, precipitation softening, and activated alumina, but these techniques are not always adequate for all conditions.[64] A large variety of highly effective methods must be available to reduce the uranium in drinking water to a healthy level in the various water conditions around the world. Nanoscale magnetite (nMAG) can be used as one of these tools to achieve highly efficient removal of uranium from drinking water via adsorption.

Nanoscale magnetite has been shown to be an efficient adsorbent material for many inorganic contaminants in drinking water, most notably for arsenic, but nMAG shows a high affinity for uranium as well.[73, 74] However, little has been done in this area. Also, because of the α-particles emitted by uranium,[60] nMAG can also work as a vital part of uranium detection in an effort to find possible anthropogenic uranium dump sites by concentrating soluble uranium more densely on less sorbent material allowing for less α-particle self-absorption.[75]

2.9 Biomedical Applications of Nanoscale Magnetite

Magnetite nanoparticles have a promising future in biomedical applications because they can be engineered to be biocompatible and non-cytotoxic in ways that do not affect their unique magnetic properties.[23] Applications utilizing the thermal energy production of the superparamagnetic nanoparticles under an alternating magnetic field have promise for the

hyperthermia treatment of cancer cells.[16] Superparamagnetic magnetite nanoparticles also give strong a Magnetic Resonance Imaging response in *in vitro* applications.[23] Other studies have shown that magnetite can be used in a system that, through magnets, can be remotely triggered, demonstrating on-demand drug delivery. Nanoscale magnetite has great potential as an integral part of biomedical applications.

2.10 Biomedical Applications of Nanoscale Magnetite Utilizing Magnetic Separation

Magnetic separations in biotechnology are crucially important. Their use has become ubiquitous in applications such as cell sorting[16, 76-89] and protein purification.[90-110] Typically, these applications utilize large magnetic beads in binary separations. Effectively, the biomaterial that is linked to the magnetic bead is "collected," and those not bound to the magnetic bead are not collected, resulting in a binary separation. The method of magnetic multiplex separation presented here may allow separations more complex than binary.

Utilizing biocompatible nanomaterials for the magnetic separations of biological materials is advantageous for biomedical applications.[16] The literature now provides a plethora of magnetic protein separations.[90-110] These magnetic protein separations dominantly utilize superparamagnetic nanoparticles encased in a matrix, termed "magnetic beads," but examples utilizing simple superparamagnetic nanoparticles are also exist. One lab on a chip scale magnetic protein separation utilizes individual 5 nm superparamagnetic nanoparticles.[100] In this case, the nanoparticles are coated with a pH responsive polymer, and biotinylated. The nanomaterial is then combined with streptavidin, which is bound to the biotinylated nanoparticles and the pH is reduced to induce aggregation. The nanomaterial is then passed through an H-shaped microfluidic channel that contains a laminar fluid interface

with a solution that has a higher pH, and a permanent magnet. As the aggregated nanomaterial flows through the channel, the magnet pulls the material through the laminar fluid interface into a solution of higher pH, dispersing the nanomaterial and flowing through the channel into the higher pH output. Non-magnetic material will flow into the low pH output.

But binary magnetic protein separations are extremely limiting. Applications such as the lab on a chip example described above could be improved to separate 3 or 4 types of proteins simultaneously with several different strength permanent magnets. Additionally, no pH adjustments that could potentially denature the proteins would be necessary. Hatton and co-workers describe a magnetic separation of three proteins in a mixture, but this method still consists of binary magnetic separations and utilizes pH adjustments for the adsorption and desorption of the selected proteins, once again potentially denaturing the proteins in some cases.[90] The size dependent separation capabilities intrinsic to nanoscale superparamagnetic nanoparticles will allow for multiplex separation of proteins without pH adjustment.

Magnetic cell sorting applications have also become widespread.[16, 76-89] Magnetic cell sorting is usually performed with magnetic beads due to greater magnetophoretic mobility, but can be performed with individual superparamagnetic nanoparticles, with advantages such as reducing interferences with tests on the separated cells.[16] In one example of magnetic cell sorting, the magnetic beads are pretreated with monoclonal antibody and combined with the cells, binding to the cells with the antigen specific to the antibody on the magnetic bead, and separated magnetically.[77] This could even be performed *in-vivo* by injecting nanoparticles coated with antibodies into the bloodstream. The nanoparticles could then be removed via extracorporeal magnetic separation as seen in Chen *et al.*[111] One could

conceive that utilizing a tunable electromagnet or several permanent magnets of varying magnetic strengths at the extracorporeal magnetic separator may achieve an *in-vivo* multiplex magnetic separation of cells.

2.11 Improving the Synthesis of CdSe Quantum Dots

A small portion of this work will focus on improvements to the synthesis of cadmium selenide quantum dots. Producing high quality CdSe quantum dots with more biologically and environmentally friendly solvents and reagents is necessary for many of their applications. Systematic alterations are a useful area readily explored method of synthesis improvements. Methods similar to Peng and co-workers, where reactants are altered to improve the quality of the quantum dots (Figure 2.5),[112] can be used to improve the synthesis of CdSe quantum dots by altering reaction conditions and components.

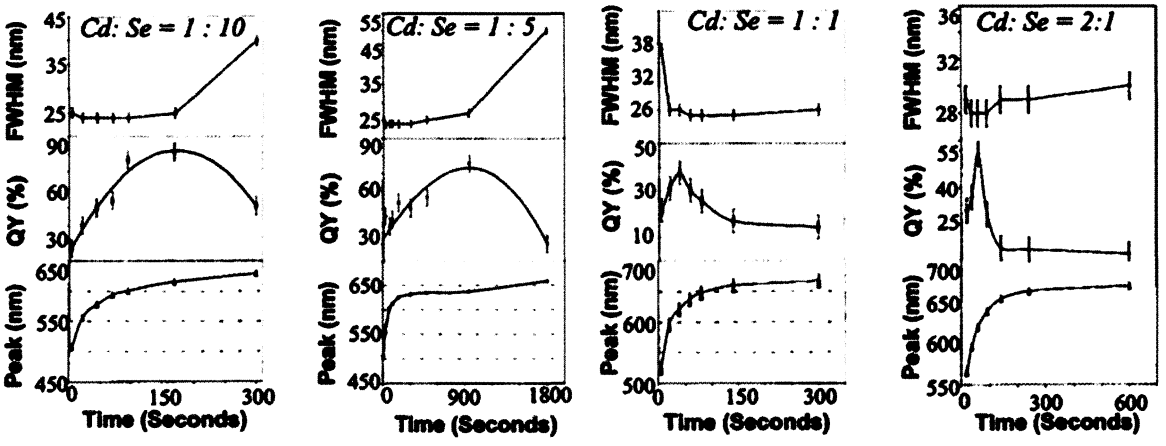

Figure 2.5 Results from other alterations in reaction conditions and components
The effects of altering reaction times and Cd:Se ratios on the size (given by absorbance peak position), the PLQY, and the size distribution (given by FWHM), are shown. (Figure reprinted with permission[112])

CHAPTER 3: NANOPARTICLE SYNTHESIS AND SURFACE MODIFICATION

3.1 Introduction

The synthesis of specially engineered nanomaterials has experienced expansive growth over the past several decades.[113, 114] There are many factors in the design of a nanomaterial: composition, size, size distribution, shape, shape distribution, surface structure, core-shell structure, dopants, and surface stabilizers just to name a few. Amongst nanomaterials that have received a high degree of attention are nanoscale iron oxides and semiconductor quantum dots due to their magnetic and photoluminescent size-dependent physical properties, respectively. The first synthesis of magnetite ferrofluid was performed in 1964, initially starting with a top-down, ball milling process.[115] A bottom-up synthesis of magnetite was later developed as a ferrous and ferric chloride co-precipitation of magnetite in alkaline solutions.[20] In 2004, scalable, size-tunable syntheses of near-monodisperse magnetite nanoparticles were developed that produced materials in organic solvents by the thermal decomposition of iron carboxylate salts.[21, 22] These methods allowed various sizes of magnetite nanoparticles to be produced in a one-pot synthesis by altering the reaction time or the molar ratio of iron to coordinating solvent (Figure 3.1).[22] With this newly discovered and highly improved synthesis, studies of size-dependent properties were able to be performed. It was observed that within the superparamagnetic region of nanoscale magnetite, separations of particles could be made by altering an external magnetic field due to the increased magnetic response by the larger particles.[18]

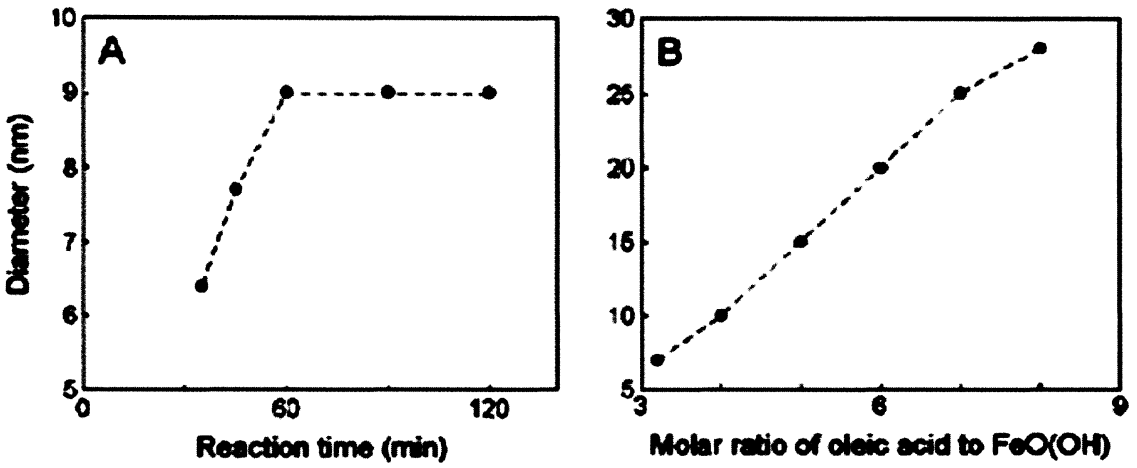

Figure 3.1 Tuning the diameter of magnetite nanoparticles by reaction time and molar ratio
The diameter of magnetite nanoparticles can be increased by longer reaction times and larger molar ratios of oleic acid to FeO(OH). (Figure reprinted with permission[22])

Quantum dots are another material of significant recent interest.[112, 116-123] Their use as biomarkers, solar cells, and LEDs have made attaining less toxic nanomaterials while increasing the nanoparticle quality a goal of many scientists.[123] Quantum dots made from cadmium selenide have received particular interest due to their size and shape control.[123] Historically, CdSe quantum dots have been synthesized with methylcadmium and selenium powder in tri-alkyl phosphines, creating monodisperse quantum dots with some shape control.[116] To create a greater applicability for these materials, a cleaner synthesis, limiting toxic or other dangerous reagents and solvents is another topic explored in this work. Additionally, increasing the photoluminescence quantum yield (PLQY) would improve upon the current limitations of current CdSe quantum dots.

To achieve control over a nanoparticle system, both the reaction mechanism and surface chemistry of the resulting nanoparticles must be understood. Another key component in nanoparticle systems is surface modification. Without this, nanomaterials face substantial limitations to meaningful applications. Surface chemistry allows for enhanced stability, phase transfer to less toxic solvents, and custom functionalization of the nanoparticles,

broadening the potential uses of these materials. To more fully understand magnetite and CdSe quantum dot nanoparticles, both their synthesis and surface chemistry are examined here, leading to the creation of monodisperse nanoparticles with improved features that can be effectively manipulated at the nanoparticle interface.

3.2 Experimental Methods

3.2.1 Instrumentation

Nanoparticle concentrations via iron content were quantitatively determined by a PerkinElmer Optima 4300 DV Inductively Coupled Plasma-Optical Emission Spectrometer (ICP-OES) (Figure 3.2). Low speed centrifugation for purification was performed with a Thermo IEC Centra CL2, a Fisher Scientific Marathon 22K, or a Thermo Scientific Sorvall Legend RT+. High-speed ultracentrifugation for purification was performed with a Beckman-Coulter Optima L-80 XP Ultracentrifuge or a Beckman-Coulter Optima L-90K Ultracentrifuge. Probe sonication for phase transfer was performed with a Hielscher UP100H Ultrasonic Processor or a Branson Digital Sonifier. The size of the nanoscale materials were measured using a JEOL 2010 Transmission Electron Microscope (TEM), a 2100 JEOL Field Emission Gun Transmission Electron Microscope (FEG-TEM) or a JEM FasTEM 2010 Cryo-Transmission Electron Microscope (Cryo-TEM). Solution dispersion of iron oxide nanoparticles were analyzed with a dynamic light scattering Malvern Zetasizer Nano ZS (DLS). A Varian-Cary 5000 UV-visible-NIR spectrophotometer was used to obtain UV-visible spectra of the quantum dots and the PLQY was determined with the help of a SPEX FluoroLog-3 Spectrofluorometer w/UV-Vis.

Figure 3.2 PerkinElmer Optima 4300 DV inductively coupled plasma-optical emission spectrometer

3.2.2 Materials

FeO(OH) from Sigma-Aldrich (iron(III) oxide, hydrated; catalyst grade, 30-50 mesh; cat. #371254) was ground to 100-150 mesh. Oleic acid (90% technical grade) and 1-octadecene (ODE) (90% technical grade), Cadmium oxide (CdO), trioctylphosphine (TOP), trioctylphosphine oxide (TOPO), and hexadecylamine (HDA) were purchased from Sigma-Aldrich. Stearic acid was purchased from Avocado. Hexanes (certified ACS grade) were purchased from Fisher Scientific. Many nonionic surfactants, including Triton N-101, Triton X-100, Tween 20, Tween 80 were purchased from Sigma-Aldrich, Pluronic P123 was purchased from BASF, and the Igepal CO-X series of surfactants (where X = 210, 530, 610,

630, 660, 710, 720, 730, 850, 887, 890, 970) received as samples from Rhodia, were used. The molecular structures of these surfactants are shown in Figure 3.3.

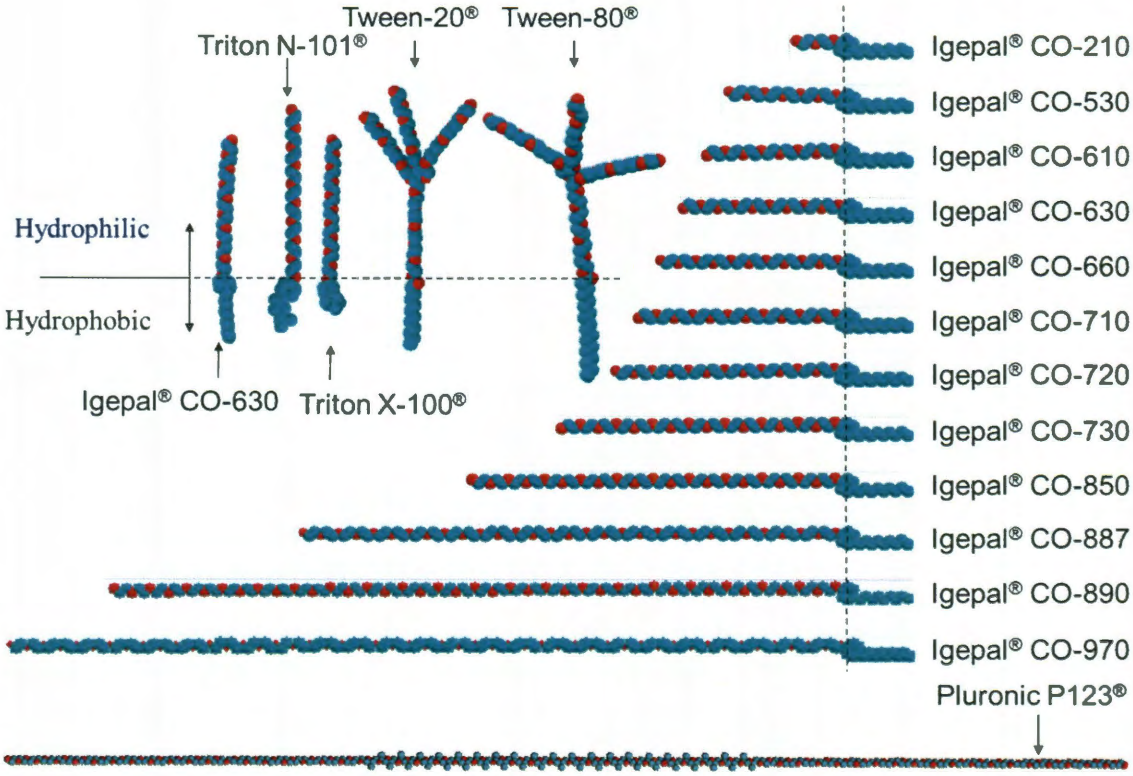

Figure 3.3 Molecular structures of the surfactants used in this work

3.2.3 Synthesis and Preparation of Nanoscale Magnetite

A scalable one-pot synthesis of magnetite nanocrystals was performed by mixing FeO(OH) (2.00 mmol), oleic acid (8.00 mmol), and 1-octadecene (20.00 mmol). The mixture was heated with stirring at 320°C and kept at this temperature for a desired time, as seen in Yu *et al.*[22] Excess reactants in the as-prepared samples were removed by repeated cycles of flocculation upon ethanol and acetone addition, followed by centrifugation at 4,500 rpm. The supernatant was then decanted and the precipitated particles were redispersed in a

small quantity of hexanes. This process was repeated several times, and the resulting black suspensions were stored in hexanes with no evidence of aggregation over a period of months.

The resulting nanocrystals were then made water soluble by two different methods. The first method was similar to those seen in work performed by Landfester and coworkers[25] where 1 mL Fe_3O_4 nanocrystals in hexanes was added to 4 mL 10 wt% Igepal® CO-630 solution. Many other surfactants, including Triton N-101, Triton X-100, Tween 20, Tween 80, Pluronic P123, and the rest of the Igepal CO-X series of surfactants (where X = 210, 530, 610, 630, 660, 710, 720, 730, 850, 887, 890, 970), were used in a similar fashion. After the addition of the magnetite to the surfactant solution, the sample was shaken and probe sonicated for several minutes. Then, the solution was centrifuged twice at 4,500 rpm for 1 hour each time, removing excess surfactant from the top and sedimented aggregates from the bottom. The nanocrystals that remained suspended in solution were then collected by two rounds of ultracentrifugation at 50,000 rpm for 1 hour. The excess surfactant was decanted and the settled nMAG was redispersed in water.

The second method used to make the magnetite water soluble was performed by adding 0.03 mL oleic acid to 1 mL of the nanoparticle stock suspension and then mixing with 10 mL of Millipore® water. The phase separated mixture was probe sonicated for 5 min and was centrifuged at 4,500 rpm for 15 min before passing through a 0.2 μm syringe filter (Whatman, GD/X, nylon). The filtrate was a clear suspension of magnetite nanoparticles coated with a bilayer of oleic acid dispersed in water.[24]

3.2.4 Synthesis and Preparation of Cadmium Selenide Quantum Dots

Similar to syntheses seen in previous literature,[121] a size-tunable one-pot synthesis of CdSe quantum dots was performed under an inert atmosphere by mixing 0.026 g CdO to

0.228 g stearic acid at 200°C with stirring. The solution initially becomes colorless at ~124°C. The mixture was then allowed to cool to room temperature. Next, 0.503 g TOPO, 0.502 g HDA, and 3.034 g ODE were added to the cooled flask and heated with stirring to 280°C. Then a solution of 0.948 g 10 % selenium in TOP was mixed with 1.052 g ODE in a glove box. This solution was rapidly injected into the heated cadmium solution and the temperature dropped to 250°C where it was maintained. High quality quantum dot samples where synthesized within the first seconds to minutes and the nanoparticle growth was quenched by rapid withdrawal of the sample and addition into cool chloroform. A schematic of the reaction setup can be seen in Figure 3.4. Seven alternates of this reaction were also performed to gain an understanding of the synthetic method (Table 3.1). The first alternate removes to HDA and adds the TOPO and ODE initially, removing the cooling down requirement. The second alternate reaction removes the TOPO. The third alternate removes the TOPO and replaces the stearic acid with oleic acid. The fourth alternate removes the TOPO and reduces the CdO and stearic acid in half. The fifth alternate removes TOPO, replaces stearic acid with oleic acid, and reduces the CdO, oleic acid, and 10 % Se-TOP in half. The sixth alternate removes TOPO, replaces stearic acid with oleic acid, and reduces the CdO, oleic acid, and 10 % Se-TOP in a quarter. The seventh alternate removes TOPO and HDA, replaces stearic acid with oleic acid, and reduces the CdO, oleic acid, and 10 % Se-TOP in a quarter. These samples were then analyzed by TEM, UV-Vis spectroscopy and fluorescence spectroscopy. PLQY was determined by comparing quantum dot samples with select laser dyes as standards.

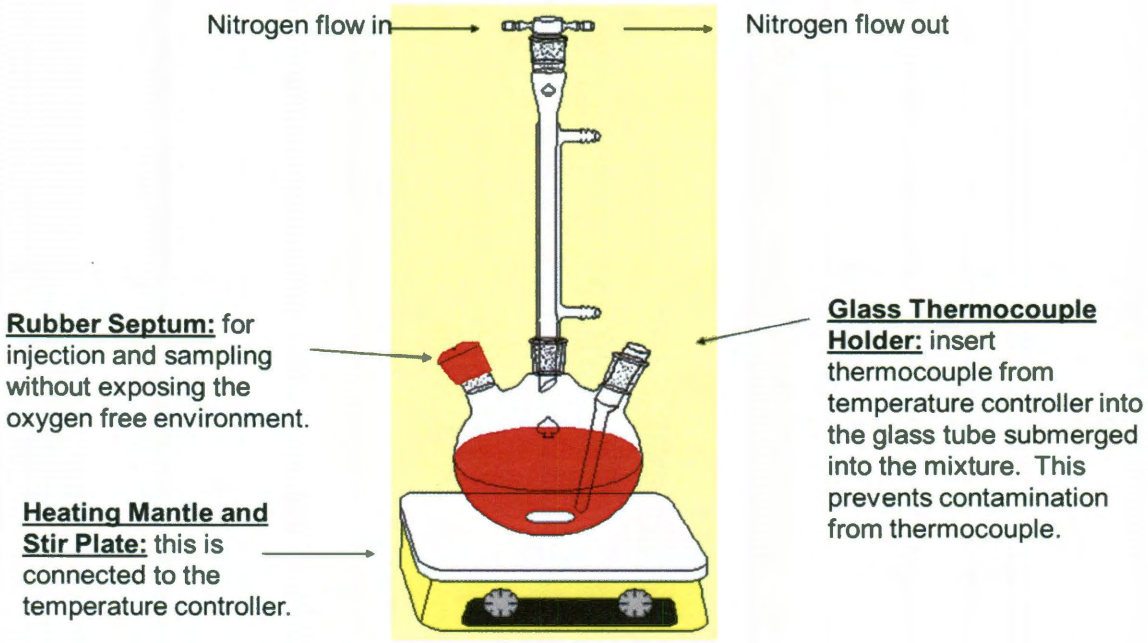

Figure 3.4 Schematic of the quantum dot reaction setup

Table 3.1 Alternate CdSe reaction conditions and components

	Step 1	T_1	Step 2	T_2	Step 3	T_3
Original	CdO + Stearic Acid	200°C, then cool to RT	+TOPO +HDA +ODE	280°C	10% Se in TOP + ODE	250°C
Alternate #1	CdO + Stearic Acid	RT	+TOPO +ODE	280°C	10% Se in TOP + ODE	250°C
Alternate #2	CdO + Stearic Acid	200°C, then cool to RT	+HDA +ODE	280°C	10% Se in TOP + ODE	250°C
Alternate #3	CdO + Oleic Acid	200°C, then cool to RT	+HDA +ODE	280°C	10% Se in TOP + ODE	250°C
Alternate #4	1/2CdO + 1/2Stearic Acid	200°C, then cool to RT	+HDA +ODE	280°C	10% Se in TOP + ODE	250°C
Alternate #5	1/2CdO + 1/2Oleic Acid	200°C, then cool to RT	+HDA +ODE	280°C	1/2 10% Se in TOP + ODE	250°C
Alternate #6	1/4CdO + 1/4Oleic Acid	200°C, then cool to RT	+HDA +ODE	280°C	1/4 10% Se in TOP + ODE	250°C
Alternate #7	1/4CdO + 1/4Oleic Acid	200°C, then cool to RT	+ODE	280°C	1/4 10% Se in TOP + ODE	250°C

3.3 Results and Discussion

The magnetite synthesis presented here[22] has been utilized extensively in our laboratory. This synthesis has proven to be scalable and nanoparticle size tunable. A library of magnetite samples has been produced and TEM images of select samples can be seen in Figure 3.5. The samples produced by this method are well-dispersed in hexanes as demonstrated by DLS (Figure 3.6). After phase transfer into water with Igepal CO-630, the sample remains well-dispersed as seen in Cryo-TEM images (Figure 3.7). Magnetite is

quantitatively analyzed after acid digestion in HNO_3 by ICP-OES through iron detection and correcting for the added mass of oxygen in Fe_3O_4 to give a mass per volume concentration. For particle per volume concentrations, the diameters determined by TEM are used and particles are assumed to be spheres. Knowing the volume per particle and the density of magnetite (5.17 g/mL),[124] particle concentrations can be calculated.

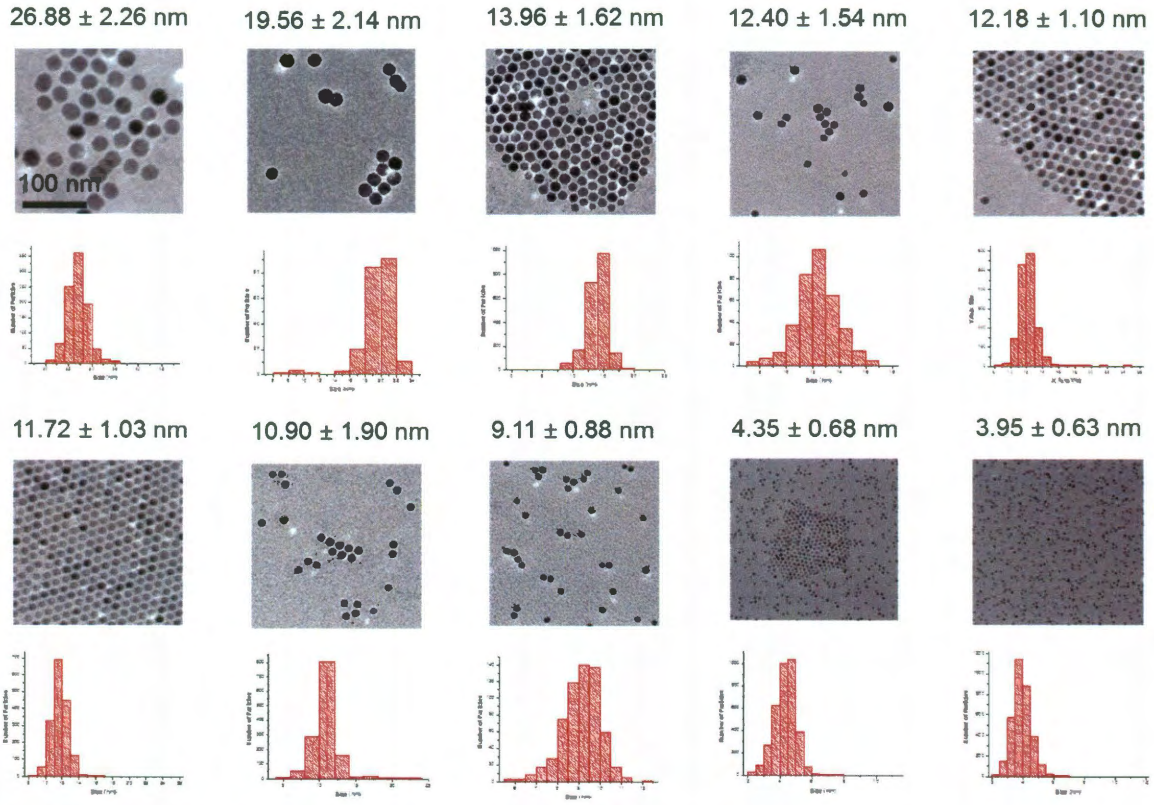

Figure 3.5 Magnetite sample library
TEM images of a select set of ten magnetite nanoparticle samples and their histograms representing their size distributions. The 100 nm scale bar is consistent for all images.

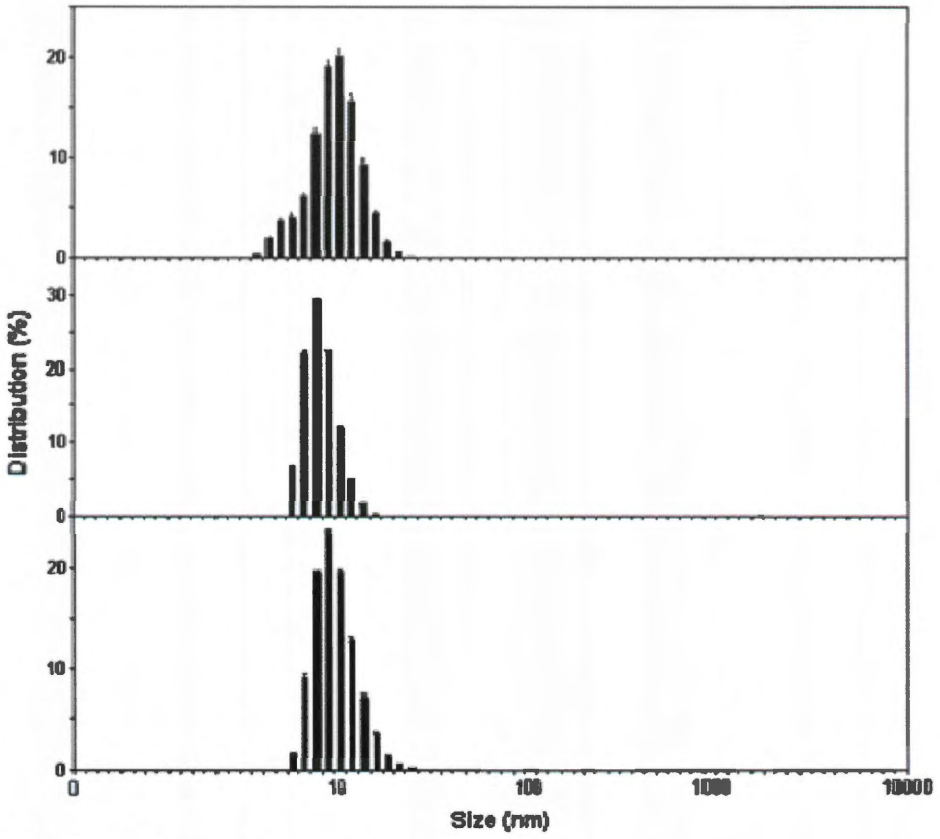

Figure 3.6 DLS data from three magnetite samples
The DLS data matches well with the hydrodynamic diameters of the magnetite samples and more importantly shows no evidence of any hard aggregation.

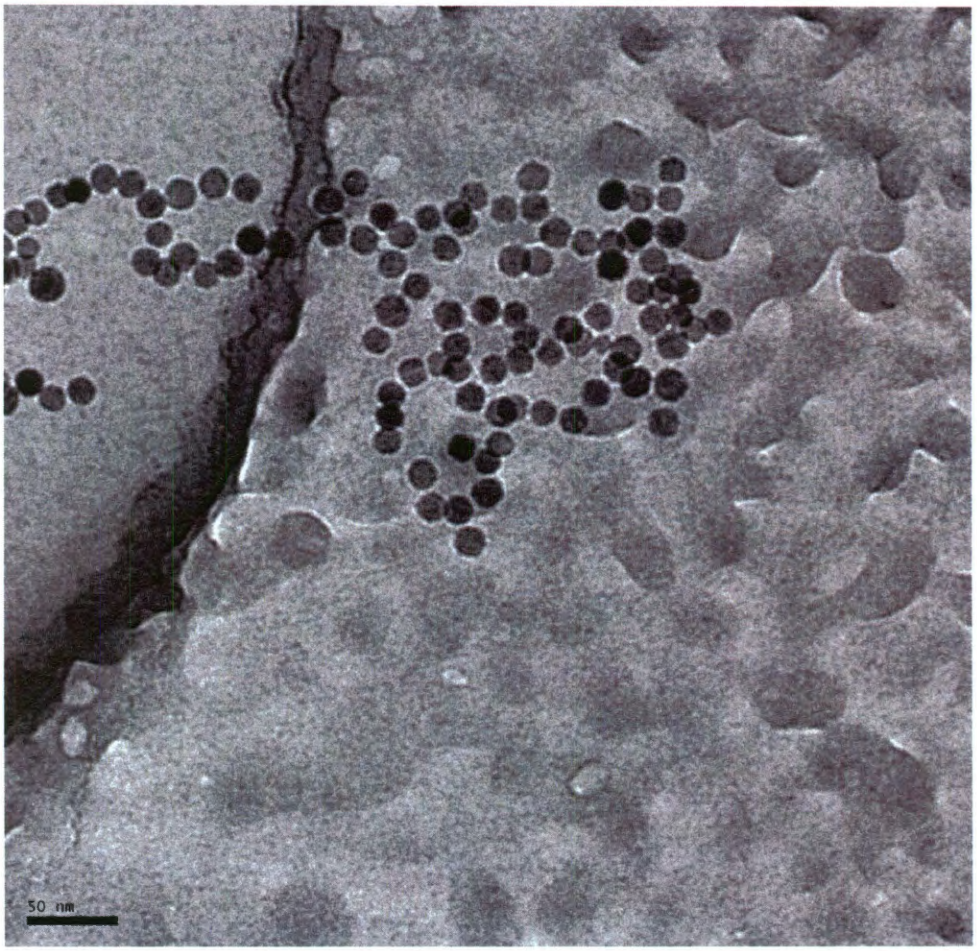

Figure 3.7 Cryo-TEM image of Igepal CO-630 coated magnetite

The growth mechanism for the synthesis of the magnetite nanoparticles is believed to occur in two steps. The first step involves the dissolution of the FeO(OH) in oleic acid to produce iron oleate or an iron oxide oleate.[22] This product then undergoes a thermal decomposition to self-assemble Fe_3O_4 nanospheres guided in size and shape by the oleic acid and oleate reverse micelles (Figure 3.8).[21, 22] Some research groups suggest that in a similar synthesis maghemite is formed along with the magnetite and this is plausible for our synthesis as well.[125] This synthetic process routinely produces nanomaterials that are more uniform in size and shape than magnetite nanomaterials produced through methods involving

the chloride co-precipitation of magnetite from ferrous and ferric chloride.[20] Because of the native oleic acid coating, the thermal decomposition reaction provides samples with far less aggregation than the co-precipitation reaction.[20-22] The limitation of the thermal decomposition reaction is that for an aqueous dispersion, a phase transfer must occur.

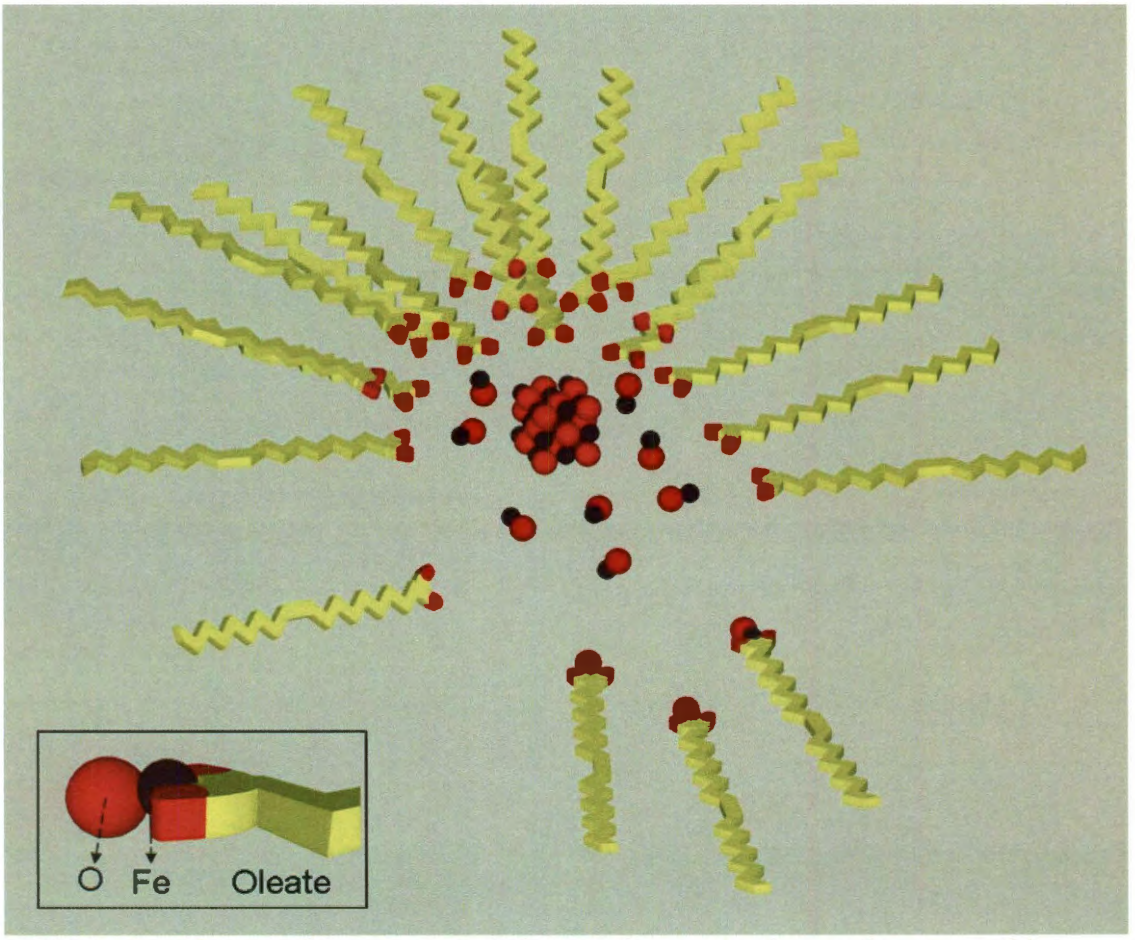

Figure 3.8 Thermal decomposition of iron oleate in the self-assembly of magnetite nanoparticles

The magnetite was made water soluble by a variety of nonionic surfactants, including Triton N-101, Triton X-100, Tween 20, Tween 80, Pluronic P123, and the Igepal CO-X series of surfactants (where X = 210, 530, 610, 630, 660, 710, 720, 730, 850, 887, 890, 970). The Igepal CO-series all have the structure Polyoxyethylene nonylphenylether, a nine carbon alkyl chain bound to a benzene ring that is bound to PEG chains of varying lengths (Table

3.2). These surfactants were compared by factors including ease of mixing and ease of settling (Table 3.3). Digital images of the Igepal series surfactants in this process are shown in Figure 3.9. These Igepal series surfactant coated materials were also characterized by FEG-TEM (Figure 3.10) and DLS (Figure 3.11).

Table 3.2 Molecular weight of each Igepal CO-series surfactant and the corresponding PEG chain length

Igepal CO-	n=PEG	MW calc
210	2	308.46
530	6	484.67
610	7	528.73
630	9	616.83
660	10	660.89
710	11	704.94
720	12	748.99
730	15	881.15
850	20	1101.42
887	30	1541.95
890	40	1982.48
970	50	2423.01

Table 3.3 Comparison of surfactants for phase transfer of magnetite into water

Surfactant	Ease of Initial Mixing	Ease of Settling
Tween® 20	+	++
Triton® N-101	+	+
Triton® X-100	-	+
Tween® 80	-	-
Pluronic® P123	--	--
Igepal® CO-210	--	--
Igepal® CO-530	++	++
Igepal® CO-610	++	--
Igepal® CO-630	++	--
Igepal® CO-660	++	--
Igepal® CO-710	+	--
Igepal® CO-720	+	-
Igepal® CO-730	-	+
Igepal® CO-850	--	+
Igepal® CO-887	--	++
Igepal® CO-890	+	++
Igepal® CO-970	++	++

Ease of Initial Mixing

++	=	reactants readily mix
+	=	reactants mix
-	=	reactants mix only after sonication
--	=	reactants mix only after multiple rounds of sonication

Ease of Settling

++	=	foam settles quickly after sonication
+	=	foam settles slowly after sonication
-	=	foam settles several days after sonication
--	=	centrifugation is required for the foam to settle after sonication

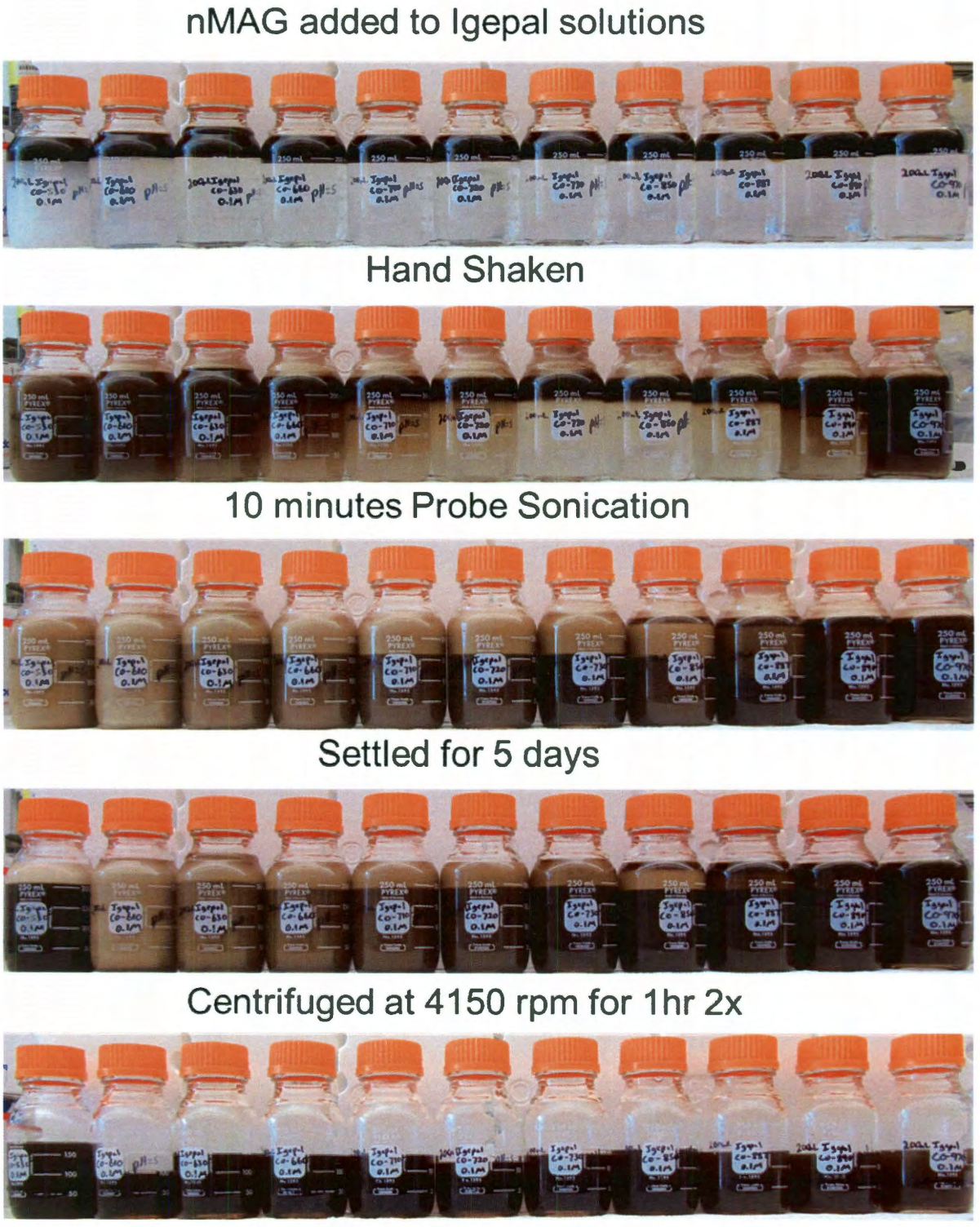

Figure 3.9 Mixing and settling of magnetite in the phase transfer into water
Igepal CO-X (where X = 530, 610, 630, 660, 710, 720, 730, 850, 887, 890, 970) is displayed from left to right.

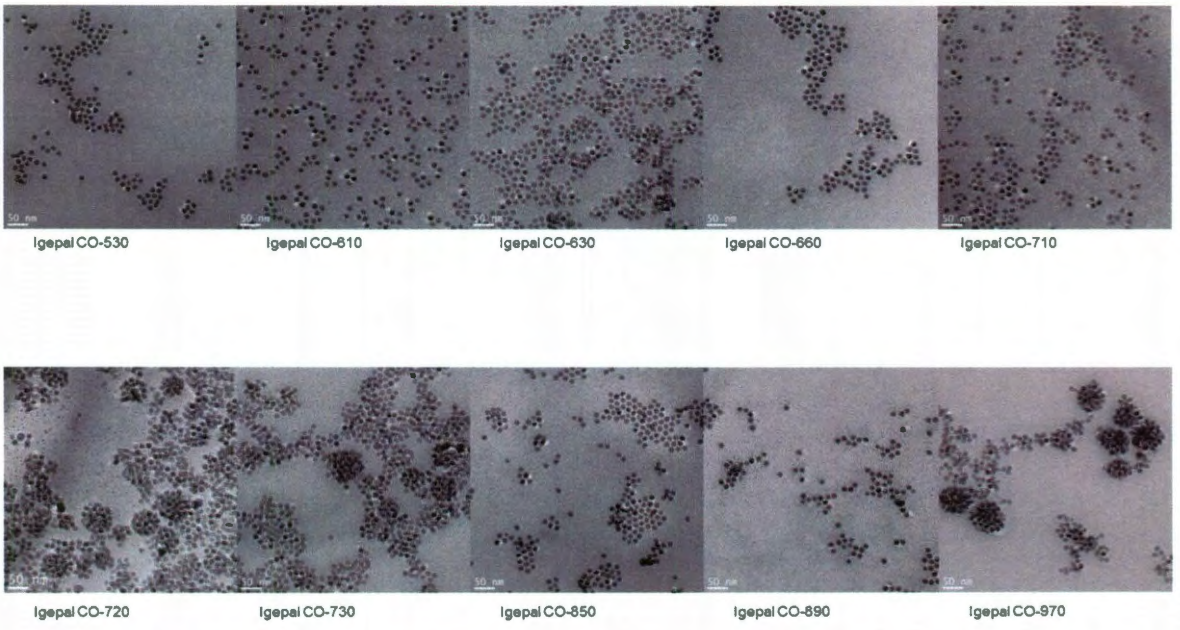

Figure 3.10 FEG-TEM images of magnetite nanoparticles coated with the Igepal CO-series

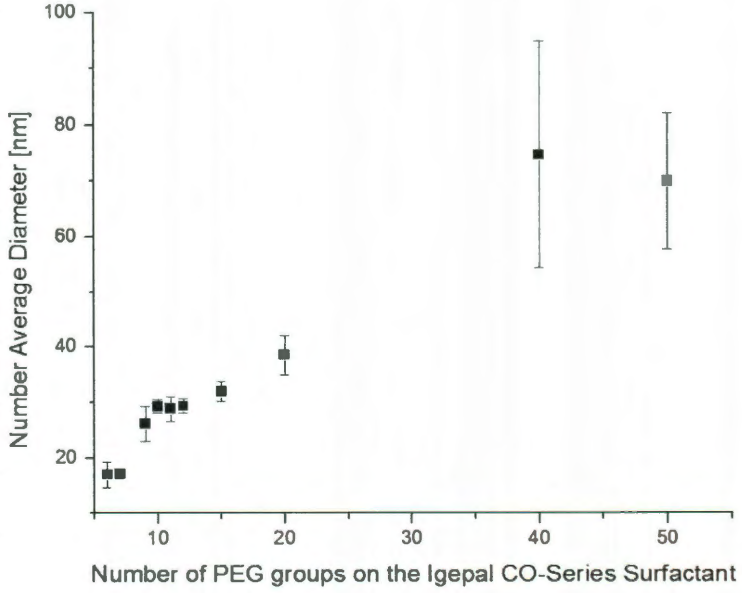

Figure 3.11 DLS results from magnetite nanoparticles coated with the Igepal CO-series

The CdSe quantum dots were produced with high quality size distributions and PLQY. An example TEM image of CdSe quantum dots synthesized by this procedure (Figure 3.12) as well as digital images of several sizes photoluminescing under a UV light (Figure 3.13) are shown. Alternate reactions 2-5 failed to produce high quality quantum dots. The remaining reactions (Figure 3.14) did produce high quality quantum dots and were compared (Table 3.4) using absorbance wavelength, half-width half maximum (HWHM), and PLQY.

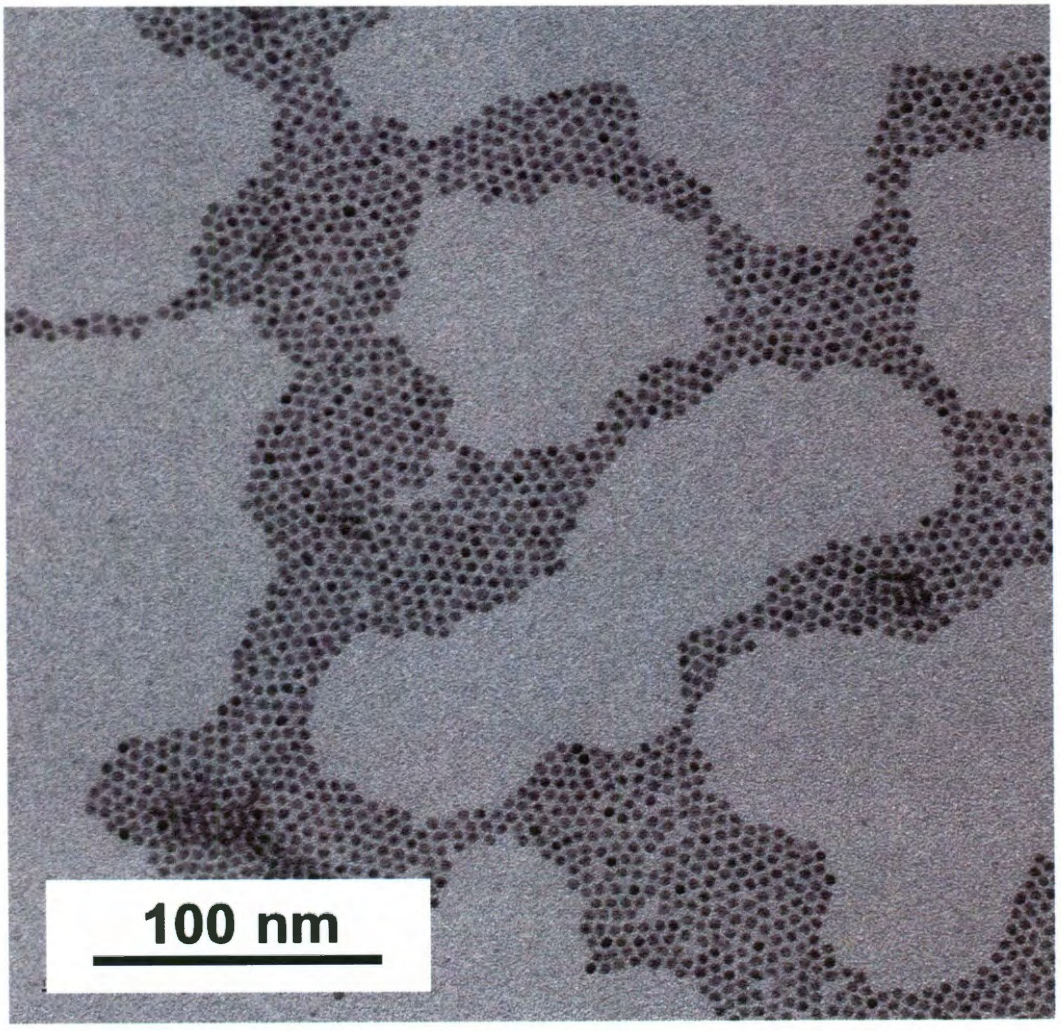

Figure 3.12 TEM image of CdSe quantum dots

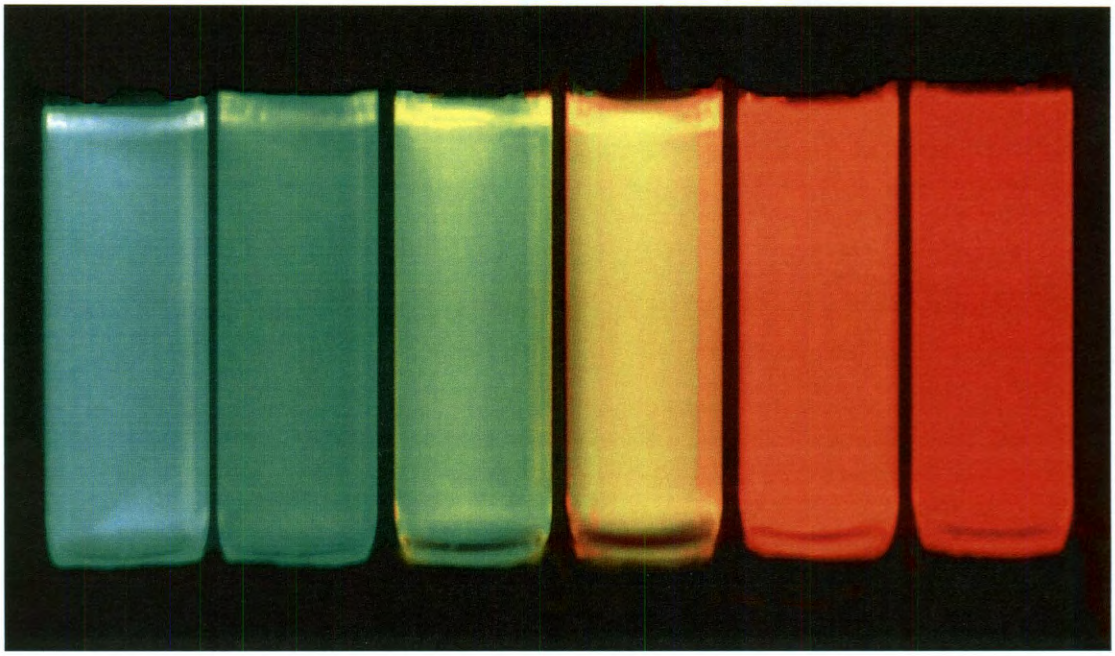

Figure 3.13 CdSe quantum dot solutions excited by UV light

Original	CdO + stearic acid + Se-Top	TOPO, HDA, ODE →	CdSe Quantum Dots
Alternate #1	CdO + stearic acid + Se-Top	TOPO, ODE →	CdSe Quantum Dots
Alternate #6	CdO + oleic acid + Se-Top	HDA, ODE →	CdSe Quantum Dots
Alternate #7	CdO + oleic acid + Se-Top	ODE →	CdSe Quantum Dots

Figure 3.14 Alterations on the synthetic method reactions

Table 3.4 Alterations of synthetic method results

Sample	TOPO	HDA	λmax	HWHM	Reaction Time	PLQY
Original	Yes	Yes	520.6 nm	13.7 nm	15 s	
Alternate #1	Yes	No	525.8 nm	16.0 nm	15 s	
Alternate #6	No	Yes	521.8 nm	13.8 nm	13 s	84.9%
Alternate #7	No	No	536.1 nm	23.5 nm	15 s	18.5%

The original synthetic method works well to provide monodisperse CdSe quantum dots, but all the reaction components are not necessary. By removing either or both TOPO and HDA, cheaper and more environmentally and biologically friendly reactions can be produced. When HDA is removed, PLQY is reduced. When TOPO and HDA are removed, the quantum dots become less monodisperse. When just TOPO is removed, the reaction must be scaled down, but this is not necessary when both TOPO and HDA are removed. It seems that HDA improves PLQY, and TOPO aids in the formation of monodisperse and large scale batches of quantum dots. Cd:Se ratios and reaction times can also be altered to achieve the appropriate size, PLQY, or size distribution. The improvement of a quantum dot synthesis depends on what is desired. These discoveries should serve as a guide in improving synthesis for specific applications.

3.4 Conclusion

Both syntheses of magnetite and quantum dots have been shown to provide reproducible, high-quality near-monodisperse nanomaterials in organic solvents at high temperatures. The magnetite has proven to be versatile enough to phase transfer into water

under a variety of conditions. The CdSe quantum dots have been produced without some of the harmful and expensive reactants with little to no change in sample quality. Cleaner syntheses such as these are necessary for future broad applications in biological and environmental settings.

CHAPTER 4: KITCHEN SYNTHESIS OF nMAG

4.1 Introduction

Iron oxide nanocrystals have found wide applications ranging from medical imaging to environmental remediation due to their unique and size-dependent characteristics.[33, 40] Both Fe_3O_4 and γFe_2O_3 are ferrimagnetic materials, and when their diameters are less than 48 nm non-aggregating particles can behave as single domain permanent magnets.[55] The enhanced susceptibility that results is central to their use in both data storage[43, 44] and magnetic separations.[18, 45] Even smaller sizes, below 10 nm in diameter, exhibit superparamagnetic properties and find use as MRI contrast agents,[40] triggers for on-demand drug delivery,[41] and magnetic transfection reagents in three dimensional cell cultures.[42] In addition to their magnetic features, these systems, magnetite (Fe_3O_4) in particular, also possesses chemical properties useful for environmental technologies. While reactive iron oxide particles containing Fe(II) have been used to oxidize organic contaminants such as trichloroethylene (TCE),[46, 47] inorganic contaminants such as arsenic, lead, and uranium are sequestered at the nanoparticle interface.[33, 48, 49] When particle diameters are as low as 10 nm, the materials can be removed from water via handheld magnets, suggesting an attractive avenue for water purification in settings that lack power as well as technical infrastructure.[18] Further development of these materials for point-of-use water purification, particularly in the developing world, requires innovative approaches to their manufacturing that are both economical as well as accessible to potential users.

This work introduces a paradigm for creating nanoscale materials which not only lowers their cost, but also enables small-scale production and rapid innovation at sites with

little to no conventional manufacturing infrastructure. We were motivated to pursue this avenue of chemical research because of our interest in nanoscale magnetite for arsenic removal.[18, 27, 33] Arsenic contamination in ground water is a severe global problem, most notably in Southeast Asia where millions suffer from acute and chronic arsenic poisoning.[72, 126, 127] Removing arsenic from groundwater in impoverished rural or urban areas without electricity and with no manufacturing infrastructure remains an outstanding problem.[30] Our recent work suggests that low-field magnetic removal of nanoscale arsenic sorbents may be a viable solution.[18] A substantial barrier for transferring this knowledge, as well as other nanotechnologies designed for global use, is the difficulty of engaging local communities in the development and commercialization process. The inaccessibility and high cost of the essential material components, often highly uniform nanocrystals, contribute significantly to the problem. Even if nanomaterials and systems are given away through charitable endeavors, end users still have little ability to adapt and ultimately commercialize the technologies through their local economies.

Developing users who are active partners, and ultimately experts in the technology, requires that two different elements come together in a manufacturing strategy. The first is a production process which optimizes not only cost and scale, but also uses simple, available, and transferable materials and techniques. Research on nanocrystal production has recently begun to emphasize the cost, efficiency, and environmental impact of standard processes.[128, 129] For materials destined for the developing world additional consideration must be given to the simplicity and accessibility of a process. Similar to work in "appropriate technology", this strategic element defines a successful manufacturing approach as one that makes use of

everyday tools and materials, is appropriate for the local infrastructure, and is easily adapted by interested users.[130-133]

An equally important consideration is the means by which this manufacturing information is shared. Thirty years ago, the only way to imagine such information transfer would have been through a network of costly laboratories and facilities in different locales, each grappling with legal, social, and communication issues. Now, access to the Internet, coupled with the principles of the Free and Open Source Software (FOSS) movement, have shown that users all over the world can become innovators, manage systems complexity in new ways, and navigate the legal issues associated with peer production.[134-136] The success of FOSS has been demonstrated in software, and increasingly in other domains as well. Since roughly 2001, the principles of open source have been successfully applied in the following domains: music and film (Creative Commons "creativecommons.org", Open Source Cinema "opensourcecinema.org"), textbook production (Connexions "cnx.org", MIT's Open CourseWare "ocw.mit.edu"), robotics (Terk "terk.ri.cmu.edu"), biotechnology (Cambia "cambia.org") and synthetic biology (BioBricks Foundation "biobricks.org"). Its application to nanotechnology would be novel and especially important for global technology as it is ideally suited to empower local users to define and ultimately adapt its content for their unique needs. Open-source frameworks can only work, though, if scientists develop appropriate nanomanufacturing processes, with reproducible and clear instructions, using widely available materials. Taken together, appropriate manufacturing processes and the FOSS model result in what we term here as a "vernacular nanotechnology", or a nanotechnology developed by a shared and evolving set of manufacturing methods.

Applying this principle of vernacular nanotechnology presents a significant research challenge for materials chemists. Nanotechnology is based on the unique properties of highly complex materials whose performance often depends on accurate control over nanometer scale features. Researchers and industry alike rely on million dollar lithographic facilities, electron microscopes, and state-of-the-art chemical laboratories to achieve their materials performance. Indeed, it may be that for some processes, particularly top-down fabrication, appropriate manufacturing methods could never be achieved. However, chemical methods for forming nanomaterials are reasonable targets for appropriate manufacturing. Research over the last few decades has provided a wealth of practical knowledge and understanding of the mechanisms governing nanocrystal formation in solution phase reactions.[22, 137] This base of knowledge suggests that under the right conditions, even with poor thermal control, impure solvents, and ambient atmospheres, it may be possible to generate reasonably high quality and functional nanocrystals.

Here we report a method to produce nanocrystalline and functional iron oxides using everyday items and equipment found in restaurants and kitchens worldwide. Commercial nanocrystalline magnetite is available from several producers, such as Sigma-Aldrich, where it is provided on the 250 gram scale for $223.00;[138] while the powders have high surface areas, they are heavily aggregated, poorly crystalline and non-uniform in size. For research laboratories, the co-precipitation of iron (II) and iron (III) salts is a simple and green approach to forming particulates of iron oxides.[20, 139] The products of these reactions however are not always monodisperse, and they are prone to aggregation; while surface stabilizers can be added with some success to create isolated nanoparticles, some limitations remain.[25] The limitations of these older methods have in the last seven years inspired many

studies of nanocrystalline iron oxide synthesis.[21, 22] Briefly, iron precursors can decompose into iron oxides in organic solvents at temperatures in excess of 260 °C; the presence of amphiphilic stabilizers regulates the growth of crystalline products which are either magnetite, maghemite, or mixtures of both phases. When inexpensive iron sources are used the reaction can be scaled to the gram level at relatively low cost.

The goal of this work was to use thermal decomposition as a departure point for defining a simple, accessible process that would yield functional magnetic nanocrystals. The term 'accessible' has a specific connotation within the community of researchers who study technology transfer to the developing world. It describes a technology that contains components which can be fully controlled, in this case manufactured, by the intended users. This creates not only the opportunity for local economic development, a necessary condition for sustainability of new technology, but also for innovations that adapt new technological capabilities to their specific settings. Adaptation of water purification technologies is especially important as environmental constraints, population size, and cultural tradition make both the problems inherent to developing societies and their solutions a strong function of local conditions. For the application of any nanocrystal in water purification, the materials themselves are an ongoing consumable and a central element in the technology. A conventional manufacturing process optimized for large material quantity and long distance delivery would be counterproductive. For our process, a better option would be a procedure that could be adapted by individuals who may already have experience with recycling, restaurant operations, or ceramics production. We call this approach 'point-of-use' manufacturing.

4.2 Experimental Methods

4.2.1 Instrumentation

In this process two sets of equipment were used. First, the synthesis was performed in a kitchen type setting and included standard pots, pans, Pyrex casserole dishes, measuring cups, cheese graters, wooden spoons, hot plates, and thermometers. Then laboratory analysis to quantitatively determine the nanoparticle concentrations via iron content or to quantitatively analyze arsenic concentrations was carried out by a PerkinElmer Optima 4300 DV Inductively Coupled Plasma-Optical Emission Spectrometer (ICP-OES) or a PerkinElmer Optima Elan 9000 Inductively Coupled Plasma-Mass Spectrometer (ICP-MS). The instrument utilized to determine the size of the nanoscale iron oxides was a 2100 JEOL Field Emission Gun Transmission Electron Microscope (FEG-TEM).

4.2.2 Materials

For the saponification reaction, edible oils such as olive oil, coconut oil, and vegetable oil along with white distilled vinegar (preferably 9 % acidity) and Crystal Drain Opener® (or lye, sodium hydroxide, caustic soda, caustic potash etc.) were purchased from local grocery stores or garden supply centers. For the magnetite synthesis rust was collected by brushing it off of any rusty ferrous metal and was ground as finely as possible.

4.2.3 Synthesis and Preparation of Soap from Edible Oils

In a typical kitchen synthesis of iron oxide nanocrystals, soap is produced from olive oil or other edible oils. The soap is prepared by dissolving 15 g Crystal Drain Opener® in 30 mL water with stirring. This solution will become hot. While this solution is still hot, it is

added to 100 g oil. The solution is stirred for about 15 minutes or until tracing occurs. The thick slurry is then placed in a dry, well-ventilated area to sit for a week to cure.

4.2.4 Synthesis and Preparation of FAM from Soap

The soap is then grated with a cheese grater. The grated soap is then added to vinegar with 9% acidity (1 mL acid for 1 g soap, typically 60 g soap in 650 mL vinegar) and boiled until all the soap is dissolved and a yellowish-brown organic layer is formed at the surface. Let the solution cool and remove the top organic layer with a spoon or turkey baster. This layer can be heated separately to remove excess water and clarify the solution. This organic liquid is the fatty acid mixture (FAM).

4.2.5 Synthesis and Preparation of nMAG from FAM and Rust

In a typical synthesis of nanoscale iron oxides, 1 gram of rust, collected by brushing rust off of any rusty ferrous metal is ground as finely as possible. The rust is combined with 20 g of FAM in a frying pan or pot with a loose cover to allow the escape of smoke and steam. **Caution:** This synthesis should be performed in a well-ventilated area. For pans with a large diameter, more FAM may be required. The reaction mixture is cooked for two hours or until a fully black solution is achieved with little to no smoking. This method produces 50-90 nm nanocrystals. If a steam cooker is used, 15-20 nm nanocrystals can be achieved. The entire process schematic can be seen in Figure 4.1.

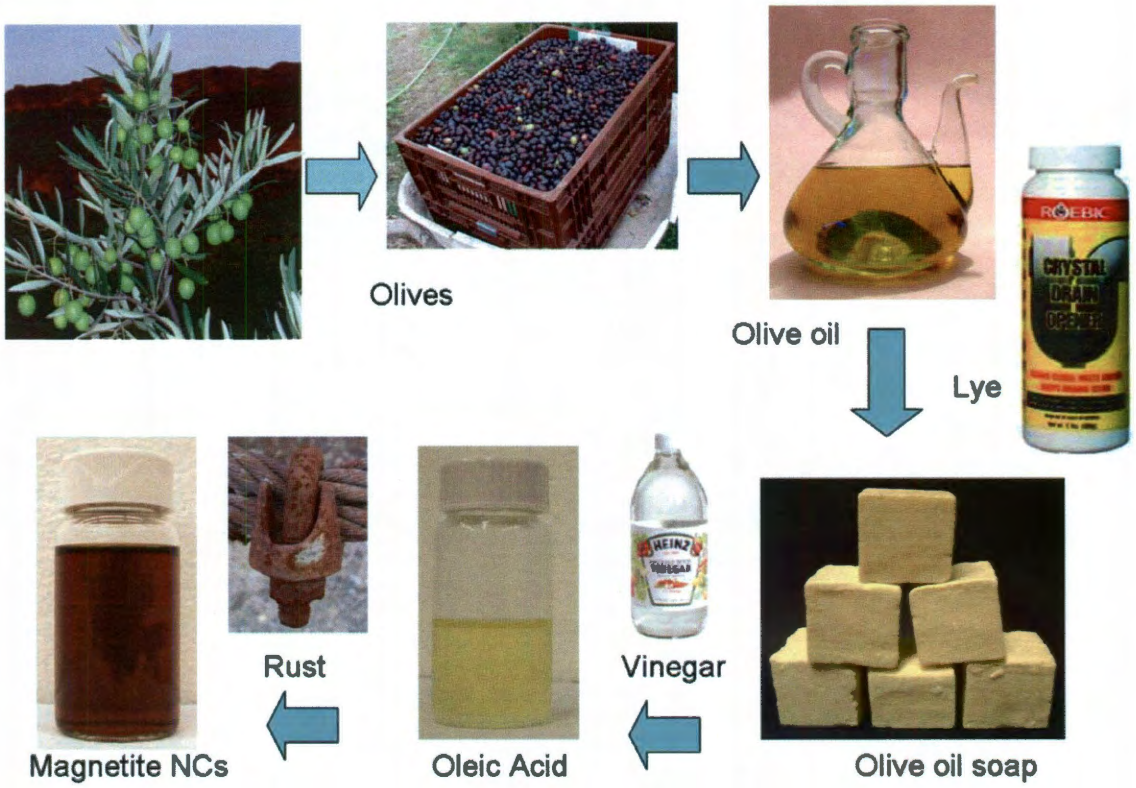

Figure 4.1 Schematic of the kitchen synthesis process
A visual representation of the kitchen synthesis to help guide the order of the procedures.

4.2.6 Transferring the nMAG into Water

If an aqueous solution of iron oxide nanocrystals is desired, 10 g of grated soap can be dissolved in 100 mL of water (heating may be necessary). Then, 3-5 g of the waxy black iron oxide material can then be added to 40 mL of the aqueous soap solution and boiled for 30 min resulting in a brown, aqueous solution of iron oxide nanocrystals. The sample can be partially purified by coarse filtration (i.e. coffee filter), and excess soap can be removed by using a magnet to attract the nanocrystals and decanting the remainder of the non-magnetic solution.

4.3 Results and Discussion

We first focused on finding nanocrystal starting products that in the spirit of our vernacular approach would be simply generated from inexpensive, everyday items. Monounsaturated fatty acids, particularly oleic acid (*cis*-9-octadecenoic acid), are central components in the preparation of both semiconductor and iron oxide nanocrystals.[22, 137] These acids are referred to as 'ripening agents' because they stabilize the soluble forms of the metal which both limits crystal nucleation (leading to larger particles) as well as promotes particle growth at intermediate times. They can serve as both solvent and stabilizer, or they can be diluted with inert heat transfer fluids and combined with other additives to tune the nanocrystal growth process.[21, 22, 122]

The basic reactants in the formation of iron oxide nanocrystals were replaced with everyday items, without significant loss of material quality (Figure 4.2). Thermal decomposition reactions typically require an iron precursor, a thermally stable, non-polar solvent (diluent), and an amphiphilic stabilizing agent (fatty acid).[22] Prior work in this group established that it is possible to run the magnetite synthesis without a non-polar solvent in pure fatty acid, though the resulting sizes are slightly larger than is optimal for arsenic removal.[140] Still the simplicity offered by a two reactant process was attractive, and both the iron precursor and fatty acid could be replaced by everyday items.

Figure 4.2 Synthesis of magnetite nanocrystals from everyday chemicals
Ingredients and tools for a typical nanocrystal synthesis: (left to right) Edible oil, vinegar, pan, Crystal Drain Opener, and rusted steel. Reaction equation is given on the top right where FAM stands for Fatty Acid Mixture.

A common source of these organic acids is the edible oils found in kitchens worldwide. These oils are predominately triglycerides (> 90 w/w%) which can be converted to their carboxylate salts (e.g. soap) through a simple saponification reaction, involving the addition of a base such as lye. The resulting soap can then be acidified with vinegar forming an organic acid (fatty acid), leaving the unwanted glycerin and other impurities behind in the aqueous phase. The resulting fatty acid of the olive oil precursor is approximately 70 % pure oleic acid, and its impurities include linoleic acid (12 %), palmitic acid (12 %), and stearic acid (2 %) (Figure 4.3).[141] We refer to this mixture as 'FAM' for fatty acid mixture and its composition is highly sensitive to the origins and quality of the starting oil.[142] The use of extra virgin olive oil, for example, will increase the yield of oleic acid in the final mixture as compared to lower grade olive oil. While we focused here on oleic acid from olive oil,

edible oils from many regions (including coconut oil, linseed oil, and others) all contain significant amounts of fatty acids appropriate for these reactions.[143] The fatty acid compositions of other edible oils are given in Table 4.1.

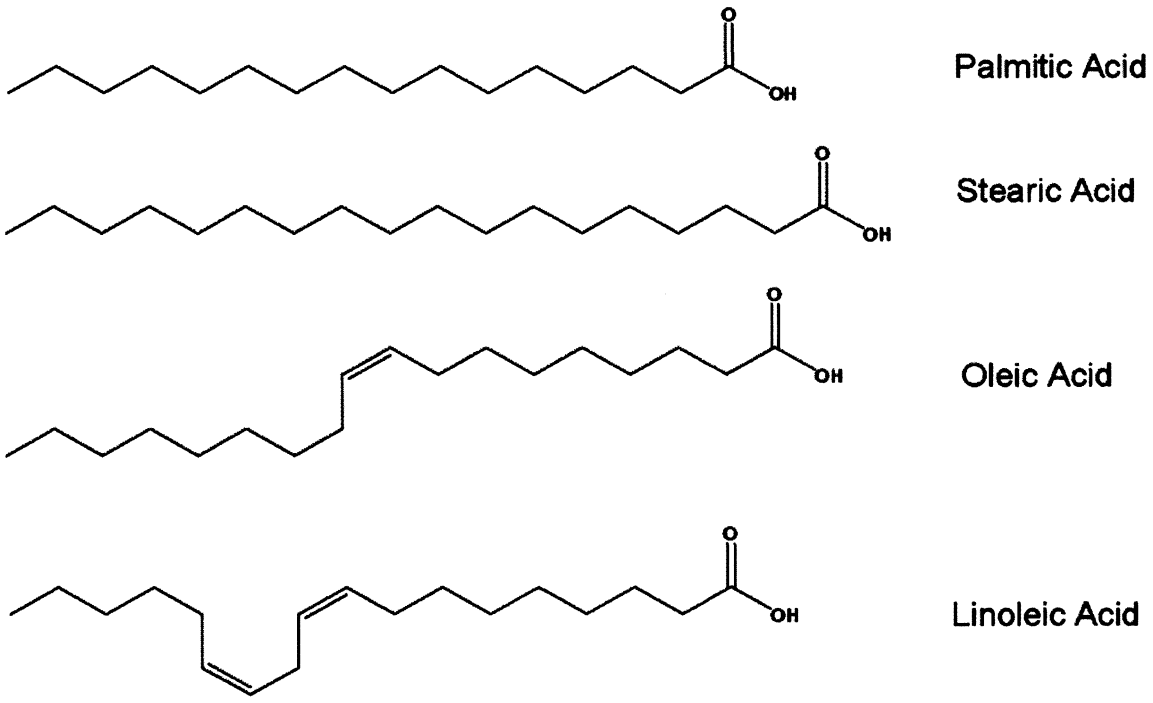

Figure 4.3 Chemical structures of four fatty acids that can be derived from edible oils
Chemical structures of fatty acids that are dominantly derived from edible oils. (Figure reprinted with permission[140])

Table 4.1 Edible vegetable oils and their fatty acid compositions

Fatty Acid	Canola Oil	Corn Oil	Coconut Oil	Extra Virgin Olive Oil	Grapeseed Oil	Hazelnut Oil	Olive Oil	Palm Oil
Caproic Acid	-	-	0.93%	-	-	-	-	-
Caprylic Acid	-	-	9.92%	-	-	-	-	-
Capric Acid	-	-	6.24%	-	-	-	-	-
Lauric Acid	-	-	46.00%	-	-	-	-	0.26%
Myristic Acid	-	-	18.21%	-	-	-	-	0.93%
Palmitic Acid	6.08%	10.89%	7.70%	10.30%	7.16%	5.22%	12.30%	37.90%
Palmitoleic Acid	-	-	-	0.73%	-	-	1.50%	-
Stearic Acid	2.01%	2.21%	2.54%	3.18%	3.84%	2.27%	1.60%	4.23%
Oleic Acid	58.70%	31.40%	6.82%	77.21%	22.40%	76.60%	69.70%	44.82%
Linoleic Acid	22.50%	55.10%	1.65%	7.26%	66.60%	15.90%	12.30%	11.90%
Linolenic Acid	1.11%	0.41%	-	0.41%	-	-	0.50%	-
Arachidic Acid	1.06%	-	-	0.95%	-	-	1.07%	-
Eicosenoic Acid	8.56%	-	-	-	-	-	-	-
Behenic Acid	-	-	-	-	-	-	-	-

	Peanut Oil	Rapeseed Oil	Rice Bran Oil	High Oleic Safflower Oil	Sesame Oil	Soybean Oil	Sunflower Oil	Walnut Oil
Caproic Acid	-	-	-	-	-	-	-	-
Caprylic Acid	-	-	-	-	-	-	-	-
Capric Acid	-	-	-	-	-	-	-	-
Lauric Acid	-	-	-	-	-	-	-	-
Myristic Acid	-	-	0.53%	-	-	-	-	-
Palmitic Acid	9.03%	3.91%	20.60%	5.39%	9.24%	9.82%	7.19%	8.23%
Palmitoleic Acid	-	-	-	-	-	-	-	-
Stearic Acid	2.58%	2.14%	2.05%	2.83%	5.54%	4.45%	4.20%	2.40%
Oleic Acid	43.10%	63.40%	40.90%	74.70%	40.40%	26.00%	24.90%	18.18%
Linoleic Acid	38.80%	20.40%	33.60%	17.00%	44.80%	52.90%	63.70%	59.50%
Linolenic Acid	-	9.52%	0.60%	-	-	6.82%	-	11.70%
Arachidic Acid	1.22%	0.40%	1.67%	-	-	-	-	-
Eicosenoic Acid	2.06%	0.18%	-	-	-	-	-	-
Behenic Acid	3.19%	-	-	-	-	-	-	-

The fatty acid composition of a variety of edible vegetable oils. (Figure adapted with permission[143])

The iron precursor for magnetite nanocrystal preparations can also be replaced with a common item: finely ground rust collected from refuse. Iron salts soluble in water are generally poor choices for this process as they do not readily dissolve in organic solutions;

however, crystalline iron oxides or hydroxides can be effectively dispersed in fatty acids at moderately high temperatures (ca 180 °C). The yellow to orange colors of the solution are generally of high clarity and arise from iron carboxylate precursors that form with the fatty acids. In a conventional reaction, bulk iron oxides or salts are first dissolved at lower temperatures in fatty acids to form iron carboxylates; these are then decomposed at higher temperatures to yield nanocrystalline iron oxides.[144] The best and most economical iron source is rust which is a mixture of iron hydroxides, oxides and in some cases even zero-valent iron;[145] rusts collected through scraping of ferrous refuse dissolve in fatty acids under the same conditions as the conventional FeO(OH) material. If the rust was not allowed to completely dissolve and react to become iron carboxylates before the subsequent thermal decomposition process, unreacted iron(0) was observed in the x-ray diffraction of the final powders.

When a rust/FAM solution is heated to above 270 °C, it produces a black suspension similar in appearance to that made with laboratory reagents. The electron micrographs of these samples (Figure 4.4) indicate the presence of large and well-separated nanocrystals, and the selected area electron diffraction and x-ray diffraction (Figure 4.5) are consistent with the magnetite structure. The size of the iron oxide nanocrystals produced using FAM and rust can be controlled much in the same way as for laboratory reactions. If the FAM is used without dilution, the resulting nanocrystals are larger (37 nm) with a cubic habit (Figure 4.4).[140] The addition of a diluent (1-octadecene) lowers the effective ratio of fatty acid to iron resulting in more nucleation and ultimately smaller nanocrystals (Figure 4.6).[146, 147] For the sample shown, we used rust and FAM with a diluent (ODE) to generate smaller sizes,

0.1884 g of iron from a rusted stand from the laboratory fume hood, and a temperature of 322 °C for 55 minutes under reflux (solution integrity preserved).

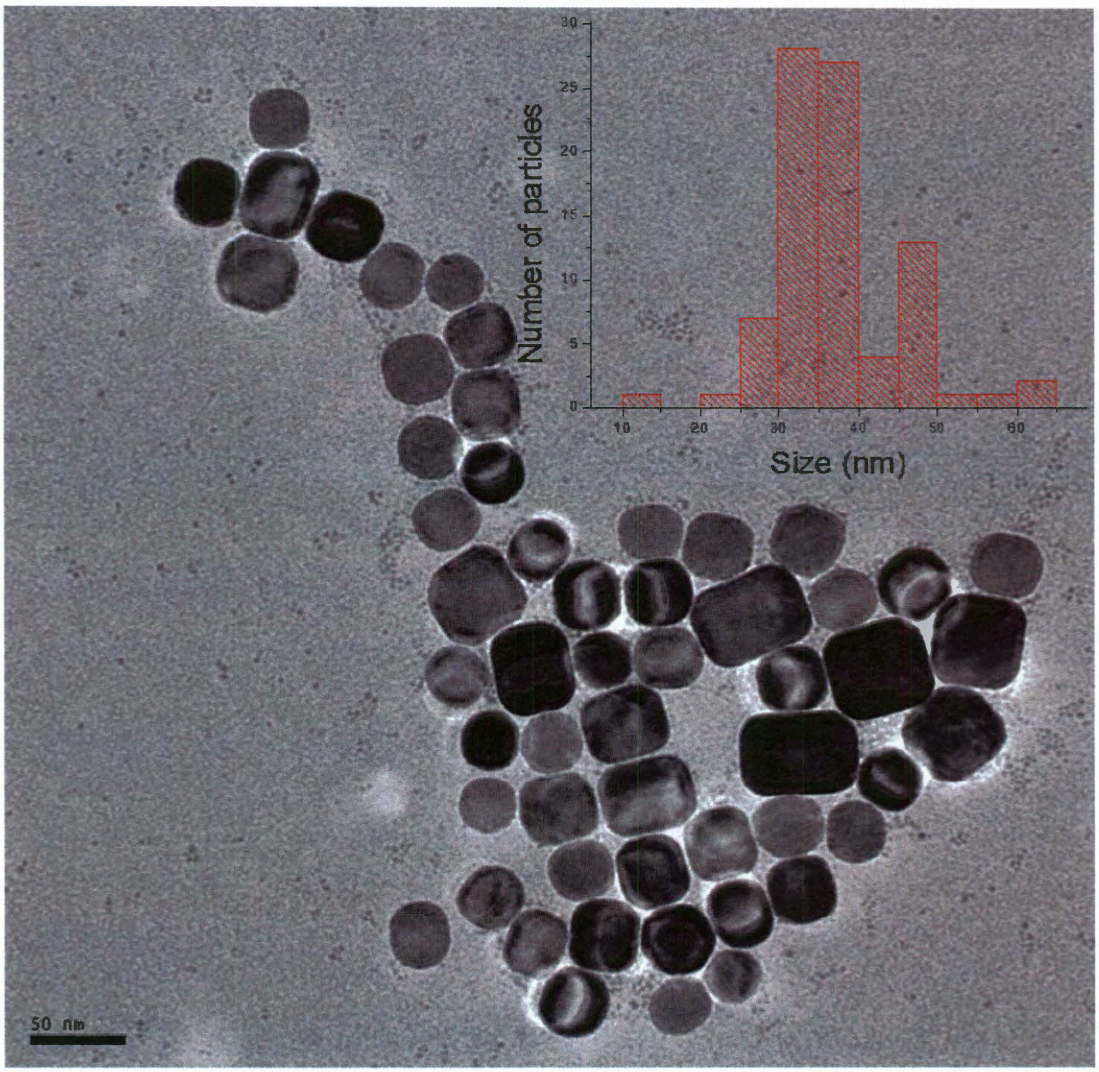

Figure 4.4 TEM image of kitchen synthesis magnetite
TEM image of 37.2 ± 7.9 nm magnetite produced in a pan with common household materials. This particular reaction took place for 90 minutes at 308 °C. The size distribution histogram is displayed as an inset.

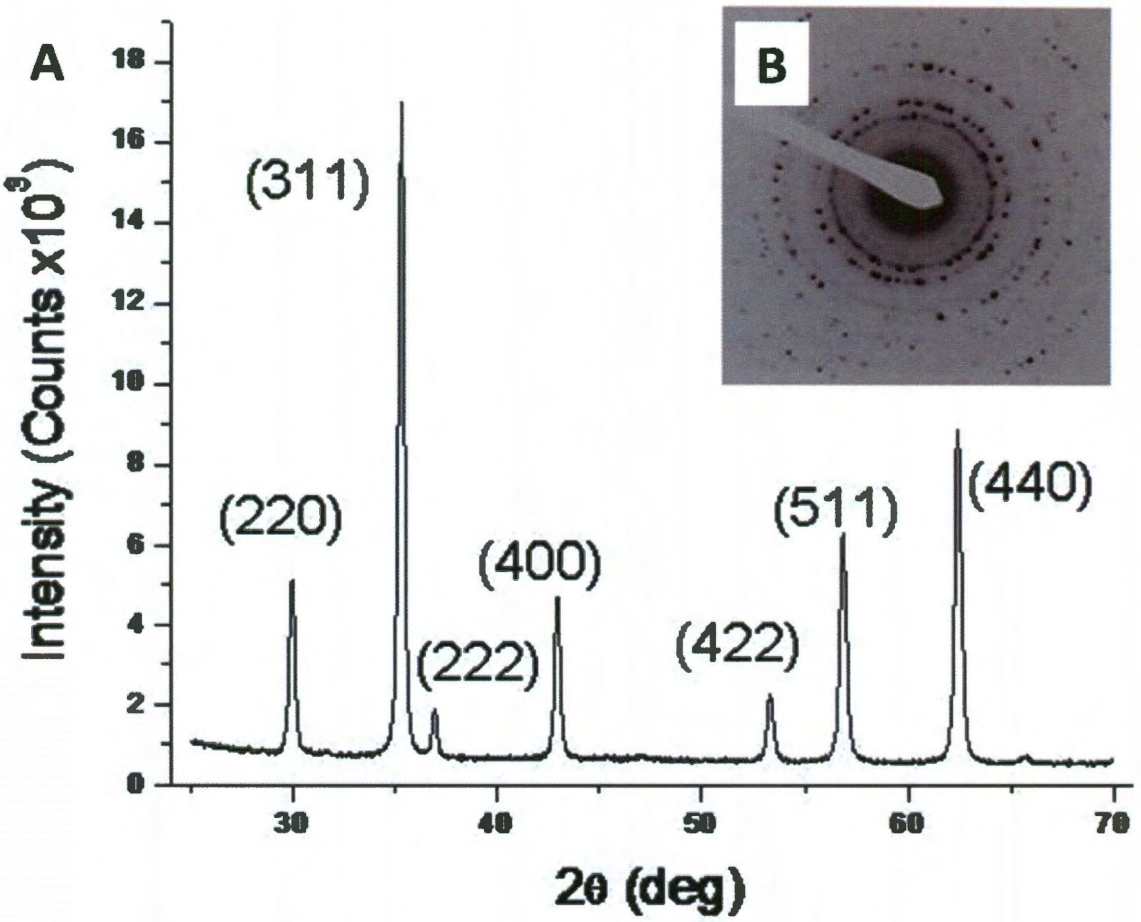

Figure 4.5 X-ray diffraction and selected area electron diffraction of kitchen synthesis magnetite
(A) X-ray diffraction of magnetite nanocrystals synthesized from everyday chemicals. (B) TEM selected area electron diffraction of as synthesized magnetite nanocrystals.

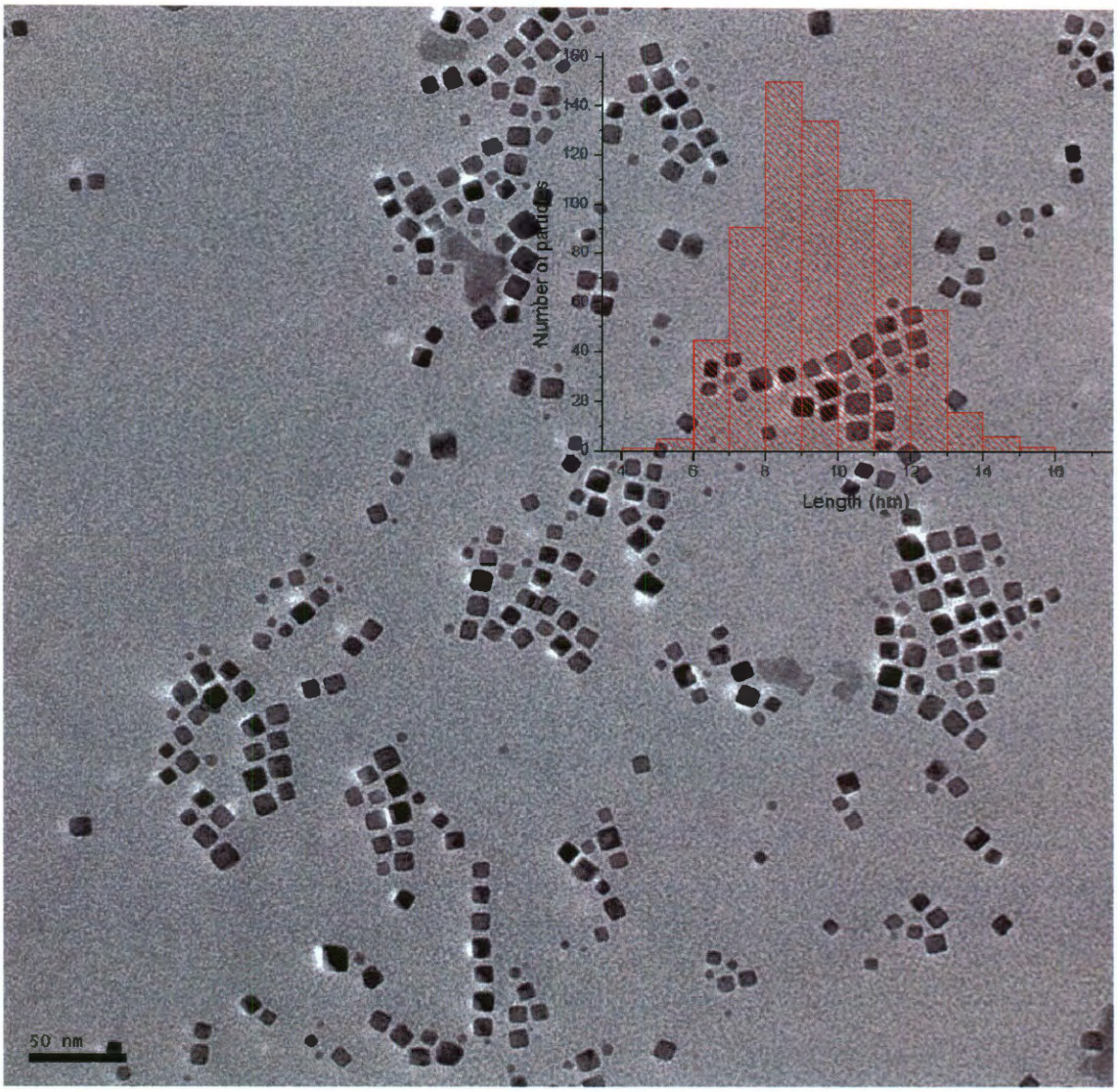

Figure 4.6 TEM image of kitchen synthesis magnetite with some laboratory chemicals
TEM micrograph of 9.65 ± 1.85 nm magnetite nanocrystals, synthesized with ODE added as a diluent, and magnetically separated in chloroform. Scale bar is 50 nm. The size distribution histogram is displayed as an inset.

The nanocrystalline product of the reaction is sensitive to the temperature of the FAM/rust mixture (Figure 4.7). Once temperatures are above ~280 °C the reaction will occur, and particle sizes increase as the temperature of the reaction approaches the boiling point of FAM (> 350 °C for the fatty acid mixture). A conventional frying pan enclosed loosely by a cover or tin foil was suitable for relatively constant temperature control; the

FAM may oxidize at these temperatures in air but our group has found this to have little impact on the reaction products.[22] While testing kitchen equipment in our laboratory setting, we found we could vary nanocrystal size over a wide range, while retaining reproducibility batch to batch of 10 % for the diameter. Restaurants and home kitchens often are equipped to heat frying oil to comparable temperatures, and we note that if lower temperatures are desired then edible oils that yield shorter chain fatty acids may be preferred.[22, 122]

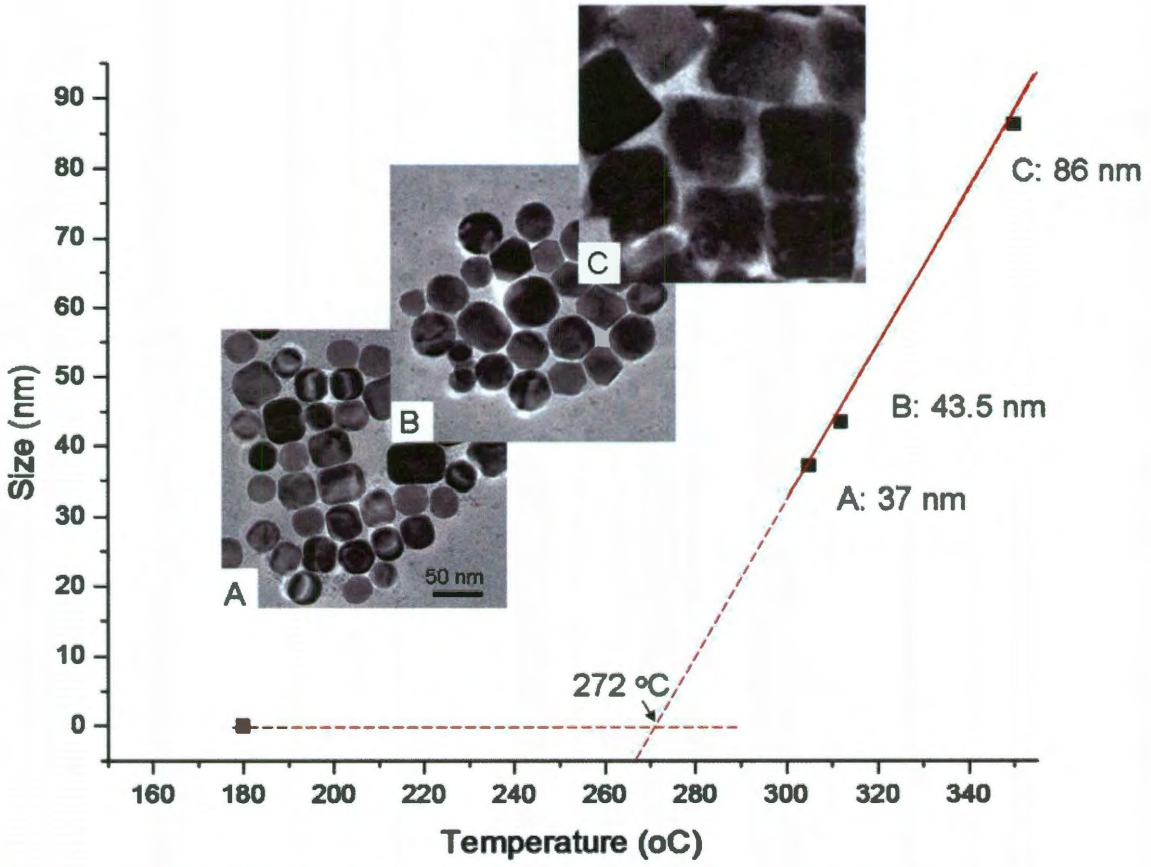

Figure 4.7 Temperature dependence of kitchen synthesis of magnetite nanocrystals
Note that there are no nanocrystals at 180 °C. (a) 37 ± 7.9 nm magnetite nanocrystals were obtained at 308 °C. (b) 43 ± 16 nm magnetite nanocrystals were achieved at 312 °C. (c) 86 ± 12 nm magnetite nanocrystals were collected when cooked at 350 °C (near boiling point).

Figure 4.7 illustrates the importance of the decomposition temperature to size control. As the temperature of the reaction increases, the particle size increases. In a laboratory environment this provides a natural route to size control; however, in settings that lack thermal controllers or even accurate thermometers visual cues for thermal control are preferred. Figure 4.8 shows the apparent changes that develop as FAM/rust mixtures are heated; intermediate temperatures are possible to stabilize, but it is more reliable to run the process near the boiling point of the FAM which is near 310 to 330 °C, depending on the FAM source. Thermal decomposition proceeds quickly and blackish-brown products develop within several minutes. However, materials left for at least two hours have the best uniformity. Transmission electron microscopy of the materials (Figure 4.4 and Figure 4.6) shows they are crystalline and in a cubic habit. The x-ray diffraction pattern indexes well to Fe_3O_4 though it is not possible to rule out Fe_2O_3 (Figure 4.5). Either phase of iron oxide is suitable for a magnetically active sorbent.

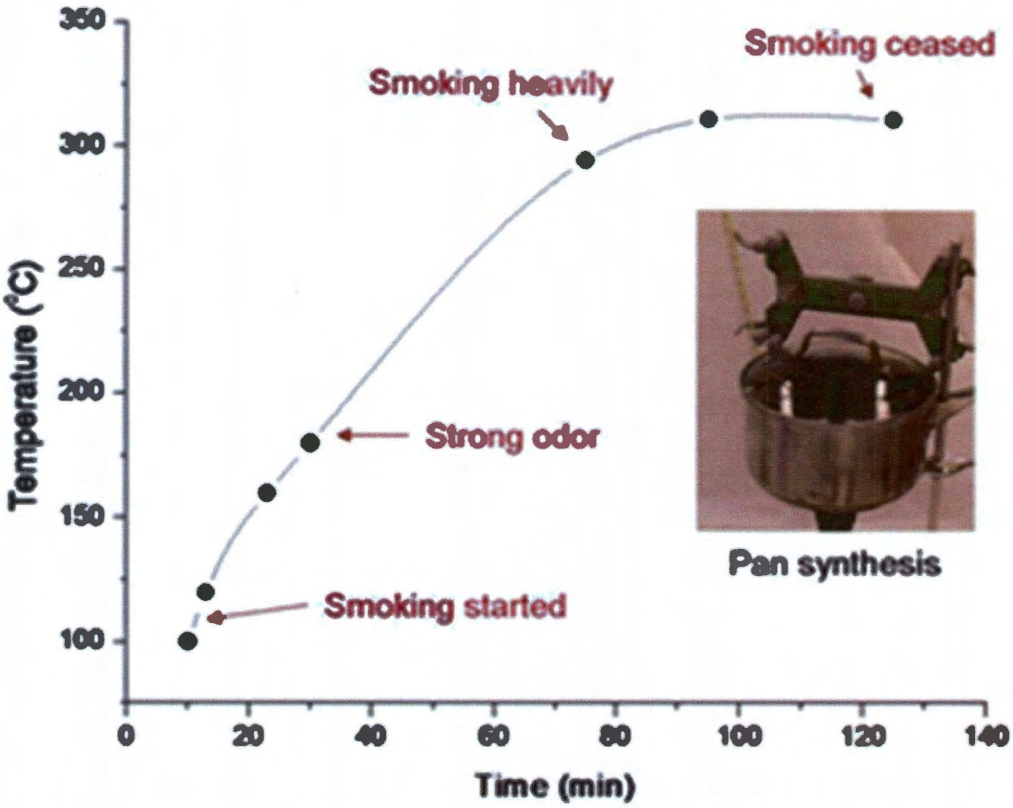

Figure 4.8 Visual cues from kitchen synthesis
As the temperature increases above 100 °C, a gas evolves from the reaction mixture, most likely due to excess water boiling away. At approximately 180°C, a strong odor begins to be emitted. This temperature likely corresponds to the formation of the iron carboxylate precursor. At approximately 300°C, the temperature begins to remain constant. At this temperature gas will begin to evolve heavily for a while but will eventually cease. When the smoking ceases, the reaction is complete.

If the reaction is completed correctly, the black product that forms can be separated from the solution using a handheld magnet (Figure 4.9). The magnetic separation of the nanoparticles is a very important feature of this process. In conventional laboratory settings, purification of nanocrystals from solution is a lengthy process that requires expensive and large centrifuges. An alternative, inexpensive method of purification is desirable. The easily evaluated magnetic properties can also confirm the crystallinity and size of the resulting material, which is useful in the absence of electron microscopy facilities. If the sample responds to the magnet, then the sample has likely produced a crystalline product. To

confirm that the product was functional as an arsenic sorbent, it was washed several times and packed into a sand column as shown in Figure 4.10. A full optimization of this fixed bed configuration is beyond the scope of this work, and because the materials are not affixed to the sand water flow does result in some minimal loss of iron material. However, as shown in Figure 4.11 it is possible through gravity filtration to significantly lower the arsenic levels of water samples to below the recommended 10 ppb limit.

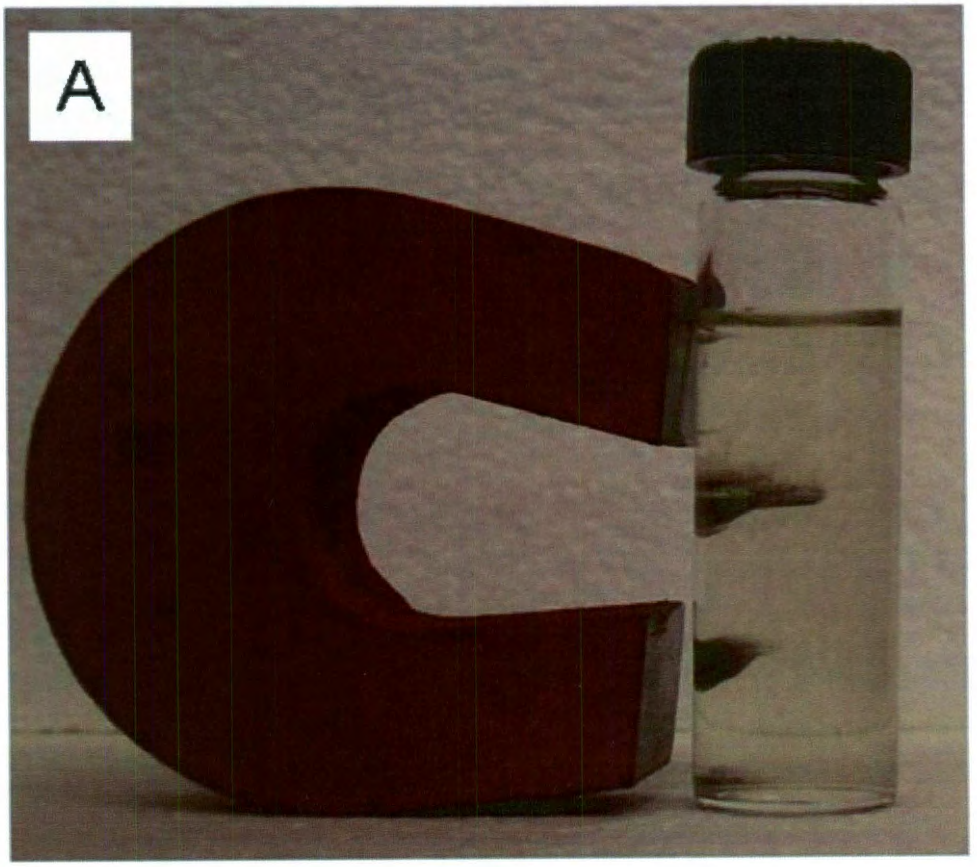

Figure 4.9 Magnetic purification of magnetite
Magnetic separation of homemade magnetite nanocrystals with a horse shoe magnet (0.13 T).

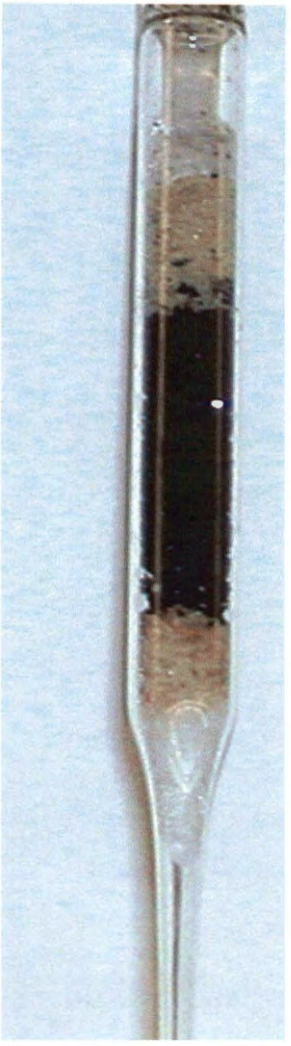

Figure 4.10 Magnetite-sand column
Glass column containing home made magnetite packed in sand for water purification.

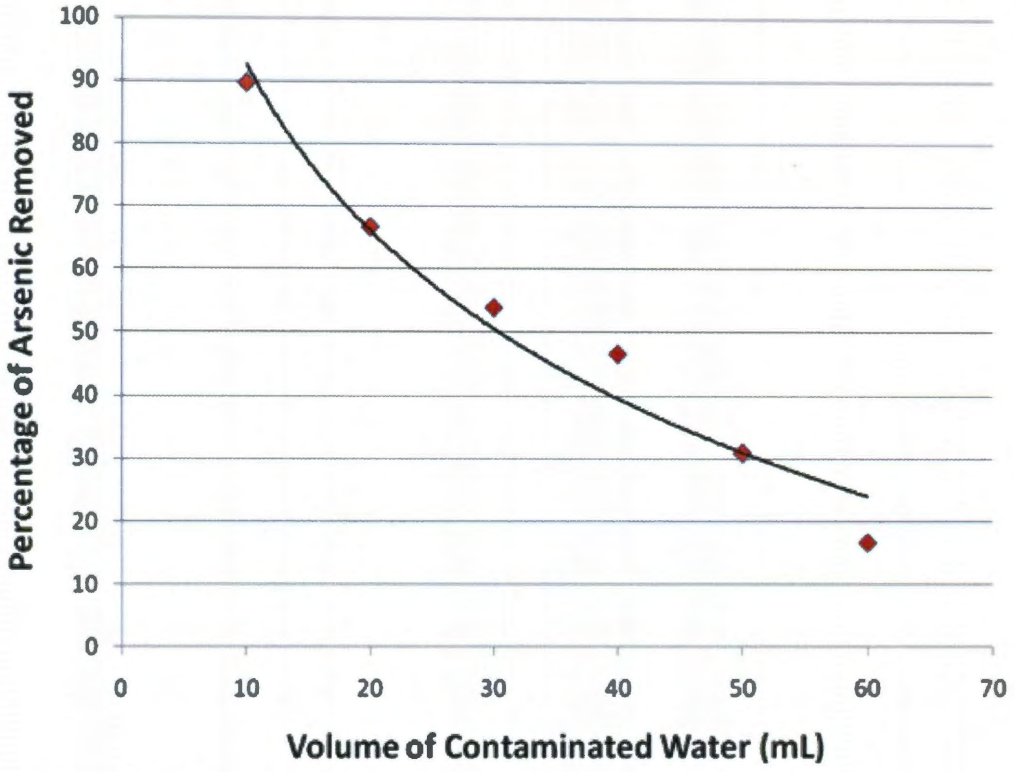

Figure 4.11 Kitchen synthesis nano-magnetite adsorption of As(V)
Remediation of arsenic based on gravity feed filtration utilizing a magnetite-sand packed column.

To explore the generality of our approach, we also produced quantum dots using laboratory precursors but with FAM from olive oil and in equipment with limited temperature control. These systems are a much more stringent test for appropriate manufacturing methods in that their size distributions are well known to be highly sensitive to solvent purity, reaction temperature, and additives such as phosphonic acids.[120, 122] The process yielded cadmium selenide nanocrystals that are functional in that they have size-dependent and strong emission characteristics of a quantum dot material (Figure 4.12). However, the materials are not uniform in size and the absorption spectra lack a well-defined peak typically observed for monodisperse samples (Figure 4.12). The incorporation of additives such as phosphonic acids are likely to improve the size distributions, but we note

that some users may find the as-prepared optical materials useful as broadly absorbing films for sunlight.[120]

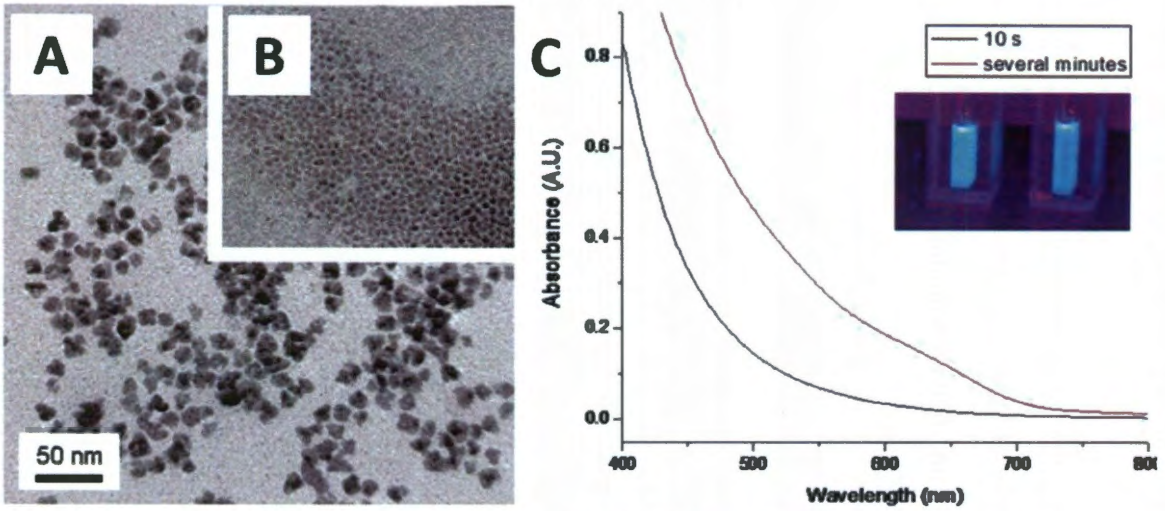

Figure 4.12 Cadmium selenide quantum dots from the kitchen synthesis
(A) TEM micrograph of 12 ± 2.7 nm CdSe nanocrystals made by dissolution of Se in fatty acid mixture (FAM) with little trioctylphospine (TOP) and heating, followed by an injection of CdO in FAM until the recovery at several minutes later and (B) 4.7 ± 0.7 nm CdSe nanocrystals at 10 seconds after injection. (C) UV-Vis absorption plots of two different sizes (lower, black plot: B, upper, red plot: A). (Inset) Digital picture of CdSe nanocrystals solutions (left:B, right:A) under UV light (366 nm).

An important element of this approach to nanocrystal production is the ability to get rapid feedback on the reaction products using simple tools. Such information is central if these methods are to be adapted and improved by local parties. We examined whether the functional properties of these nanocrystals could serve as the basis for evaluating the material quality. Figure 4.9 shows that a handheld magnet applied to a solution of nanocrystalline magnetite results in particle collection, and can replace more expensive evaluations of magnetic properties that rely on magnetometers. Its magnetic properties and solution color are an indication both of its size as well as crystalline quality.[18] Additionally, quantum dots can be evaluated using handheld ultraviolet lamps for their fluorescence yield, which is easily detected with the naked eye under normal light conditions.[148]

4.4 Conclusion

Here we show that nanoscale magnetite can be synthesized with materials commonly found in kitchens. These materials can be purified and phase transferred into water to be utilized for the removal of arsenic from drinking water. This work also shows that it is possible to create functional and high quality nanocrystals using methods appropriate for manufacturing in diverse and low infrastructure settings. We suggest that the transfer of this knowledge is best achieved using the open source movement for guidance. FOSS has demonstrated in the case of software (e.g. Linux, Apache, and GNU) that when a working solution is legally available and well-coordinated, volunteers can and will work in parallel to innovate and adapt the solution to a vast array of circumstances. FOSS also works because of widely and cheaply available hardware; by analogy, nanotechnology's "source code" cannot rely on expensive, scarce, or extreme production methods, but must similarly make use of the most widely available platforms, as in our case of magnetite production. Taken together, these methods and the FOSS system may provide an alternative technology transfer process that encourages local innovation and micro-business using knowledge that is secured in a legal commons for all to use. Based on this preliminary work in magnetite production, we have begun a small-scale version of open source nanotechnology, and we encourage interested readers, and members of the global scientific community to participate (opensourcenano.net).

CHAPTER 5: MULTIPLEX HIGH GRADIENT MAGNETIC SEPARATION

5.1 Introduction

Many technologies have been developed for nanoscale iron oxides, including MRI imaging,[40] water purification,[27, 33] on-demand drug delivery,[41] and cell culture transfection.[42] The motive response of magnetic particles to external fields is central to their application. Even modest magnetic fields, on the order of millitesla, can be sufficient to concentrate nanocrystals from suspensions.[18] Such separations can be useful in minimal infrastructure settings for water purification.[140] In a biological setting, magnetic separation can result in the capture and release of nanoparticles and their cargo.[92] Further development of the nanoscale properties could lead to more complex detection, sensing, or separation applications.

There are various methods of fine size separation for nanomaterials including centrifugation,[124] salts-based size-selective precipitation,[149] size exclusion chromatography,[150] and diafiltration,[151] but these processes do not take advantage of the magnetic properties demonstrated by iron oxide nanoparticles. The magnetic separation of coated nanoscale iron oxides and a binary form of magnetic chromatography has previously been demonstrated by Moeser *et al.*[51] Here, we expand upon these standard approaches of magnetic separation by using varying field strengths which separate different particles based on their diameter. The process does not simply separate nanoparticles based on whether they move in response to a magnetic field; rather, it separates nanocrystals based on the magnitude of their response to applied fields. Thus, several different populations can be separated from a complex mixture, in what we term here a 'multiplexed' separation, in

analogy to a multiplexed analysis.[152] This capability is particularly critical for biotechnology where it is often desirable to separate more than one type of component from a complex mixture.[77, 90, 153] Alternatively, in the present example it enables the size distribution of magnetic nanocrystals to be sharpened using a method that is effective, fast, and consumes minimal solvent.

This multiplex separation scheme is based on the premise that as the magnetic field acting on a nanocrystal suspension is increased, the retained sample becomes enriched in smaller particles.[18, 154] This enrichment reflects the size-dependent behavior of the particles: a larger magnetic field is required to remove smaller nanocrystals at room temperature. The size dependence has been the subject of some study.[18, 56, 125] It is generally thought that in an external magnetic field, nanocrystals may reversibly aggregate and align their magnetic dipoles.[18] This is due to the fact that the particle sizes in question are superparamagnetic and, therefore, experience large magnetizations in the presence of magnetic fields while retaining no magnetization upon the removal of the external field.[56] The forces required to move particles of this size range within a magnetic separator require reversible aggregation, and are dependent on particle size, concentration, and magnetic Bjerrum length, which is explicitly detailed by De Las Cuevas *et al.*[56] The larger structures would have very large magnetic moments, and in an external magnetic field would experience substantial motive force.[18] The tendency for superparamagnetic materials to aggregate is expected to increase with particle size due, in part, to their larger magnetic susceptibilities.[56] In addition, Bégin-Colin and co-workers indicate that smaller sizes of iron oxide crystals are enriched with the less magnetic maghemite (γ-Fe_2O_3) as opposed to magnetite (Fe_3O_4) which would also contribute to their reduced response to an external field.[125]

5.2 Experimental Methods

5.2.1 Instrumentation

Magnetic separations of the nanoscale iron oxides were performed on an L-1CN S.G. Frantz Canister Separator High Gradient Magnetic Separator (HGMS)(Figure 5.1), equipped with a stainless steel canister column (6.3 x 25.4 x 222.3 mm, 35.5 cm^3) packed with stainless-steel wool (~50 μm wire diameter), with a packing volume of 5 % of the canister (~15 g stainless-steel wool). The iron content of the materials retained in the HGMS was quantitatively determined by a PerkinElmer Optima 4300 DV Inductively Coupled Plasma-Optical Emission Spectrometer (ICP-OES). To determine the size of the nanoscale iron oxides before and after separation a 2100 JEOL Field Emission Gun Transmission Electron Microscope (FEG-TEM) was used for imaging and Image Pro software was used for sizing.

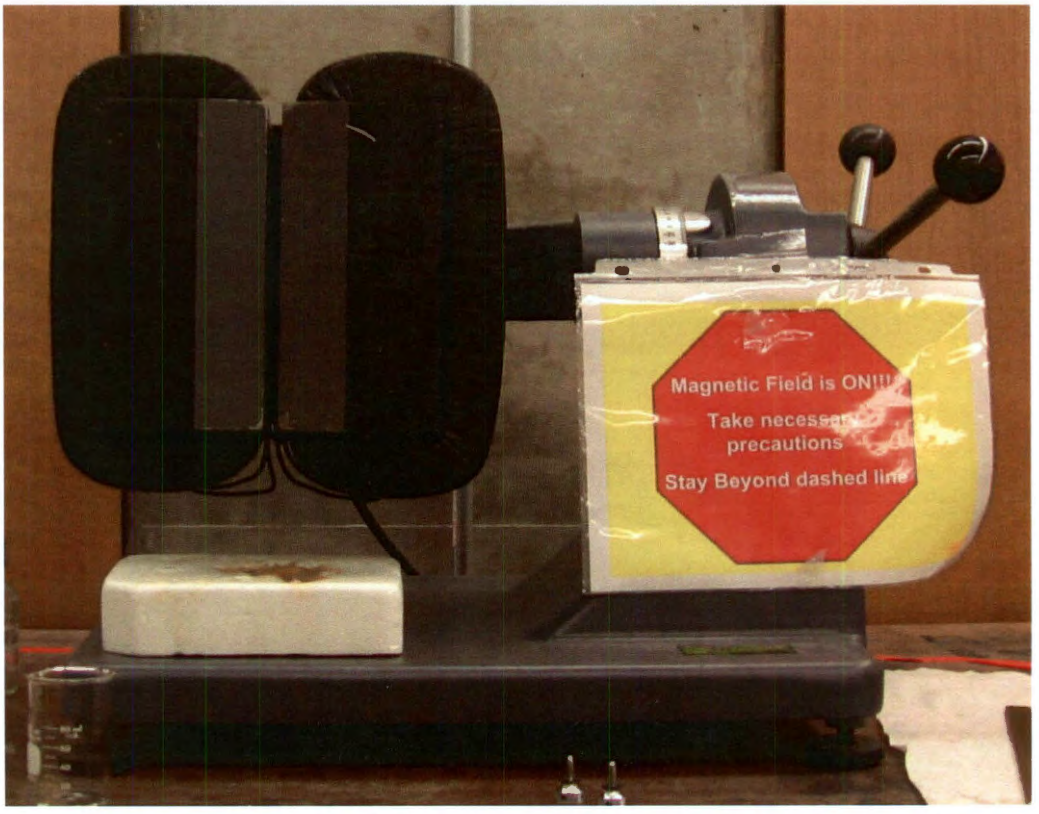

Figure 5.1 S.G. Frantz Canister Separator (model L-1CN)

5.2.2 Materials

FeO(OH) from Aldrich (iron(III) oxide, hydrated; catalyst grade, 30-50 mesh; cat. #371254) was ground to 100-150 mesh. Oleic acid (90% technical grade) and 1-octadecene (90% technical grade) were purchased from Aldrich. Hexanes (certified ACS grade) were purchased from Fisher Scientific.

5.2.3 Synthesis and Preparation of Nanoscale Magnetite

The size-dependent properties of iron oxide nanoparticles were evaluated to determine the optimal conditions for a multiplex magnetic separation. Four sizes of iron oxide nanocrystals were prepared via the thermal decomposition of iron oleate.[21, 22] The 4.0 nm iron oxide nanocrystals were synthesized by the thermal decomposition of 0.045 mmol iron oleate with 2 mmol oleic acid in 20 mmol 1-octadecene at 320 °C for 2 h. The 9.2 nm iron oxide was prepared by 1 mmol FeO(OH) with 3 mmol oleic acid in 40 mmol 1-octadecene at 320 °C for 30 min. The 11.7 and 15.9 nm iron oxide were prepared by reacting 10 mmol FeO(OH) with 40 mmol oleic acid in 28 mmol 1-octadecene at 320 °C for 1 h and 3h, respectively. Excess reactants in the as-prepared samples were removed by repeated cycles of flocculation upon ethanol and acetone addition, followed by centrifugation. The supernatant was then decanted and the precipitated particles were redispersed in a small quantity of hexanes. This process was repeated several times, and the resulting black suspensions were stored in hexanes with no evidence of aggregation over a period of months. These iron oxide samples were very uniform, and had average diameters of 4.0±0.4, 9.2±1.0, 11.7±1.1, and 15.9±1.4 nm (Figure 5.2).

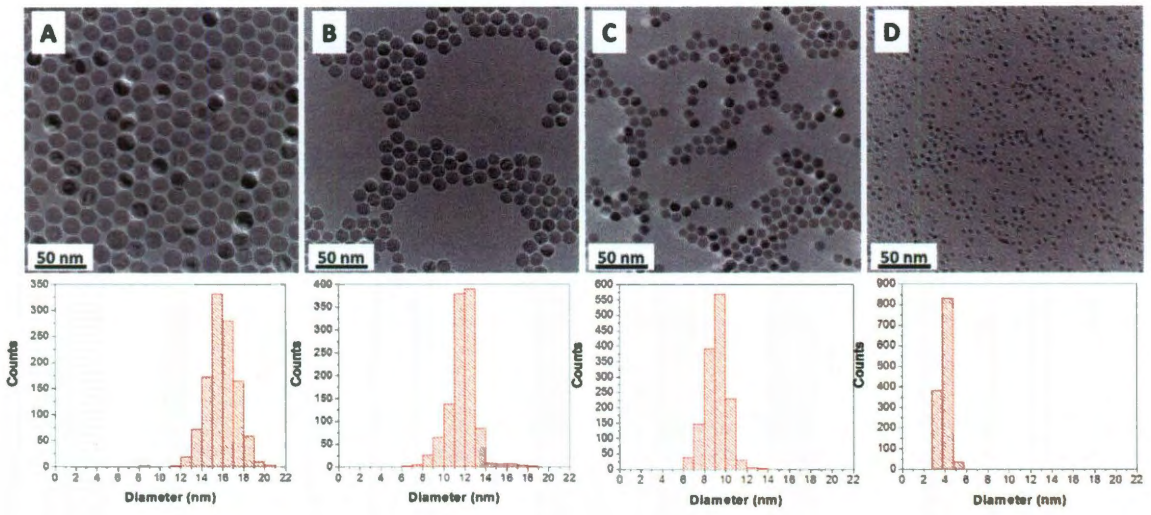

Figure 5.2 TEM images of nanoscale magnetite
TEM images of (a) 15.9±1.4 nm, (b) 11.7±1.1 nm, (c) 9.2±1.0 nm, and (d) 4.0±0.4 nm nanoscale iron oxide samples. Histograms are displayed below each image to show the size distribution.

5.2.4 Magnetic Separations of Nanoscale Magnetite

Different sizes of near-monodisperse nanoscale magnetite were passed through the HGMS at magnetic fields varying from 0 to 1.6 T to determine how efficiently the magnetite is retained in the column, similar to previous methods.[18] The samples were passed through the HGMS at gravity feed (~1 min), collected, and analyzed with comparison to the inserted sample by ICP-OES to determine the percent retention of the magnetite. A schematic of this system is shown in Figure 5.3. The data from this experiment was used to demonstrate the size-dependent properties of nanoscale magnetite and provide a guide as to which magnetic field strengths would be necessary for multiplex separations. The magnetic fields that were chosen for the multiplex separations were 0.05 T, 0.13 T, 0.23 T, and 1.59 T.

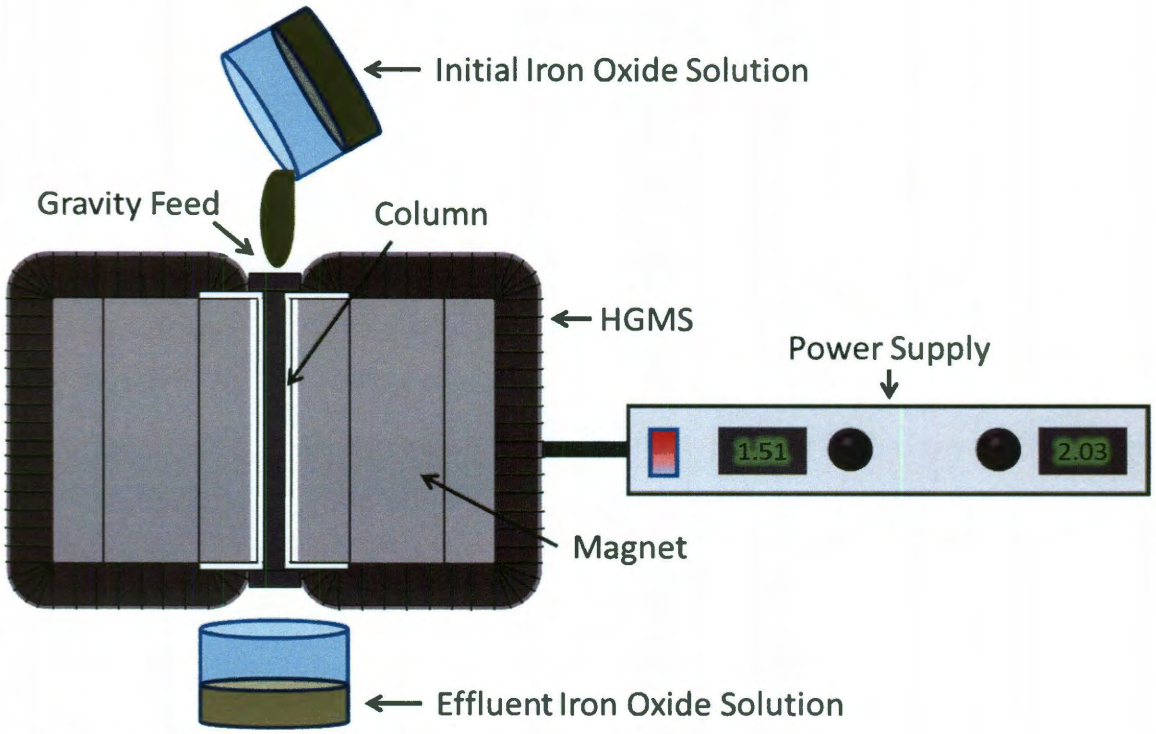

Figure 5.3 Schematic of the gravity feed HGMS experimental setup
The magnetic field strength is adjusted with the power supply and the iron oxide nanoparticle solution is passed through the column packed with stainless steel wool. The solution flow is gravity fed and only restricted by the packing density. Effluent is collected below.

5.2.5 Separation of Magnetite by Size through Magnetic Separation

The near-monodisperse magnetite nanoparticles shown in Figure 5.2 were combined to create a tetramodal magnetite sample that is approximately 1:1:1:1 particle to particle ratio. This mixed sample was passed through the HGMS at 0.05 T, retaining only the largest nanoparticles (15.9 nm) and allowing the smaller particles to pass through in the effluent. The magnetic field was then turned off, and the column was flushed with hexanes to collect the largest nanocrystals. The effluent from the HGMS at 0.05 T was then passed through the HGMS at 0.13 T; at this field strength the second largest iron oxide particles (11.7 nm) were expected to be preferentially retained in the column. After collecting this material from the column, the procedure was repeated at 1.59 T to retain 9.2 nm particles, and the 4.0 nm particles were isolated in the effluent. The magnetic field was then reduced to 0.23 T and the

9.2 nm sample was rinsed out. The final rinse was performed at 0.23 T rather than 0 T in order to reduce the release of larger particles that may potentially be present in the column. FEG-TEM images were taken of the final magnetite samples.

5.2.6 Analysis of Separation Data

The FEG-TEM images of the samples taken from the experiment above were analyzed with Image Pro sizing software. The size distribution data was fit with multiple Gaussian peak fits. Excel was also used to analyze the size distribution data. The initial size distribution data was compared with the resulting size distributions from separations. The enrichment of each size was mathematically optimized with respect to the desired size range as a variable to determine the actual size range that was enriched by the process and at what magnitude.

5.2.7 Sharpening Nanoscale Iron Oxide Size Distributions

An experiment demonstrating this process's ability to improve the size distribution of a polydisperse magnetite sample was also performed. A polydisperse 8.47 ± 2.50 (29.57 %) magnetite sample was passed through the HGMS at 0.17 T and rinsed with hexanes removing the smaller particles. The magnetic field was then reduced to 0.05 T and rinsed again with hexanes. This time the effluent was saved as the improved magnetite sample allowing the biggest particles to remain in the HGMS column.

5.3 Results and Discussion

The size-dependent response of these pre-mixed individual particles to an applied external field is shown in Figure 5.4. The HGMS applies a large external field to a narrow column (6.3 mm ID) filled with stainless steel wool; the steel wool creates regions of high

field gradients which serve to collect magnetic particles. While the exact values of the magnetic gradients are difficult to calculate in this geometry, they do scale with increasing applied field.[155, 156] For these studies, the particles were suspended in hexanes and gravity fed (~1 min) through the 22.3 cm long column. The effluent thus contained nanoparticles not captured by a particular applied field; the retained material could be recovered by removing the field and washing the column with additional hexanes. Quantitative analysis of the iron content of the starting suspensions and the effluent allowed for the calculation of the percent nanoparticles retained at varying applied magnetic fields.

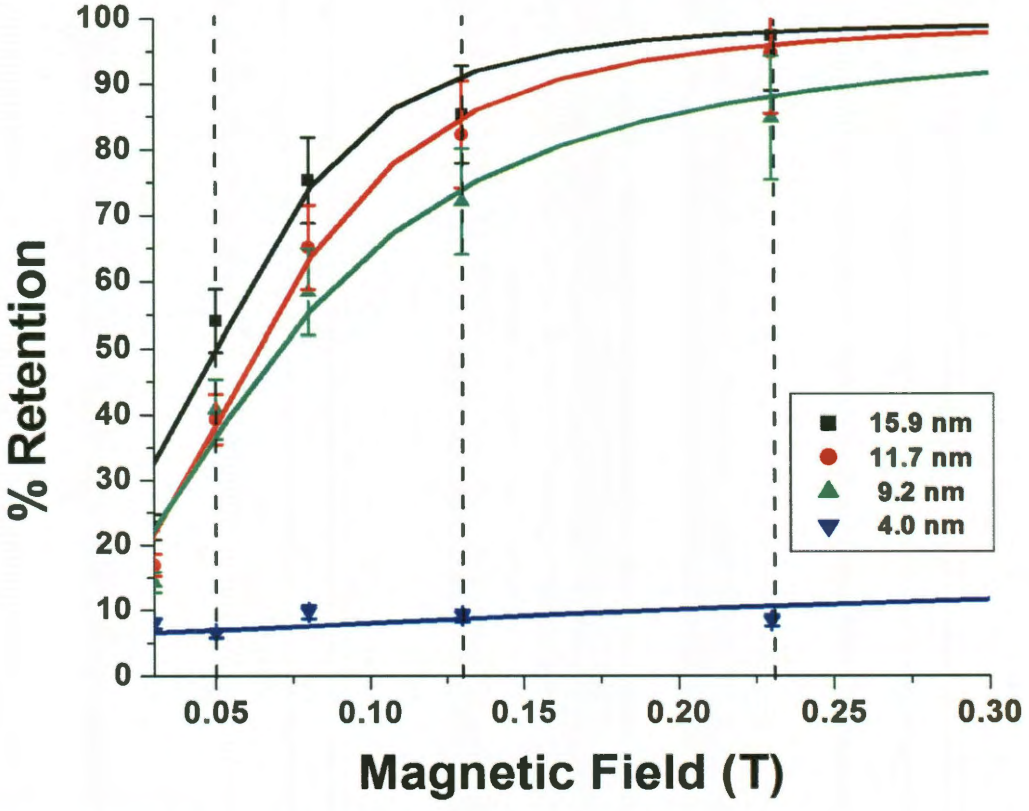

Figure 5.4 Size-dependent response of nanoscale magnetite to magnetic fields
These data illustrate the magnetic field required to retain the nanoscale iron oxide samples at specific particle diameters. This plot was utilized to determine the magnetic fields necessary for the tetramodal magnetic separation. Magnetic field strengths used in this experiment are marked with dashed lines.

Figure 5.4 shows the percent of nanoparticles retained in the column as the external field strength was increased from millitesla to 1.6 T. As expected, the smallest particles were the least retained by the column. Even at field strengths as high as 1.6 T (not shown), less than 17% of the material was captured by the column. In contrast the larger particles were almost completely retained (98 %) at only 0.23 T. The intermediate diameters exhibited retention characteristics between the large and small extremes. This data suggests that by varying the applied fields (vertical lines in Figure 5.4) it would be possible to selectively retain particles based on their size. For this process, magnetic fields of 0.05 T, 0.13 T, 0.23 T, and 1.59 T were used.

The four sizes of nanoscale iron oxides were then combined (Figure 5.5) to form a multimodal sample with distinct populations of iron oxide. The diameters of these materials were different enough to be distinguished in transmission electron microscope (TEM) images as illustrated by the colored circles in Figure 5.5. The mixed sample was initially passed through the HGMS at a very small external field (0.05 T). As expected from Figure 5.4, the largest iron oxide particles (15.9 nm) were preferentially retained in the column and enriched to 42 % of the sample in the first pass. The magnetic field was then turned off, and the column was flushed with hexanes to collect the largest nanocrystals. The effluent from the HGMS at 0.05 T was then run through the HGMS at 0.13 T; at this field strength the second largest iron oxide particles (11.7 nm) were preferentially retained in the column and enriched to 38 % of the sample. After collecting this material from the column, the procedure was repeated at 1.59 T to retain 9.2 nm particles, and the 4.0 nm particles were isolated in the effluent at 84 % of the sample. The magnetic field was then reduced to 0.23 T and the 9.2 nm sample was rinsed out at 65 % of the sample. Each of the four collected samples were

analyzed on the TEM (Figure 5.6). The resulting particle size distributions, shown in Figure 5.7, were determined using Image Pro sizing software.

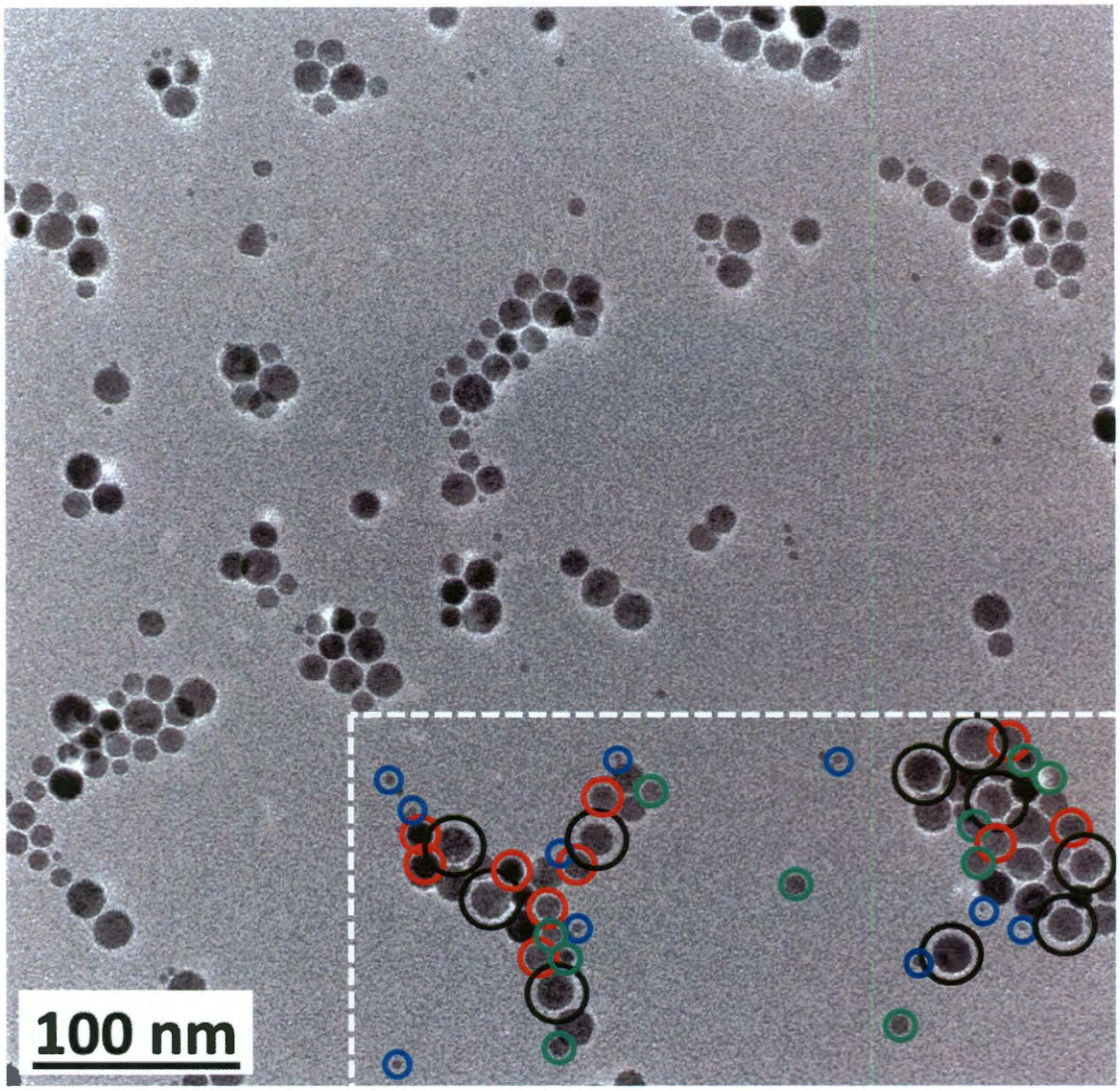

Figure 5.5 TEM image of tetramodal nanoscale magnetite sample
TEM images of mixed tetramodal iron oxide nanocrystal sample produced by quantitatively mixing four monodisperse iron oxide samples. In the dashed box, selected particles are circled to indicate their size: black for the 15.9 nm particles, red for the 11.7 nm particles, green for the 9.2 nm particles, and blue for the 4.0 nm particles.

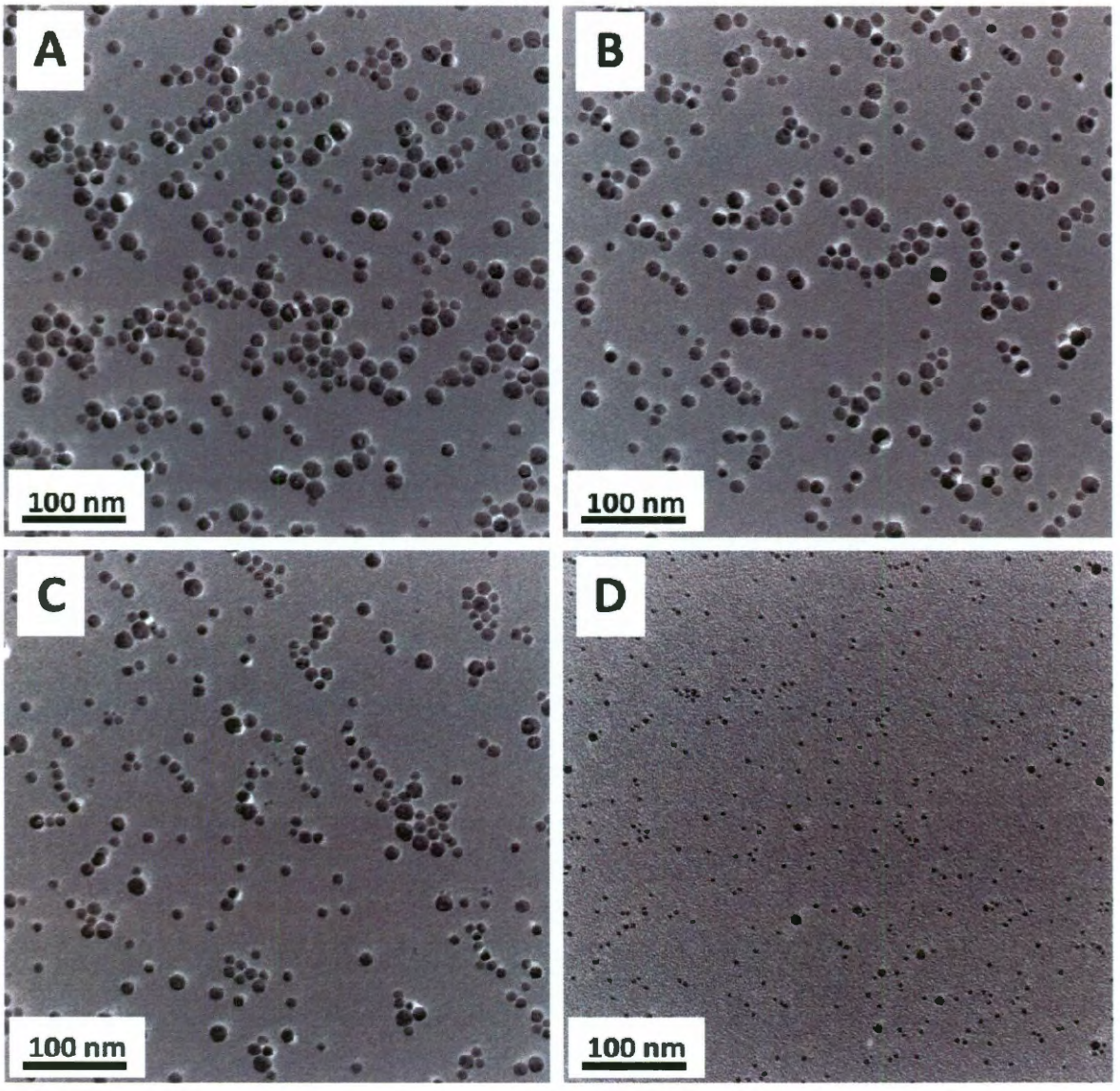

Figure 5.6 TEM of separated tetramodal nanoscale magnetite sample

TEM images of iron oxide samples obtained from the retained material (A) at 0.05 T, (B) at 0.13 T, (C) at 1.59 T, (D) and from the effluent at 1.59 T.

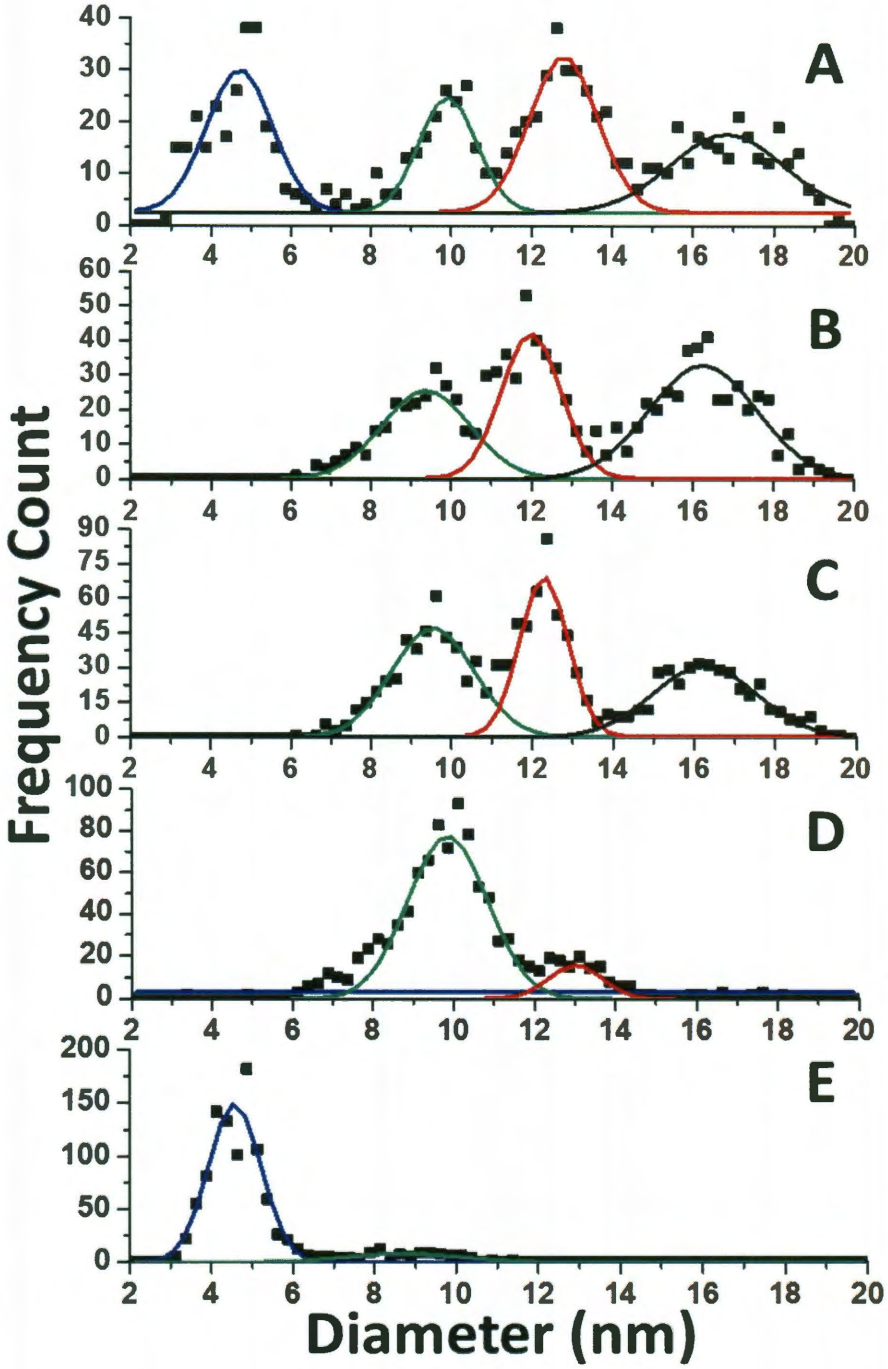

Figure 5.7 Size distributions of separated nanoscale magnetite samples
Distributions of nanocrystal diameters for the (A) starting tetramodal iron oxide sample and for the iron oxide samples obtained from the retained material (B) at 0.05 T, (C) at 0.13 T, (D) at 1.59 T, (E) and from the effluent at 1.59 T.

Figure 5.7 shows that it is possible to separate nanoparticles based on size using variable field applications. However, it is apparent in the data that the larger nanocrystals do not separate as well as the smaller materials. For example, in just one pass through the column the smallest size (4.0 nm) is separated relatively cleanly; fewer than 16 % of the material in this sample contained the larger sizes. In contrast, at lower field strengths the resulting effluents show enrichment in a particular particle size relative to the others rather than a complete separation. Such data is consistent with Figure 5.4 which shows the differences in response to applied magnetic fields is less pronounced as particle sizes increase. These observations result from the fact that the magnetic properties of these materials change most drastically when diameters fall below 27 nm.[157] This is in part due to the fact that for isolated particles in the superparamagnetic regime, the magnetic moment decreases with diameter.[125] However, iron oxide nanoparticles have been shown to form chains under the influence of an applied magnetic field.[158] Additionally, linear or network aggregation of larger particles may occur even without an external magnetic field.[159] This could prematurely induce aggregation which would make it more difficult to distinguish larger particles based on their isolated or non-aggregated diameters.

This variable field separation does not immediately lead to a baseline separation of particles under the conditions studied. Rather, the process creates samples that are enriched in a particular particle diameter. To quantify this enrichment as a function of diameter, we calculated the separation efficiency from the purity of the recovered materials. We defined the relative abundance, R, in a separated sample as:

Equation 5.1

$$R = \frac{F}{1 - F}$$

where F is the fraction of iron oxide nanocrystals within a specified diameter range. The enrichment factor, α, was then found from:

Equation 5.2

$$\alpha = \frac{R_f}{R_i}$$

where R_i and R_f, are the relative abundance of the desired diameter range before and after magnetic separation, respectively.[160] For the experiments performed here, we achieved enrichment factors of 18.7 for diameters ranging from 1 to 5.5 nm; 6.7 for diameters from 5.5 to 10.5 nm; 1.8 for diameters from 10.5 to 13.5 nm; and 1.7 for diameters greater than 13.5 nm. The enrichment factors for all size ranges were greater than one, implying that productive enrichment is taking place.

These enrichment factors can also be used to estimate the performance of a variable-field magnetic separation under more optimized conditions. Enrichment processes often rely on separations which are applied multiple times. In this case, greater enrichment could be attained by using longer HGMS columns, or alternatively by successive exposure of a sample to the same magnetic field. Because little material remains in the column after it is demagnetized, the product yields per pass are quite high, making multiple treatments practical. For the two smaller samples, it is possible to achieve a relative abundance of 9, or 90% purity, through only two applications of the column (or twice as long of column). In contrast, six successive column passes are required in order to ensure 90% pure samples of the two larger particles.

The data presented here provides a novel example of a size-dependent magnetic multiplex separation of iron oxide nanocrystals. A distinct trend in separation was observed with diameter, and this could be applied to separate different nanoparticle sizes from a

mixture using a conventional HGMS column. Small size particles could be separated most effectively, yielding an 84% pure sample. In principle, more highly purified nanocrystal populations could be recovered either by using a longer column, or by relying on successive passes through the standard columns. In biological applications which conventionally use magnetic beads, a variable field separation with appropriately designed particle diameters could be used to separate more than one cell type or biomolecule from a complex mixture. An experiment demonstrating this process's ability to improve the size distribution of a polydisperse magnetite sample was performed on a polydisperse 8.47 ± 2.50 nm (29.57 % RSD) magnetite sample (Figure 5.8) that was passed through the HGMS at 0.17 T and rinsed with hexanes removing the smaller particles. The magnetic field was then reduced to 0.05 T and rinsed again with hexanes. This allowed the largest particles to remain in the column while the rest of the previously retained nanoparticles were collected as the improved magnetite sample. The final magnetite sample contained a much improved 11.31 ± 1.58 nm (14.01 % RSD) (Figure 5.9). In this example the relative standard deviation was cut in half, which is a significant improvement in the overall size distribution. This process effectively cuts the tails off of the Gaussian size distribution curve. In nanomanufacturing, this separation could be applied to sharpen the size distribution of non-uniform materials as well as separate particles from the solvents and surfactants used in preparation.

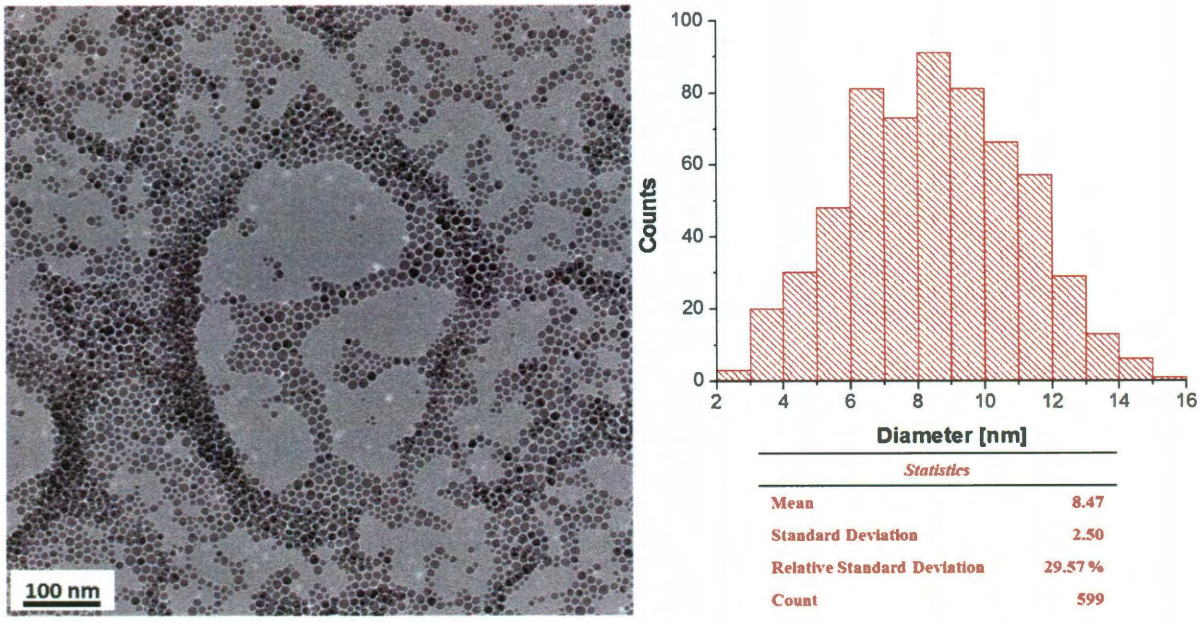

Figure 5.8 Polydisperse magnetite sample

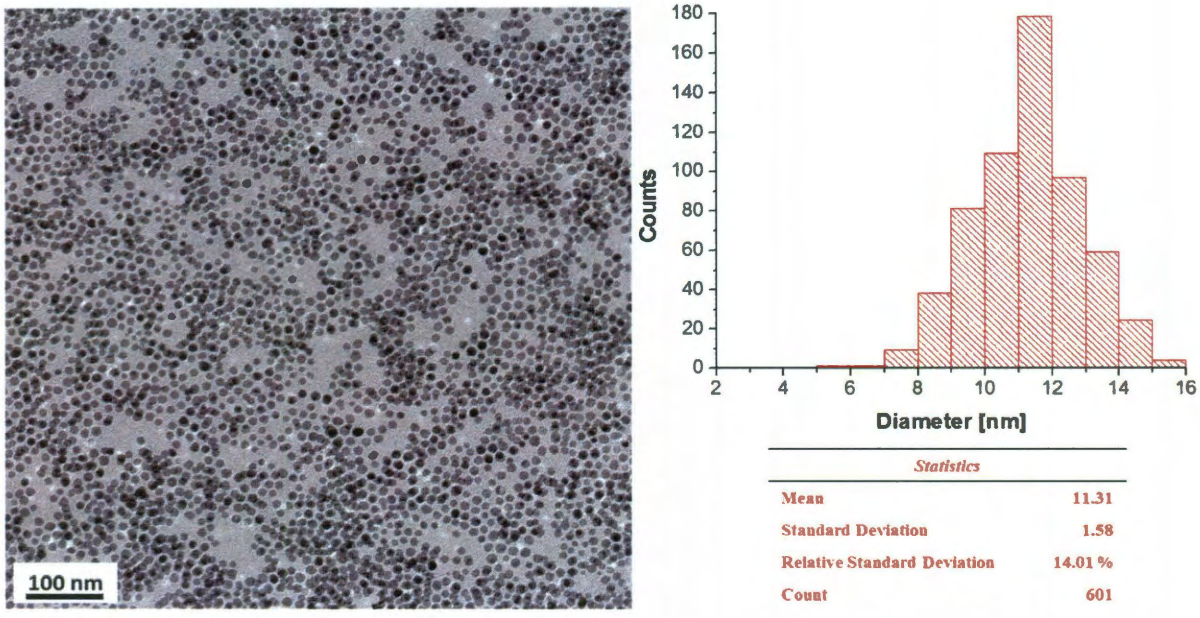

Figure 5.9 Magnetite sample with improved size distribution from magnetic separation

A method such as this could lead to improved biological multiplex separations, such as a multiplex separation of immunospecific cells. One such example of this would be to functionalize each different nMAG size with a distinct monoclonal antibody that has a specific affinity for a distinct type of cell.[77] Once combined with the cell mixture, the immunospecific cells could be separated simply by tuning the electromagnet. It could also enable the unique capture of different protein populations bound to distinct sizes of immunomagnetic particles. Alternatively, in nanomanufacturing it could supplant more laborious and slow purification processes designed to sharpen the size distribution of nanocrystalline magnetite.

5.4 Conclusion

In summary, the size-dependent properties of magnetic nanocrystals can be used as the basis for a variable magnetic field separation. We report for the first time the use of this principle for the enrichment of particular particle diameters in a complex mixture of four distinct diameter populations. The separation is particularly effective for distinguishing very small (e.g. 4 nm) from larger (e.g. > 12 nm) nanocrystals and for improving the size distribution of a magnetite nanoparticle sample.

CHAPTER 6: nMAG SIZE DEPENDENCE FOR ARSENIC ADSORPTION

6.1 Introduction

Arsenic-contaminated drinking water is a major problem around the world. Countries such as Bangladesh, India, Vietnam, Mexico, Argentina, Chile, Hungary, Romania, and the United States face significant challenges in meeting the newly lowered standards for arsenic in drinking water.[28] Several methods of arsenic removal are already available including precipitation, adsorption, ion exchange, solvent extraction, nanofiltration, foam flotation, and biological sequestration.[31] However, as recently noted, these technologies cannot perform well in actual field trials, and improved materials and systems are needed.[30] In particular, sorbents must be able to achieve a low arsenic level in drinking water for geographical areas with high arsenic concentrations. One option that has been explored is arsenic remediation using iron oxides. Many papers have been published demonstrating that bulk iron oxides have a high affinity for the adsorption of arsenite and arsenate.[28, 161, 162] Arsenic can form inner sphere monodentate, bidentate-mononuclear, or bidentate-binuclear complexes with iron oxides (Figure 6.1). Extended X-ray absorption fine structure spectroscopy has provided direct evidence for inner sphere adsorption of arsenite and arsenate on all types of iron oxides.[36, 163, 164] Studies can be found that analyze bulk, nanostructured films, and dispersed iron oxide nanoparticles.[18, 27, 33, 165]

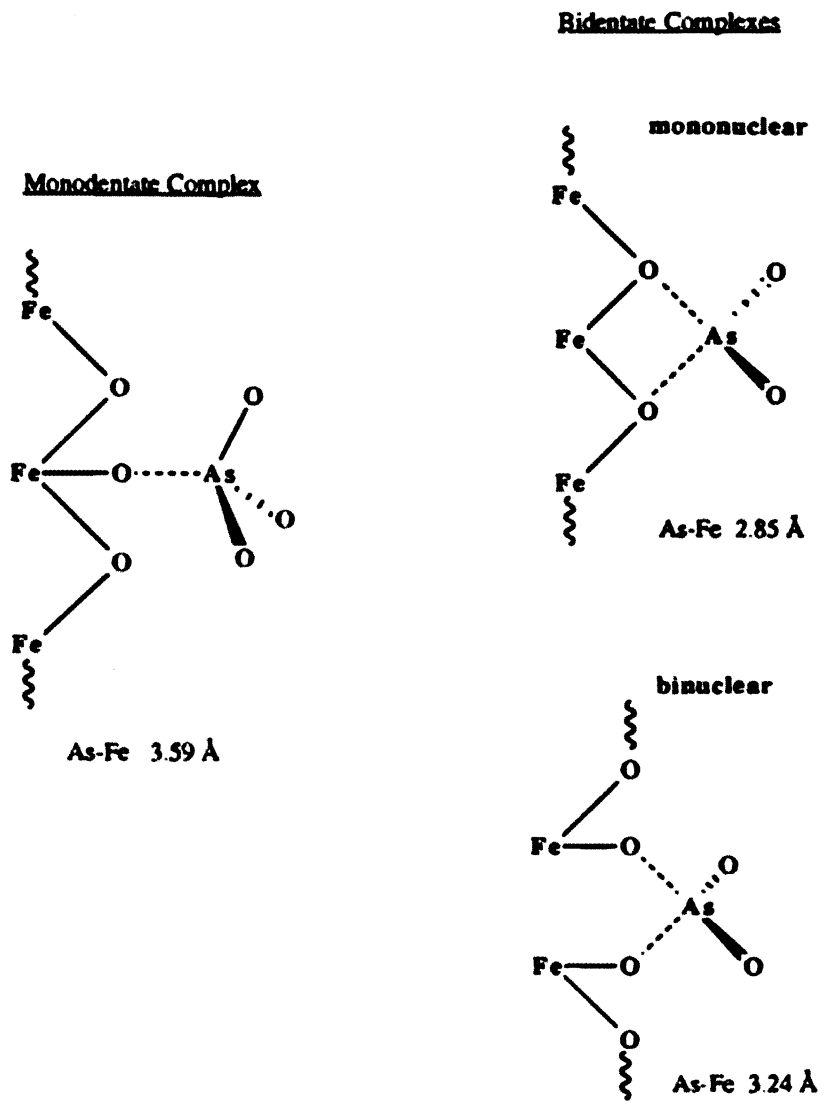

Figure 6.1 Inner sphere arsenic complexes with iron oxides
Inner sphere monodentate, bidentate-mononuclear, or bidentate-binuclear complexes of arsenate with goethite based on EXAFS spectroscopy. (Figure adapted with permission[36]).

Several types of iron oxides have been explored but nanoscale iron oxides in particular hold promise due to their increased surface area, reactivity, and size-dependent magnetic properties. Nanoparticle systems can be used either deposited on a substrate or dispersed in solution The sorption of arsenic onto nanostructured iron films has been studied and was found to be an efficient process with high arsenic retention.[166] However, such solid systems can have slow mass transport and complex recycling processes. Alternatively,

dispersed nanoparticles, which are homogeneously distributed in solution, have favorable mass transport to surfaces and can permit magnetic capture of depleted materials.[90] In addition, the magnetic separation of dispersed sorbents avoid many of the classical problems of filtration related to occluding and fouling of packed columns and membranes. Specifically for this work, magnetic separations are also possible for nanoscale materials. It has been shown that magnetite (Fe_3O_4) nanoparticles are highly efficient in biological separations because of the extremely small particle size and a large surface area without a high-mass-transfer resistance.[167]

In this work, we show the use of nanoscale iron oxide for remediation of arsenic. First we examine the effect of Fe_3O_4 particle size on the adsorption and desorption behaviors of arsenite ($H_3AsO_3^0$or $H_2AsO_3^{1-}$) and arsenate ($H_2AsO_4^{1-}$or $HAsO_4^{2-}$).[162] Then we compared laboratory synthesized magnetite versus commercially available magnetite and finally look at the effect of dispersion versus aggregation.[27, 33] The importance of particle dispersion against aggregation was also studied.

6.2 Experimental Methods

6.2.1 Instrumentation

The instrument utilized to magnetically separate the nanoscale iron oxides was an L-1CN S.G. Frantz Canister Separator High Gradient Magnetic Separator (HGMS), equipped with a stainless steel canister column (6.3 x 25.4 x 222.3 mm, 35.5 cm^3) packed with stainless-steel wool (~50 μm wire diameter), with a packing volume of 5 % of the canister (~15 g stainless-steel wool). Probe sonication for phase transfer was performed with a Hielscher UP100H Ultrasonic Processor or a Branson Digital Sonifier. Low speed centrifugation for purification was performed with a Fisher Scientific Marathon 22K. High-

speed ultracentrifugation for purification was performed with a Beckman-Coulter Optima L-80 XP Ultracentrifuge. Quantification of iron concentrations for sorbent materials and the iron content retained by the HGMS was a PerkinElmer Optima 4300 DV Inductively Coupled Plasma-Optical Emission Spectrometer (ICP-OES). Arsenic concentrations were quantitatively determined with a PerkinElmer Optima Elan 9000 Inductively Coupled Plasma-Mass Spectrometer (ICP-MS). Size determination of the nanoscale iron oxides before and after separation was performed with a JEOL 2010 Transmission Electron Microscope (TEM).

6.2.2 Materials

FeO(OH) from Aldrich (iron(III) oxide, hydrated; catalyst grade, 30-50 mesh; cat. #371254) was ground to 100-150 mesh. Oleic acid (90% technical grade) and 1-octadecene (90% technical grade) were purchased from Aldrich. Hexanes (certified ACS grade) were purchased from Fisher Scientific. A 20 nm magnetite sample was purchased from Reade Advanced materials, and a 300 nm magnetite sample was purchased from Sigma-Aldrich. Commercially available nanoscale magnetite (Sigma-Aldrich, Iron (II,III) oxide, nanopowder, <50 nm, 98+ %) was utilized for the aggregation effect experiments. Igepal® CO-630 was purchased from Sigma-Aldrich. The arsenic(V) and the arsenic(III) stock solutions were prepared by dissolving the corresponding arsenic oxides (As_2O_5 and As_2O_3) purchased from Sigma-Aldrich in de-ionized water with 4 g/L NaOH.

6.2.3 Synthesis and Preparation of Magnetite Nanocrystals

A scalable one-pot synthesis of magnetite nanocrystals was performed by mixing FeO(OH) (2.00 mmol), oleic acid (8.00 mmol), and 1-octadecene (20.00 mmol). The

mixture was heated with stirring at 320°C and kept at this temperature for a desired time, as seen in Yu *et al.*[22] The resulting nanocrystals were then made water soluble by methods similar to those seen in work performed by Landfester and coworkers[25] where 1 mL Fe_3O_4 nanocrystals in hexanes was added to 4 mL 10 wt% Igepal® CO-630 solution. The sample was then shaken and probe sonicated for several minutes. These samples were then centrifuged twice at 4500 rpm for 1 hour, removing excess surfactant from the top and sedimented aggregates from the bottom. The nanocrystals that remained suspended in solution were then collected by two rounds of ultracentrifugation at 50,000 rpm for 1 hour. The excess surfactant was decanted and the settled nMAG was redispersed in water.

6.2.4 Magnetic Separations

Magnetic separations were performed with a high-gradient magnetic field column separator packed with stainless steel wool. To separate the magnetite, a controlled magnetic field (1.6 T) was applied and a sample was passed through the column. The nanoparticles were retained in the column as the solvent passed through. When the magnetic field was removed and fresh solvent passed through the column, the nanoparticles were recovered (Figure 6.2). This process was necessary for the separation of the 12 nm magnetite in the sorption studies.

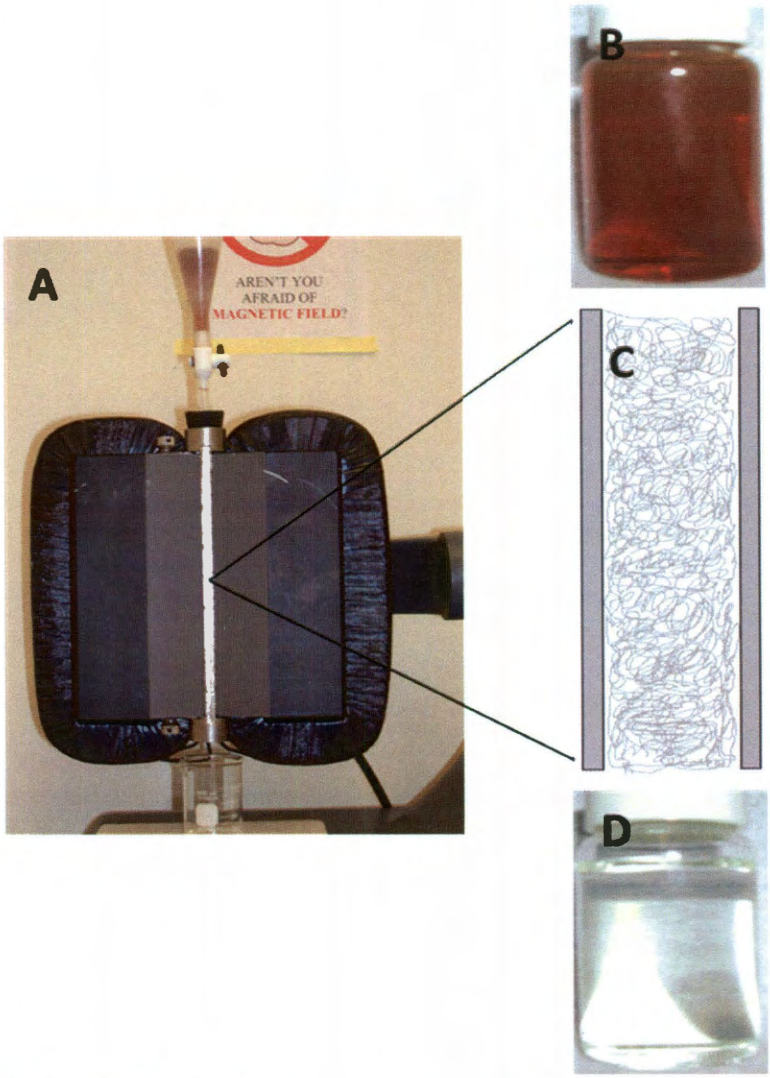

Figure 6.2 Schematic of magnetic separator.
A high-gradient magnetic field column separator (A) consisting of an S.G. Frantz Canister Separator (model L-1CN) was used for the magnetic separation experiments. The brown Fe_3O_4 suspension (B) was passed through a stainless-steel wool-packed column (C) within the magnetic separator. The colorless effluent (D) demonstrates the retention of magnetite.

6.2.5 Sorption

Sorption studies were performed on three sizes of magnetite, consisting of one laboratory synthesized material and two commercially synthesized materials, at arsenic concentrations ranging from 0 to 34 ppm. The concentrations of magnetite were 2.5 g/L and 0.1 g/L for commercially made 300 nm and 20 nm magnetite, respectively, and 0.011 g/L for

laboratory prepared 12 nm magnetite nanocrystals. Adsorption studies were conducted at pH 4.8, 6.1, and 8.0 for the commercial materials. A background electrolyte of 0.01M $NaNO_3$ was used for the adsorption studies. For the 6.1 and 8.0 pH experiments, 2(N-Morpholino)-ethanesulfonate (MES) and Tris at 0.005 M were added as buffers, respectively. For 12 nm magnetite nanoparticles, 0.01 M $NaNO_3$ and 0.01 M Tris buffer at pH 8 was used as an electrolyte background solution. A small of amount of trace metal grade HNO_3 or NaOH was used to adjust pH.

The magnetite arsenic mixtures were equilibrated on a slowly rotating rack that tumbled end-over-end (4 rpm) for 24 h, and then centrifuged at 4000 rpm for 30 min. The supernatant solutions of the 300 nm and 20 nm commercially made magnetite solutions were filtered through 0.2 μm Nalgene syringe filters (Surfactant-Free Cellulose Acetate, SFCA). For the 12 nm laboratory prepared magnetite, a magnetic field column separator was used to separate the solid from liquid phase. All experiments were performed in triplicate with the filtrates and precipitate analyzed for arsenic and iron by inductively coupled plasma-mass spectrometry and inductively coupled plasma-optical emission spectrometry, respectively.

6.2.6 Desorption

Desorption studies were conducted with the 20 and 300 nm magnetite at pH 6.1, by adding arsenic-free electrolyte to the arsenic-exposed magnetite nanoparticles which were previously used for a 24 h adsorption. Desorption experiments with 12 nm magnetite, however, were not performed because of limited samples. These samples were allowed to equilibrate for 24 h on a tumbler and centrifuged. The supernatant solution was pipetted into a syringe filter and filtered through 0.2 μm Nalgene syringe filters (SFCA). Successive desorption was performed by repeating the above desorption procedures two more times after

the supernatant solution was removed. Arsenic concentrations were then measured by ICP-MS. The solid phase concentration was calculated from the solution phase arsenic concentrations by assuming a mass balance.

6.2.7 Arsenic Adsorption and the Dispersion of Materials

In an effort to study the arsenic adsorption of a well-dispersed nanoscale magnetite as compared to aggregated nanoscale magnetite, commercially available magnetite nanopowder (<50 nm) was used. Samples of 0.4 g/L nanopowder in 1.5 to 48 ppm arsenic solutions at pH~7 were prepared and allowed to adsorb for 24 h while tumbling end-over-end at 4 rpm. For comparison, samples were prepared identically using nanopowder that had been previously sonicated in 0.7 wt% Igepal CO-630 to disperse the aggregates. Samples of arsenate in an aqueous Igepal CO-630 solution with the nanopowder (aggregated, not dispersed), and arsenate sonicated in an Igepal CO-630 solution before the addition of the nanopowder (aggregated, not dispersed) were compared as controls.

6.3 Results and Discussion

The synthesis of magnetite nanocrystals is successful at a variety of sizes with near-monodisperse size distributions.[22] These particles prepared in the laboratory can be easily dispersed in aqueous phase as described in the previous section. Commercially available nanoscale iron oxides, while more polydisperse, are available in large amounts and the two sizes (20 and 300 nm) are readily suspended in water.[22, 27] In addition to a difference in size, these commercial materials are also more aggregated in suspension than the laboratory prepared materials (Figure 6.3).

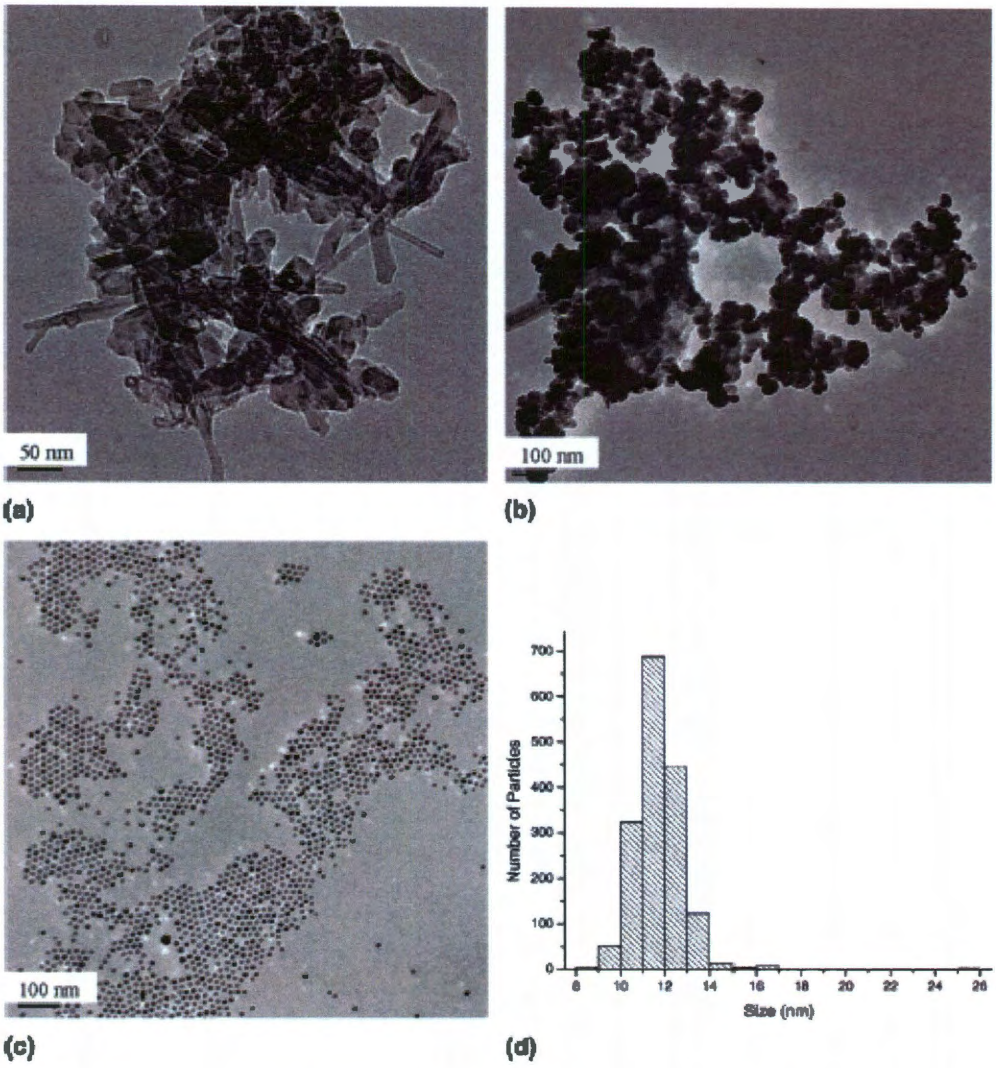

Figure 6.3 Comparison of magnetite nanomaterials by TEM
TEM image comparison of (a) 300 nm, (b) 20 nm, and (c) 12 nm magnetite displaying the improved dispersion of the laboratory synthesized 12 nm magnetite. (d) A histogram describing the size distribution of the 12 nm sample is included.

The dispersed magnetite nanocrystals can be removed from the solution through interactions with a magnetic column. The 20 nm commercially made nanocrystals were permanently retained in the column and could not be recovered, while the laboratory prepared nanocrystals were able to be recovered when the magnetic field was turned off

(Figure 6.4). Furthermore, when the magnetic field is increased, a greater percent of nanocrystals are retained in the column (Figure 6.5).

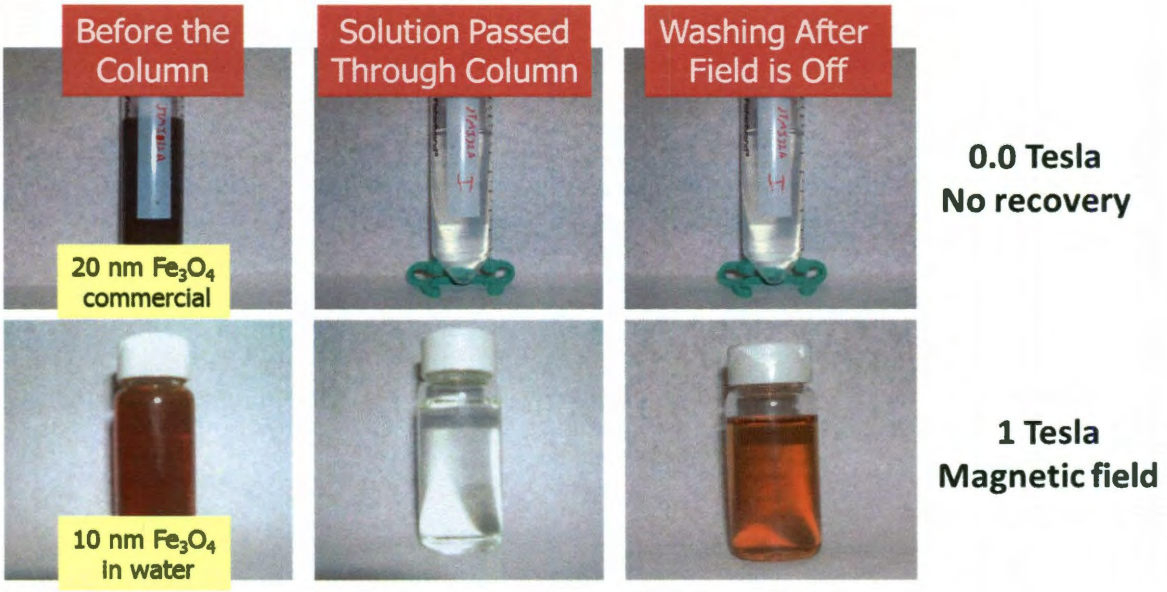

Figure 6.4 Magnetic separation of nanoparticles.
The top row shows 20 nm, agglomerated Fe_3O_4 in an aqueous solution and the effluent after passing through the magnetic column. The bottom row shows 10 nm, laboratory prepared Fe_3O_4 in an aqueous solution and the effluent after passing through the magnetic column.

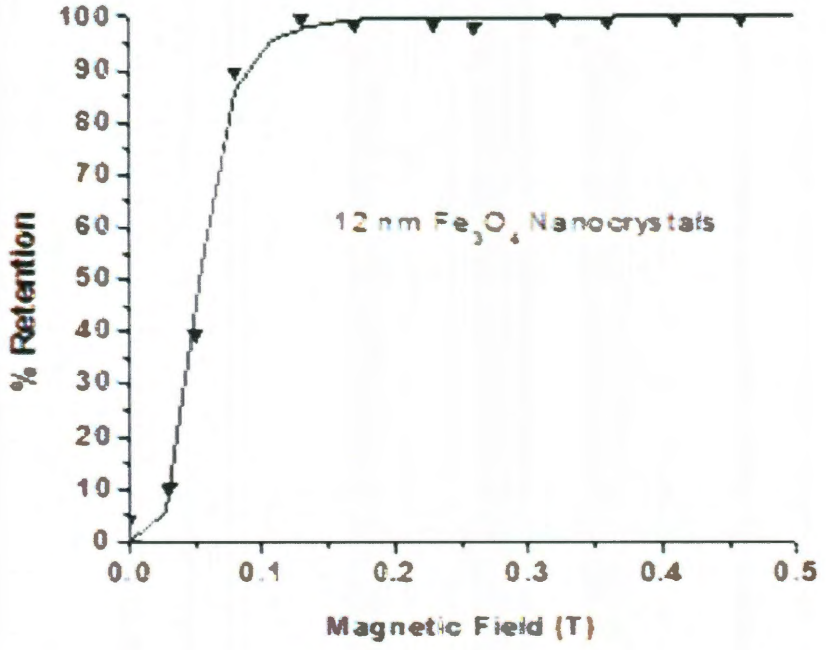

Figure 6.5 The magnetic field dependence of particle retention.
As the magnetic field increases, the retention of Fe_3O_4 nanocrystals increases.

Figure 6.4 shows the starting magnetite dispersions, effluents after passage through the column at various magnetic fields, and the solutions with the recovered nanoparticles after removal of the external magnetic field. Initially, the solutions are colored due to the presence of nanoparticles (first column). When they are exposed to the magnetic column, the nanoparticles adhere to the steel wool and the effluent at the bottom of the column is clear (second column). Finally, in some cases, the nanoparticles are recoverable once the magnetic field is removed and can be collected in a washing procedure (third column).

The recovery process is effective for small nanoparticles, but not for large ones. The agglomerated, commercial nanoparticles cannot be recovered from columns even under no field. There is irreversible sorption to the column packing materials. We speculate that their large magnetic moment provides a remanent magnetization at zero field. This would increase their interactions with the residual stray magnetic fields present in the column. In contrast, the smaller particles can be completely recovered at zero field.

To further understand the adsorption of arsenic on magnetite, comparison to the Langmuir isotherm was performed. All adsorption isotherm data were represented by the Langmuir isotherm equation:

Equation 6.1

$$q = \frac{b \times q^{max} \times C}{(1 + b \times C)}$$

where b is the sorption constant (L/μmol), q is the sorption density (μmol/g), C is a constant, and q^{max} is the maximum sorption density of the solid (μmol/g). Figure 6.6 shows an increase in the weight based arsenic(V) adsorption density with decreasing the particle size of magnetite. The surface-based arsenic(V) adsorption densities were very similar for 20 nm and 300 nm magnetite nanoparticles; however, the adsorption density for 12 nm magnetite

nanoparticles was significantly increased. These observations result from a higher surface area due to the smaller particle size, but may be influenced by the larger number of sites exposed for arsenic adsorption in the 12 nm magnetite as it was well-dispersed in solution, while the 20 nm and 300 nm magnetite nanoparticles were aggregated. A similar phenomenon was observed for arsenic(III).

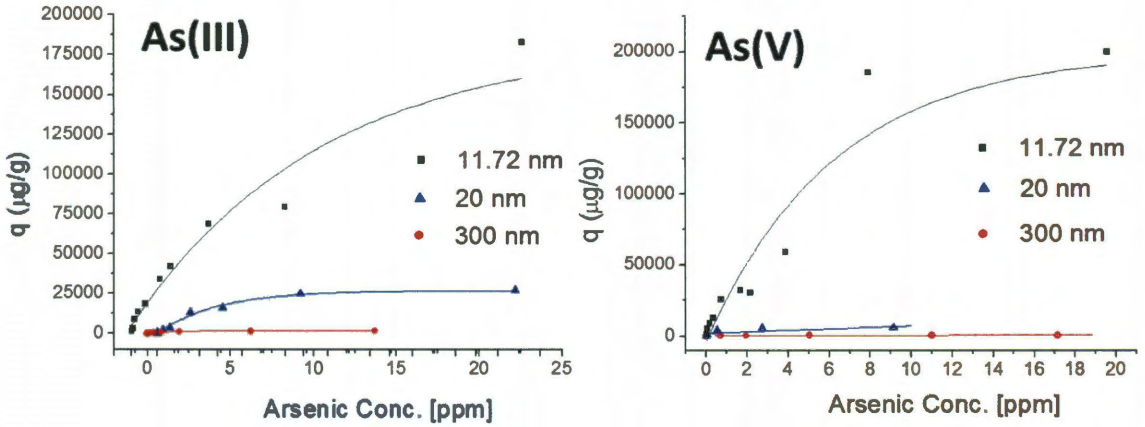

Figure 6.6 Plot of arsenic(III) and arsenic (V) adsorption on different magnetite nanoparticles (i.e., 12, 20, and 300 nm).
The solid lines are drawn using Langmuir isotherm equation. All adsorption data were plotted as equilibrium adsorbed arsenic versus equilibrium arsenic in solution. In this graph, q refers to the mass of arsenic adsorbed per mass of magnetite given in units of µg/g.

In the desorption studies, no loss of magnetite nanoparticles was assumed. The data in Figure 6.7 illustrate the irreversible desorption of both arsenic(III) and arsenic(V) from 20 nm magnetite nanoparticles. For example, approximately 1 % of the adsorbed arsenic(III) and arsenic(V) was desorbed at pH 6.1. Similar desorption hysteresis was observed at pH 4.8 and 8.0. The high adsorption capacity and strong desorption hysteresis suggest that magnetite nanoparticles can be useful in water treatment and solid waste disposal.

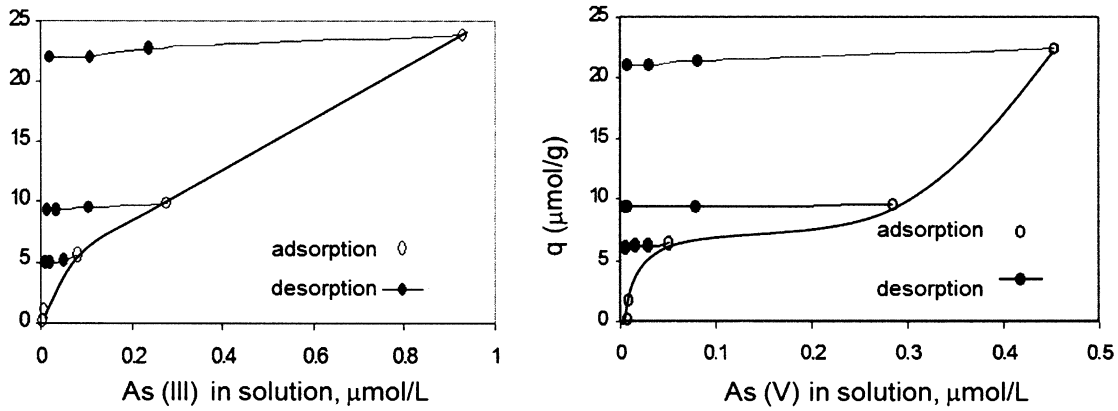

Figure 6.7 Adsorption and desorption of arsenic(III) and arsenic(V) to 20 nm Fe_3O_4 at pH 6.1.
All data were plotted as equilibrium adsorbed arsenic versus equilibrium arsenic in solution. In the desorption studies, no loss of magnetite nanoparticles was assumed.

In Table 6.1, arsenic removal efficiency was compared assuming a treatment of 3 L of 500 µg/L arsenic solution with 1 kg magnetite. The arsenic removal efficiency was calculated based on Freundlich isotherm equation:

Equation 6.2

$$q = K_F \times C^N$$

where K_F is the Freundlich constant, N is the Freundlich exponent, and C is the concentration of the dissociated arsenic, in the adsorption data over the range of 0 - 500 µg/L aqueous concentration. A decrease in residual arsenic concentrations and an increase in arsenic removal efficiency were observed with smaller magnetite nanoparticles. The 12 nm magnetite nanoparticles left residual arsenic concentrations of less than 10 µg/L and removed over 98 % of arsenic (III and V), while the 20 nm Fe_3O_4 removed more than 90 % and the 300 nm Fe_3O_4 was only able to remove at most 30 %. The high arsenic adsorption capacities found for the 12 nm magnetite nanoparticles agree well with previously published data that gives a full treatment of the sorption and desorption kinetics regarding the size dependence of magnetite nanoparticles.[27]

Table 6.1 The effect of Fe_3O_4 size on arsenic removal efficiency.

Particle Size (nm)	As(V) or As(III)	Initial As Concentration (μg/L)	Residual As Concentration (μg/L)	% Removal
12	As (III)	500	3.9	99.2
20	As (III)	500	46.3	90.9
300	As (III)	500	375.0	24.9
12	As (V)	500	7.8	98.4
20	As (V)	500	17.2	96.5
300	As (V)	500	356.4	29.2

Arsenic removal efficiency was compared assuming a treatment of 3 L of 500 μg/L arsenic solution with 1 kg magnetite. The arsenic removal efficiency was calculated using Freundlich isotherm equation, $q=K_F \cdot C^N$, in the adsorption data over the range of 0 – 500 μg/L aqueous concentrations.

Arsenic adsorption for a well-dispersed nanoscale magnetite was compared to aggregated nanoscale magnetite. The commercially available aggregated magnetite nanopowder (<50 nm) was added directly to the arsenate solutions at 0.4 g/L (Figure 6.8). The dispersed nanoscale magnetite was made from the same nanopowder but was made dispersable by sonication in 0.7 wt% Igepal CO-630 (Figure 6.9) and added to the arsenate solutions. TEM images of the aggregated (Figure 6.10) and dispersed (Figure 6.11) materials are shown. For this experiment, a variety of samples were prepared in triplicate. All experiments utilized 1.5 to 48 ppm arsenate solutions at pH~7 for 24 h while tumbling at 4 rpm. These experiments were compared with samples of arsenate in an aqueous Igepal CO-630 solution with the nanopowder (aggregated, not dispersed), and arsenate sonicated in an Igepal CO-630 solution before the addition of the nanopowder (aggregated, not dispersed) were compared as controls and can be seen as a comparison together on the arsenic adsorption isotherm in Figure 6.12.

Figure 6.8 Image of aggregated magnetite nanopowder in an aqueous solution

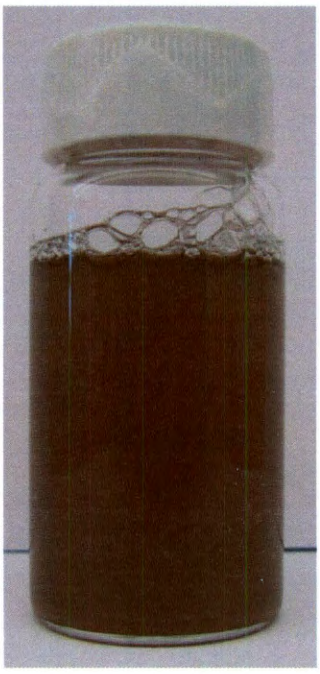

Figure 6.9 Image of dispersed magnetite nanopowder in an aqueous 0.07 wt% Igepal CO-630 solution

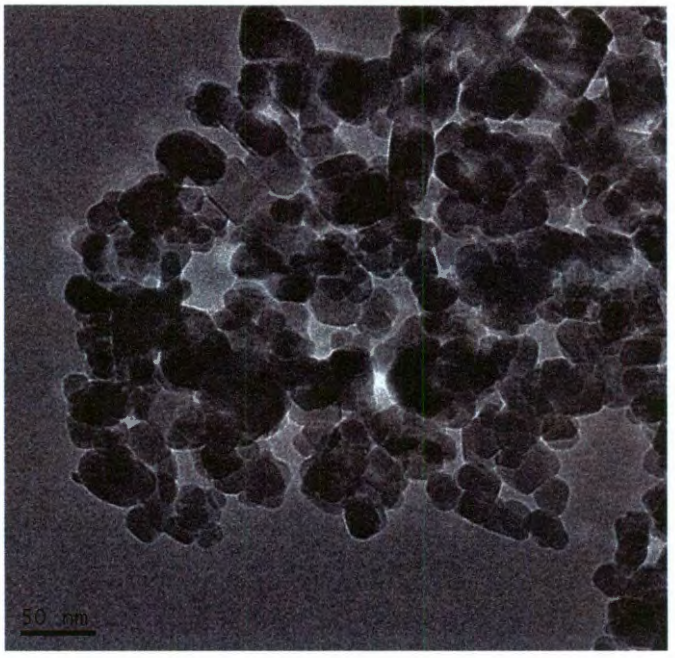

Figure 6.10 TEM image of aggregated magnetite nanopowder from an aqueous solution

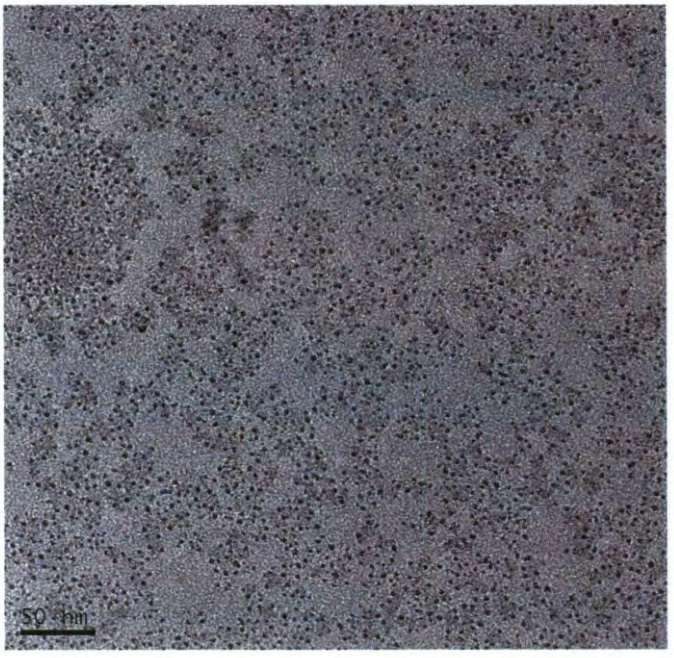

Figure 6.11 TEM image of dispersed magnetite nanopowder from an aqueous 0.07 wt% Igepal CO-630 solution

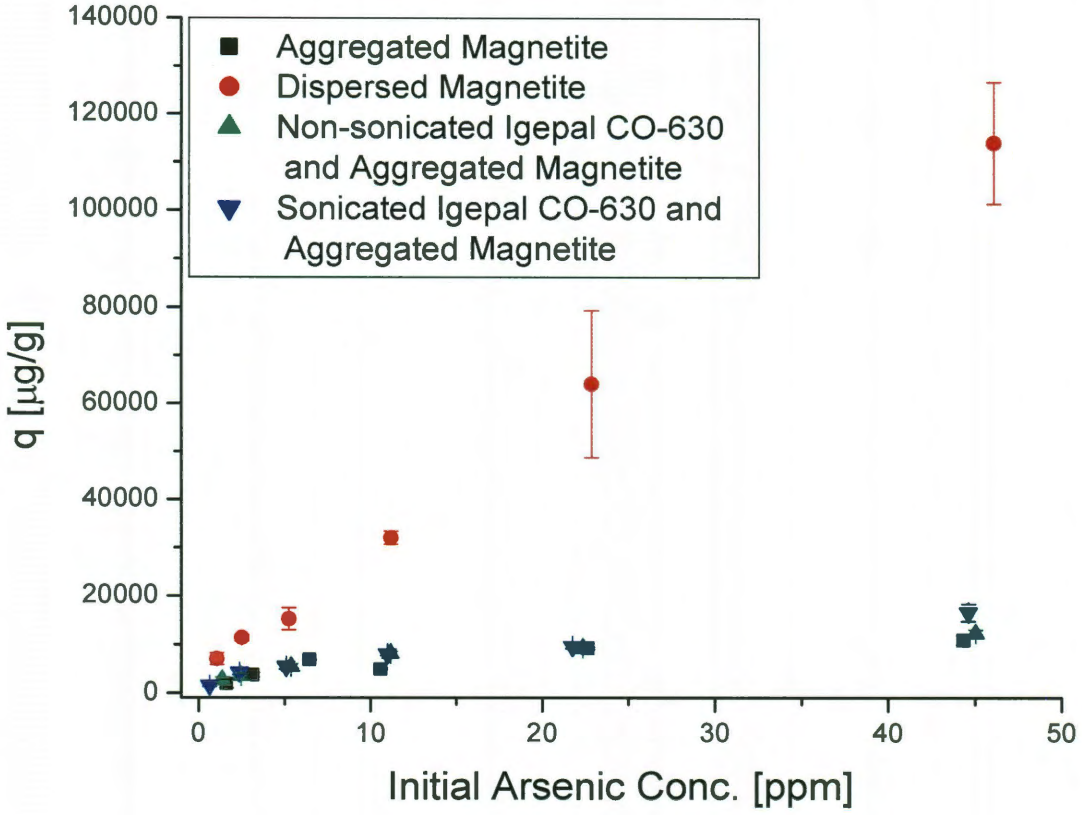

Figure 6.12 Comparison of arsenic adsorption isotherms from aggregated and well-dispersed magnetite Aggregated samples of 0.4 g/L nanopowder at pH~7 were compared to dispersed nanopowder. The first sample is aggregated nanopowder in the arsenate solutions. The second sample is identical except the nanopowder had been previously sonicated in 0.7 wt% Igepal CO-630 to disperse the aggregates. The third sample is a non-sonicated, aggregated nanopowder with arsenate in an aqueous Igepal CO-630 solution. The fourth sample is an arsenate sample sonicated in an Igepal CO-630 solution before the addition of the nanopowder. All adsorption data were plotted as equilibrium adsorbed arsenic versus equilibrium arsenic in solution. In this graph, q refers to the mass of arsenic adsorbed per mass of magnetite given in units of µg/g.

This data demonstrates that the well-dispersed nanomaterial adsorbs arsenic ~10 times better than aggregated equivalent material and the controls. This indicates that the arsenic adsorption is not primarily due to the surfactant or the presence of surfactant with iron oxides, but rather the dispersion itself increasing the available surface area of the nanoscale iron oxide. This is important because it demonstrates that access to the surface via dispersion is more important than the potential loss of available surface area due to the surface coverage of the surfactant. When the data in Figure 6.12 is compared to the data in

Figure 6.6, we see that although a dramatic improvement in the arsenic adsorption capacity is made when dispersing the commercial nanopowder, the improvement still does not achieve the levels of the laboratory synthesized magnetite. Even though both samples are well-dispersed, the laboratory synthesized magnetite is much smaller and, therefore, has a greater surface area per mass, allowing it to continue to outperform the commercial nanopowder.

6.4 Conclusion

Arsenic removal efficiency depends strongly on the size of magnetite sorbents. The small laboratory prepared magnetite was not only more efficient in the removal of arsenic, but also more easily recovered from the column of the magnetic separator than the commercial materials. This would be beneficial in a water treatment system because the arsenic contaminated magnetite could be flushed from the column permitting reuse of the separator system. It can also be concluded that dispersed materials will adsorb arsenic more efficiently than aggregated material even though both materials are in the presence of a surfactant. The well-dispersed nature of the laboratory synthesized material is a major reason why it outperforms the aggregated magnetite materials. However, it is not the only reason because the dispersed commercial magnetite still does not achieve the levels of the laboratory synthesized magnetite. Even though both samples are well-dispersed, the laboratory synthesized magnetite is smaller, allowing it to continue to outperform the commercial nanopowder. Interestingly, from the results of these experiments, it can be concluded that less expensive commercial nanopowders can be enhanced with surfactants to improve their sorption efficiencies and may prove to be an adequate adsorptive material for the remediation of arsenic from drinking water.

CHAPTER 7: nMAG FOR THE DETECTION AND REMEDIATION OF URANIUM IN ENVIRONMENTAL MATRICES

7.1 Introduction

Radionuclide quantification and remediation using sensitive, portable, and robust methods has been a longstanding challenge for society.[168-174] This fact has been underlined by recent events in Japan at the Fukushima-Daiichi reactor which illustrates the vital importance of this information to emergency response, risk mitigation, and human and environmental health.[175, 176] For many radionuclides, both detection and remediation efforts necessarily center on dilute samples as regulations set low exposure thresholds for radioactive species. As an example, the U.S. Environmental Protection Agency has established for uranium a maximum contaminant level of 30 parts per billion (ppb) in groundwater.[172] To detect whether these maximum contaminant levels are being met or to reduce the existing levels, we apply iron oxide nanocrystals as a platform for radionuclide collection, analysis, and remediation in lightly contaminated environmental media. While our focus is on uranium, the chemistry of the actinides is similar and our strategy may be appropriate for other types of radionuclides.[177-179]

Methods for uranium detection include both mass and optical emission spectrometry as well as radiation analysis. Thermal ionization mass spectrometry, inductively coupled plasma optical emission spectroscopy (ICP-OES), and inductively coupled plasma mass spectrometry (ICP-MS) are powerful analytical tools that can detect the presence of uranium isotopes from the part per million (ppm) to part per trillion (ppt) level.[180] While ultra-

sensitive, these approaches require a sophisticated laboratory infrastructure which limits their ability to provide rapid data in low infrastructure settings. In contrast, handheld scintillation counters can perform highly sensitive radiation measurements associated with uranium decay and emission of α-particles which are counted individually. However, they are not always practical for detecting low levels (< ppm) of uranium in highly relevant samples such as water, soils, and biological fluids. Scintillation counters can be effectively used to measure the presence of uranium because the dominant isotope, U-238 (99.3 % natural abundance), is an α-particle emitter, decaying through a 14-step decay series arriving at stable Pb-206 (Figure 7.1).[60, 181, 182] α-decay occurs when $^{4}_{2}He$ separates from the nucleus (Figure 7.2).[183] However, it is not always possible to detect the emitted α-particles because they are strongly absorbed by most solids and liquids. Just 40 microns of water can effectively block 99.99% of an α-particle source.[184, 185]

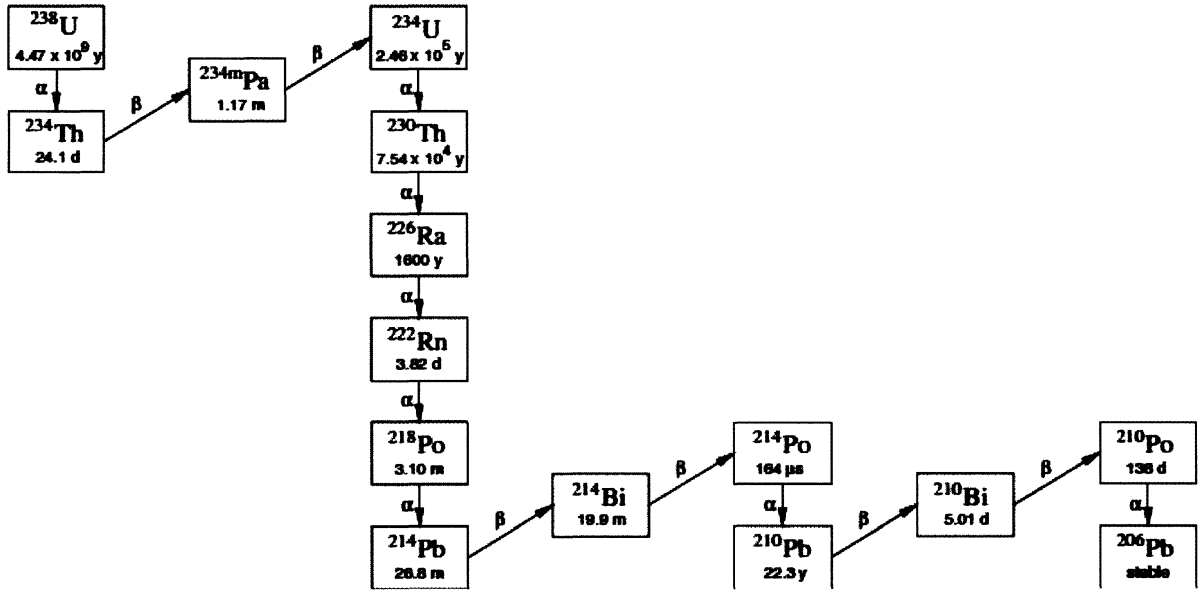

Figure 7.1 U-238 decay chain
14-step decay series of U-238 ending in Pb-206. Half-lives for each step is given along with the primary decay product. (Figure reprinted with permission[182])

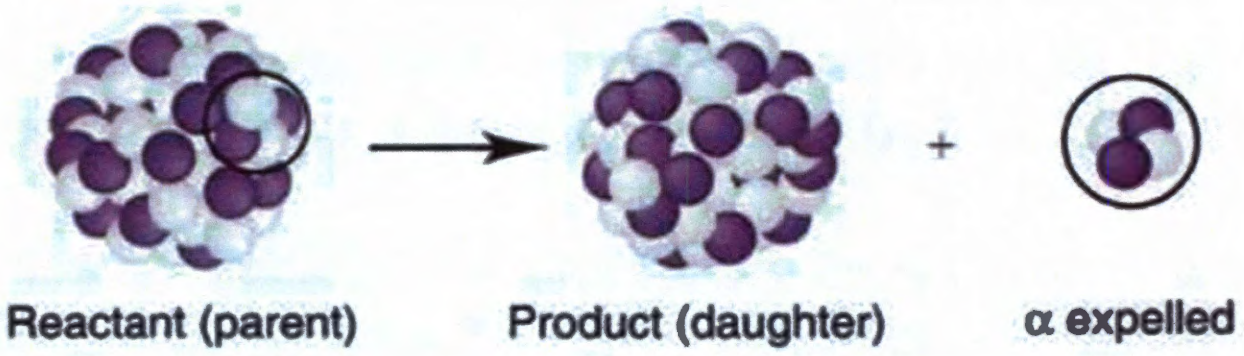

Figure 7.2 Radioactive α-decay reaction
This figure illustrates the expulsion of an α-particle from the nucleus of the reactant (parent) radioactive atom. (Figure adapted with permission[183])

Because of this interference, α-particle quantification either requires very long counting times or sample modifications that ensure α-particles are emitted (and detected) only at a sample's surface. This issue was highlighted by the work of Goldstein and Stirling who generated, via electrochemical methods, a uniform "infinitely thin" film of uranium for solid-state α-particle detection.[180] Similarly, thin and porous polymers can be engineered to bind uranium, and in one example radionuclides sorbed from 10 part per trillion solutions onto these substrates were detected using scintillation counters.[186, 187] Both approaches require mass transfer of uranium from dilute solutions to fixed surfaces, either an electrode or polymer interface, and would be difficult to apply to large sample volumes of heterogeneous, environmental media.

The approach described here uses nanocrystalline iron oxides to bind and separate uranium from solution. It has been demonstrated that iron oxides have a high affinity for the adsorption of uranium and can form inner sphere bidentate-mononuclear complexes (Figure 7.3).[34] The use of engineered materials for uranium concentration has been explored in the context of water remediation as well as geochemistry; natural minerals, metal oxides, and polymers can bind, and in some cases, concentrate uranium species from water.[73, 74, 188-191]

Crystalline iron oxides and zero-valent iron are effective adsorbents for uranium, in particular the uranyl ion (UO_2^{2+}) formed when uranium oxides are acidified under oxic conditions.[73, 74, 190, 192] In this work, the capacity for the iron oxide to adsorb uranium, measured as the maximum weight percent of uranium sorbed to the material, was maximized through the use of nanoscale particles with high surface areas. These nanocrystalline iron oxides also demonstrate significant susceptibility to externally applied magnetic fields, which, for near neutral solutions, can be utilized for material separation and concentration as opposed to physical filtration.[18] Finally, while the uranium content in the concentrated nanoparticle residues could be measured after acid digestion using ICP-MS/ICP-OES analysis, the narrow particle size distributions led to the generation of sub-micron films that minimized α-particle absorption by the iron oxide. This feature facilitated rapid detection of microgram quantities of uranium recovered from dilute environmental samples.

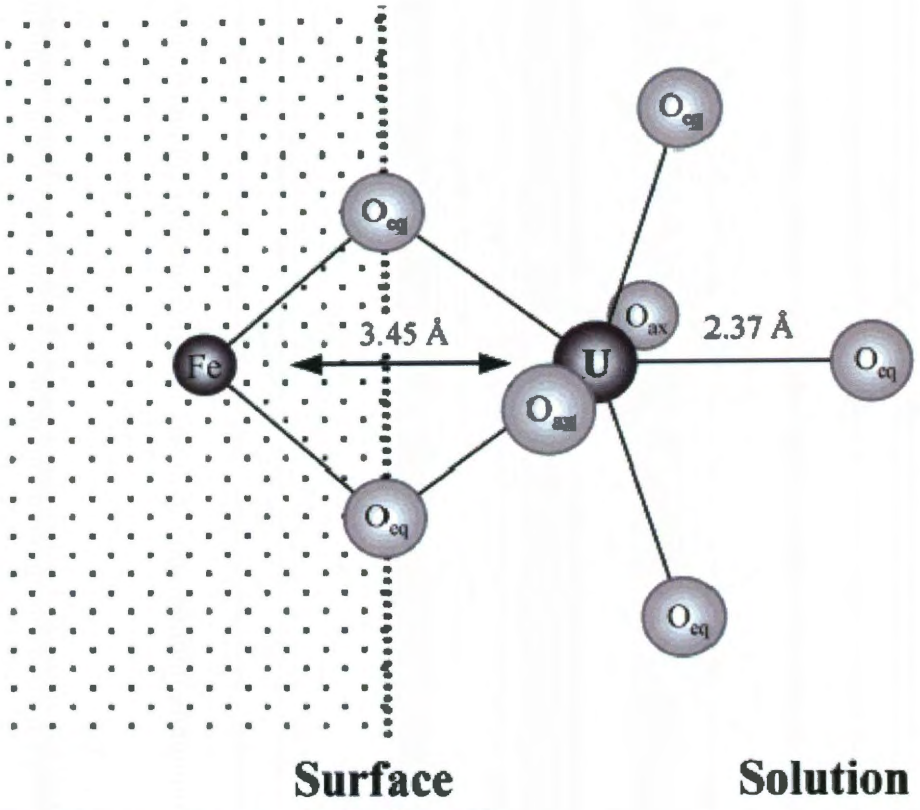

Figure 7.3 Inner sphere uranium complex with iron oxide
Inner sphere bidentate-mononuclear complex of uranium with goethite based on EXAFS spectroscopy. (Figure reprinted with permission[34])

7.2 Experimental Methods

7.2.1 Instrumentation

Quantitative determination of nanoparticle concentrations via iron content and of uranium concentrations was found by using a PerkinElmer Optima 4300 DV Inductively Coupled Plasma-Optical Emission Spectrometer (ICP-OES) or a PerkinElmer Optima Elan 9000 Inductively Coupled Plasma-Mass Spectrometer (ICP-MS). Radiation from the uranium was detected by a Ludlum model 43-1-1 scintillator α-particle detector. Low speed centrifugation for purification was performed with a Fisher Scientific Marathon 22K. Probe sonication for phase transfer was performed with a Hielscher UP100H Ultrasonic Processor.

The images of the nanoscale iron oxides were captured by a 2100 JEOL Field Emission Gun Transmission Electron Microscope (FEG-TEM) operated at 200 kV and sizes were determined using Image Pro software. A Gatan Imaging Filter (GIF) for elemental mapping incorporated with the FEG-TEM was used to determine if uranium is bound to the nMAG system. Also incorporated on the FEG-TEM was an Oxford Energy Dispersive Spectrometer (EDS) backscatter detector, used for elemental analysis. Small-Angle X-ray Scattering (SAXS) was performed by a Rigaku SmartLab X-ray Diffractometer. Thin film morphology was analyzed with an FEI Quanta 400 ESEM FEG Scanning Electron Microscope (SEM). Samples were sputter coated with a layer of gold on a CRC-150 Sputter Coater before SEM analysis.

7.2.2 Materials

The materials required for the nMAG synthesis are FeO(OH) (Iron(III) Oxide, hydrated; catalyst grade, 30-50 mesh; cat. #371254), oleic acid (90% technical grade), and 1-octadecene (90% technical grade) from Sigma-Aldrich. Hexanes (certified ACS grade) were purchased from Fisher Scientific. Commercially available nanoscale magnetite (Sigma-Aldrich, Iron (II,III) oxide, nanopowder, <50 nm, 98+ %) was used as a comparative material to the laboratory synthesized nMAG. Sand (sea, washed) was purchased from Fisher. The uranium used in these experiments was from an aqueous uranyl nitrate solution. The uranium standards used for the ICP-OES and ICP-MS calibration stock solution (1004 ppm U in 1.2 wt% HNO_3) was purchased from Sigma-Aldrich.

7.2.3 Synthesis and Preparation of Magnetite Nanocrystals

Nanoscale iron oxide (Fe_3O_4) was synthesized via thermal decomposition by adding 20.02 g FeO(OH) to a mixture of 1 L 1-octadecene and 255 g oleic acid. The mixture was heated to 320 °C with stirring for 2 hours to produce the magnetite nanocrystals, as described by Yu *et al.*[22] The nanocrystalline magnetite was then precipitated with an excess of ethanol. The slurry was then centrifuged at 4,500 rpm, allowing for the solvent to be decanted. The iron oxide nanocrystals were then redispersed in a minimal amount of hexanes. This flocculation step was repeated two more times to recover pure nanocrystals without any residual molecular by-products.

Water soluble iron oxide nanocrystals were then prepared by adding 0.03 mL oleic acid to 1 mL of the nanoparticle stock suspension and then mixed with 10 mL of Millipore® water. The phase separated mixture was probe sonicated for 5 min and was centrifuged at 4,500 rpm for 15 min before passing through a 0.2 μm syringe filter (Whatman, GD/X, nylon). The filtered product was a clear suspension of magnetite nanoparticles coated with a bilayer of oleic acid dispersed in water.[24]

7.2.4 nMAG Characterization

Nanoparticle sizes and shapes were verified by FEG-TEM and SAXS. Three detector methods in the FEG-TEM were used to obtain data: CCD, GIF and EDS. The CCD camera was used for high resolution micrographs, a GIF detector was used for iron and uranium energy filtered images, and an Oxford EDS backscatter detector was used for elemental analysis. TEM samples were prepared on ultrathin carbon coated copper grids (Ted Pella). For SAXS analysis, 15 μL of sample (~0.5 g/L) was taken in a quartz capillary tube and

analyzed for two hours. The resulting scan data were analyzed using Nanosolver software, which takes in the densities of water, iron oxide and the oleic acid as parameters and fits the system in accordance with a core-shell model to compute the size and size distribution of the nanoparticles.

7.2.5 Uranium Analysis

Uranium concentration was analyzed by an ICP-OES or ICP-MS. Uranium calibration standards were quantitatively diluted in 1 % HNO_3 from a uranium calibration stock solution. Based on uranium decay and the subsequent emission of α-particles (0.691 pCi/μg for natural abundance uranium), uranium was detected and quantified via α-particle detection.[180] α-particles were measured from uranium solutions dried onto a flat filter disc (0.02 μm Anodisc, 47 mm diameter, Whatman) at a parallel distance of 10 mm. Upon sorption, uranium-loaded nanoparticles were similarly analyzed via α-particle detection. Films of uranium-loaded particles were prepared on a 0.02 μm alumina filter membrane via gentle vacuum filtration, which allowed for uranium-loaded particle deposition and solution separation. Films were individually dried overnight under vacuum, whereby total uranium-loaded particle mass was calculated by subtracting the filter mass from the total mass, yielding typically 0.40 mg of material. Film measurements (α-particle counts) were taken as one minute averages for 150 minutes per sample. Experiments were also performed in order to determine how much magnetite material could be used before α-particle self-absorption effects are observed. This was performed by sequentially adding more and more uranium coated magnetite to a filter and measuring the α-particle counts.

7.2.6 Uranium Sorption Behavior (Isotherms)

In methods similar to those previously described,[18, 27, 33] uranyl sorption isotherms were characterized for the two magnetite systems: commercially available nanoscale magnetite and the oleic acid stabilized iron oxide nanocrystals described earlier. The sorption behavior of the commercial and laboratory prepared iron oxide nanomaterials were determined by adding them to aqueous solutions at various uranium concentrations at pH 5, 7, and 9 and allowed to adsorb for 24 hours. The solution volumes were typically 5 mL, containing 0.01 to 1 g/L iron oxide, and the uranium concentrations in these dilute samples ranged from 1.53 to 41.2 ppm. Upon equilibrium under oxic conditions, the suspensions were filtered and analyzed by ICP-OES to determine the amount of uranium remaining in solution. The sorption capacity, q, was then determined by dividing the amount of uranium sorbed onto the particles by the mass of the particles. Kinetics experiments were performed beforehand to determine the necessary time to reach an equilibrium state for particle sorption isotherms; while most of the sorption occurred within one hour, to obtain the most accurate data, the system was allowed to equilibrate for one day. All experiments were performed in triplicate.

7.2.7 Soil Preparation and Extractions

A 9.35 g/L uranyl stock solution was prepared with concentrated uranyl nitrate at pH 3. Sea sand was mixed with diluted uranyl stock solutions. The sand mixture was allowed to completely dry under vacuum. The final uranium concentration ranged from 1 to 134 ppm. The dried sand mixture was then washed with various solutions to determine their extraction

efficiencies. Many of these extraction solutions for the removal of uranium were tested and can be seen in Figure 7.4. These extraction solutions provided a wide range of efficiencies for the removal of uranyl. 1 % HNO_3 was chosen for not only its high efficiency for uranyl extraction but also because it does not later interfere with the adsorption process. It was determined that a 1% HNO_3 solution approached 100 % uranyl extraction efficiency. This extraction solution was used thereafter for all following experiments. After extraction, the acidic solutions were adjusted to pH ≈ 5 with dilute NaOH solution before further process steps.

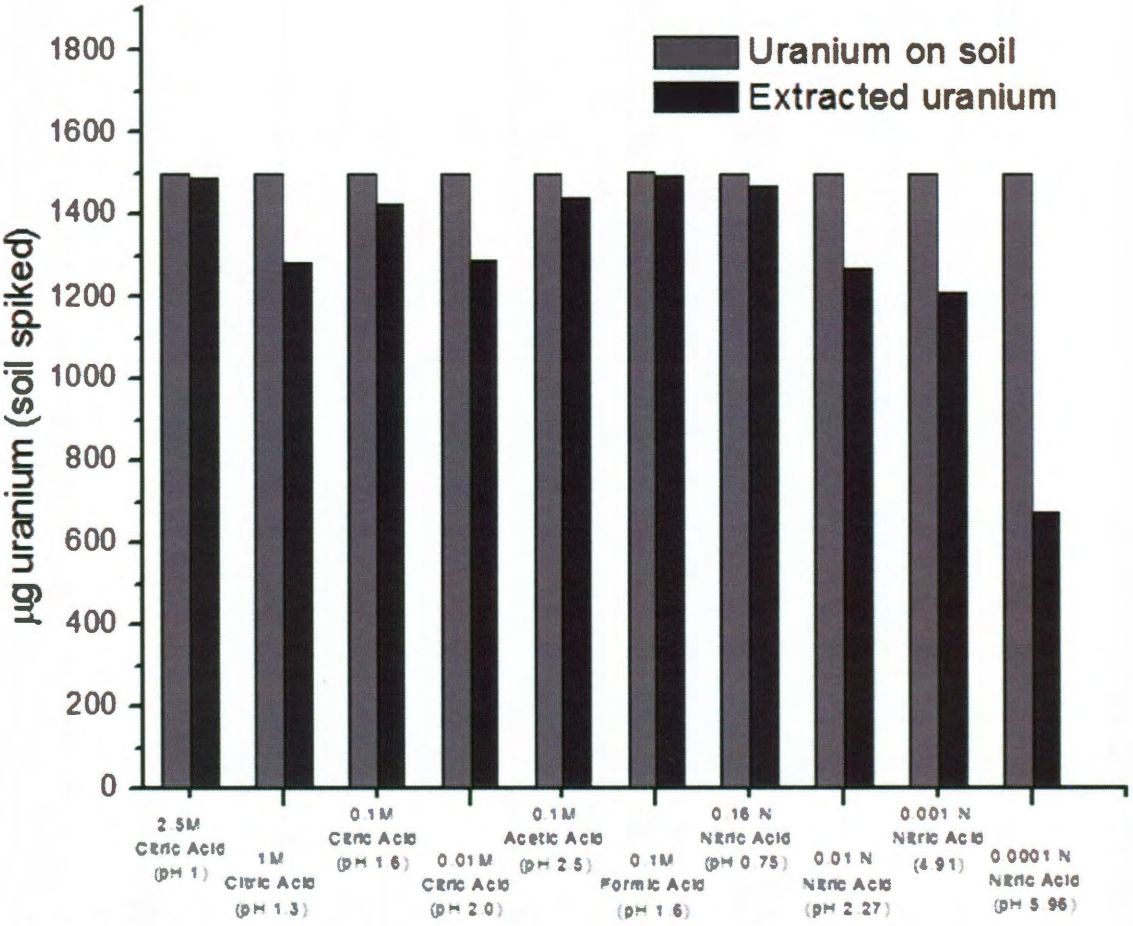

Figure 7.4 Comparison of uranyl extraction solutions
This plot compares various uranyl extraction solutions based on the known initial uranium concentration on the sand versus the total uranium extracted. High extraction efficiencies are observed for 2.5 M citric acid, 0.1 M acetic acid, 0.1 M formic acid, and 0.16 N nitric acid. A slightly higher 1 % (0.23 N) nitric acid was chosen over the organic acids in order to avoid interferences in uranyl adsorption to magnetite.

7.2.8 Deposition Characterization

It is critical to form a thin and uniform film for optimal α-particle counting to prevent α-particle self-absorption. When using isolated nanoparticles, a 10 mL suspension of particles (~0.40 mg total mass), at varying degrees of sorbed uranyl concentrations, was slowly vacuum filtered through a weighed, 0.02 μm filter membrane (Anodisc, 47 mm diameter, Whatman) to yield a thin and uniform film. Effluent was collected and measured for uranium concentration via ICP-MS or ICP-OES. Membranes with a thin film were then dried under vacuum and reweighed. The measured difference between the final and the starting weights were taken as the total mass of uranium-iron oxide nanoparticle complex. Film morphology was characterized by SEM, after sputter coating the samples with ca. 5 nm Au. The same process was used to make a film by commercial magnetite powder. The entire extraction, adsorption, deposition, and analysis process can be seen in Figure 7.5.

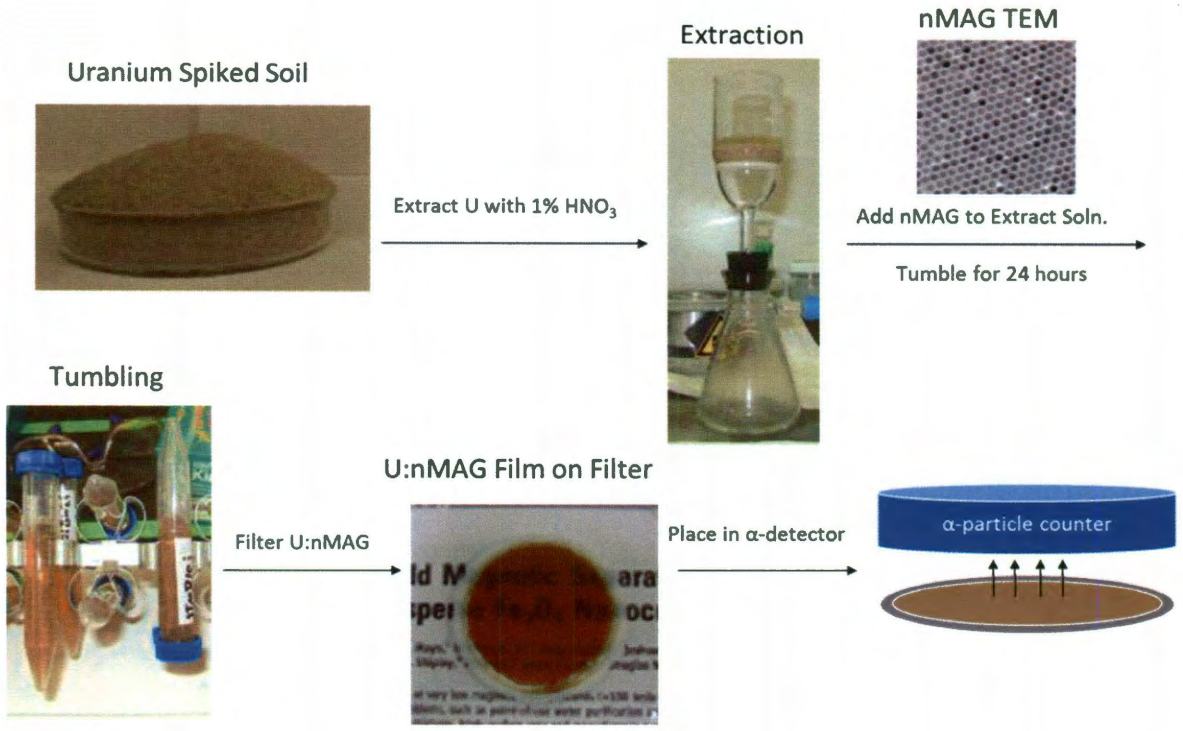

Figure 7.5 Process schematic for the extraction, adsorption, deposition, and analysis of uranium using magnetite
The overall process that is presented here involves the extraction of the uranyl nitrate with 1 % HNO_3 and readjustment of the pH to 5 by addition of NaOH. The nanoscale magnetite is then added to the uranyl solution for 24 hrs to insure complete adsorption. The uranium coated magnetite is then laid down as a thin film on the alumina filter, dried, and placed under an α-particle detector for analysis.

7.3 Results and Discussion

Two distinct types of iron oxide nanomaterials were compared in these studies. The first was a commercially available nanoscale (primary particles 10-50 nm diameter) magnetite powder, which is aggregated when dispersed in water (Figure 7.6a). The second was a nanocrystalline iron oxide formed via thermal decomposition of iron carboxylates. This material was phase transferred into water with oleic acid.[24] Transmission electron microscope (TEM) analyses showed these materials to be nearly uniform in particle diameter (10.8±0.6 nm) (Figure 7.6d). SAXS of the aqueous solution confirmed the measured core

diameters from TEM and identified the primary species as single iron oxide cores coated with an oleic acid bilayer (11.95±0.8 nm) (Figure 7.7) Commercial magnetite could not be analyzed via SAXS in water due to extensive aggregation.

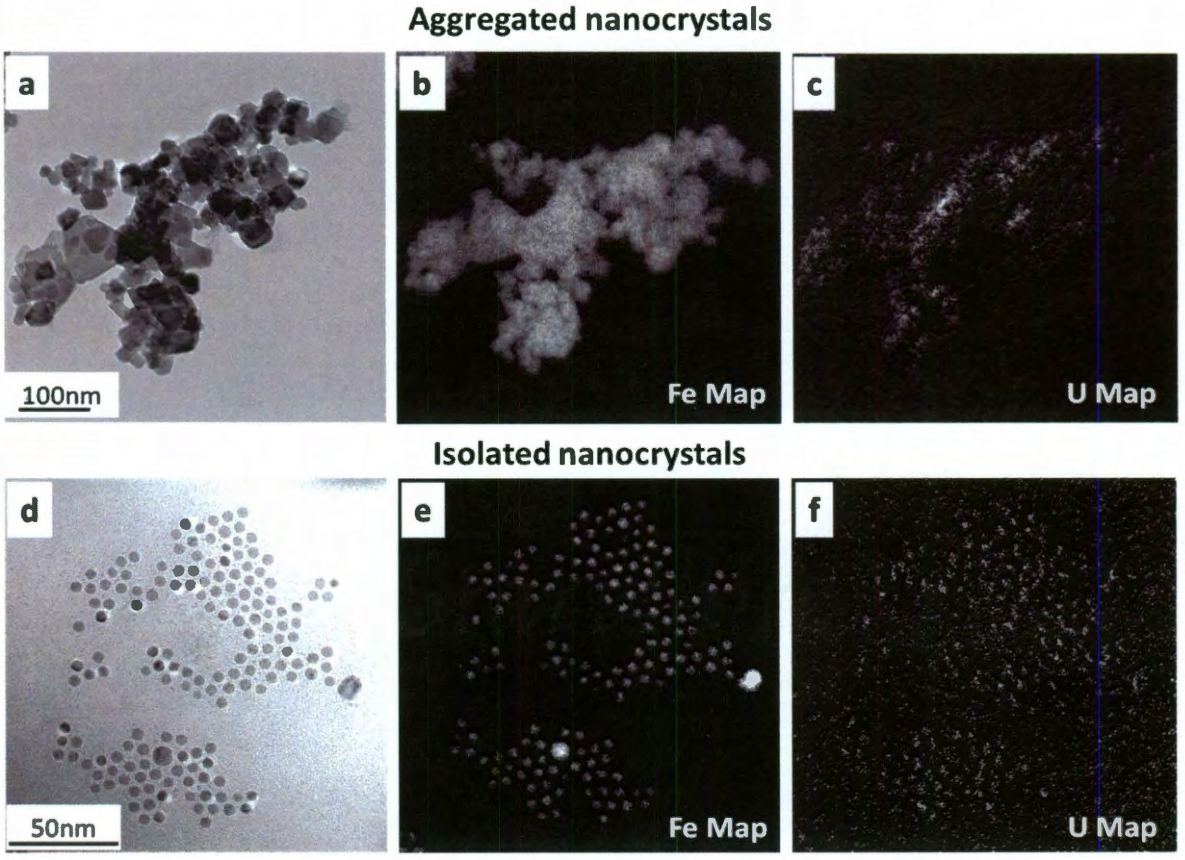

Figure 7.6 Images of iron oxide nanocrystals after uranium exposure
(a) FEG-TEM image of commercial nanoscale magnetite; (b) Fe mapping using GIF imaging on commercial nanoscale magnetite; (c) U mapping using GIF imaging on commercial nanoscale magnetite; (d) FEG-TEM image of oleic acid stabilized nanocrystals; (e) Fe mapping using GIF imaging on oleic acid stabilized nanocrystals; (f) U mapping using GIF imaging on oleic acid stabilized nanocrystals.

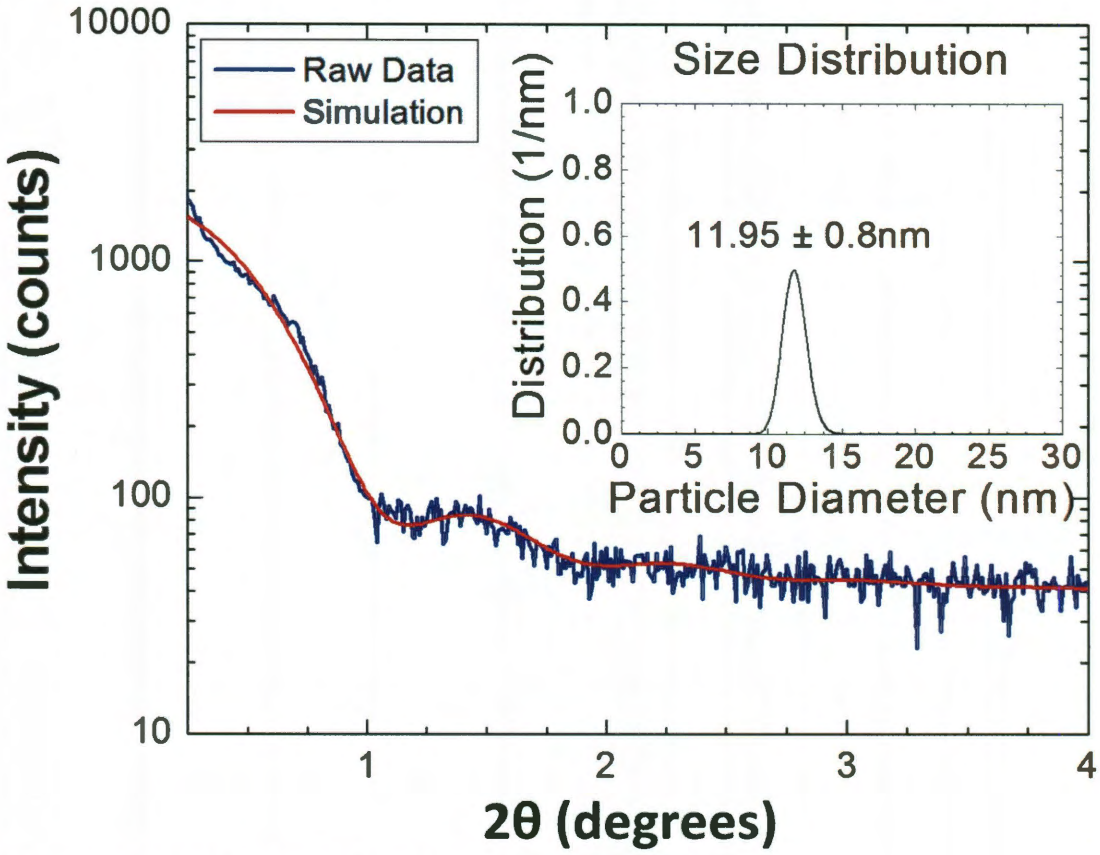

Figure 7.7 SAXS data for the oleic acid stabilized magnetite sample

While both nanocrystalline iron oxides were able to adsorb uranium from solutions, the non-aggregated materials were more effective and could in some experiments concentrate uranium by a factor of more than 50,000. Maximum sorption (pH 5) values at room temperature with 24 hour equilibration time for both samples were 428 mg/g (30 wt%) for oleic acid stabilized nanocrystals and 40 mg/g (3.8 wt%) for the commercially available magnetite powder. To further understand the adsorption of uranium on magnetite, a comparison to the Langmuir isotherm was performed. All adsorption isotherm data were represented by the Langmuir isotherm equation:

Equation 7.1

$$q = \frac{b \times q^{max} \times C}{(1 + b \times C)}$$

where b is the sorption constant (L/μg), q is the sorption density (μg/g), C is a constant, and q^{max} is the maximum sorption density of the solid (μg/g). Such large concentration factors are reflected by the high uranyl sorption capacities of iron oxides. These sorption properties are presented for both the aggregated and non-aggregated materials in Figure 7.8. Linear range isotherm data for these materials were used to determine the partitioning coefficient K_d, defined as a ratio of bound to dissolved uranium in a closed, equilibrated system, and given as:

Equation 7.2

$$K_d = \frac{V}{m} \times \frac{[U_{ads}]}{[U_{dis}]}$$

where V is the volume, m is the mass of sorbent, and $[U_{ads}]$ and $[U_{dis}]$ are the concentrations of adsorbed and dissociated uranium, respectively.[193] Oleic acid stabilized nanocrystals have a calculated K_d of $10^{4.70}$ while the K_d for the aggregated particles was $10^{3.26}$. An EDS detector coupled with an FEG-TEM detected uranium and iron in the magnetite samples with much higher uranium levels in the laboratory synthesized sample, indicating an improved uranium concentrating ability (Figure 7.9). A GIF applied to FEG-TEM images revealed electron energy loss profiles after uranium sorption (Figure 7.6) that matched to both uranium and iron. This data supports a direct contact/sorption model as suggested by the literature on uranium interactions with iron oxide minerals.[49, 193]

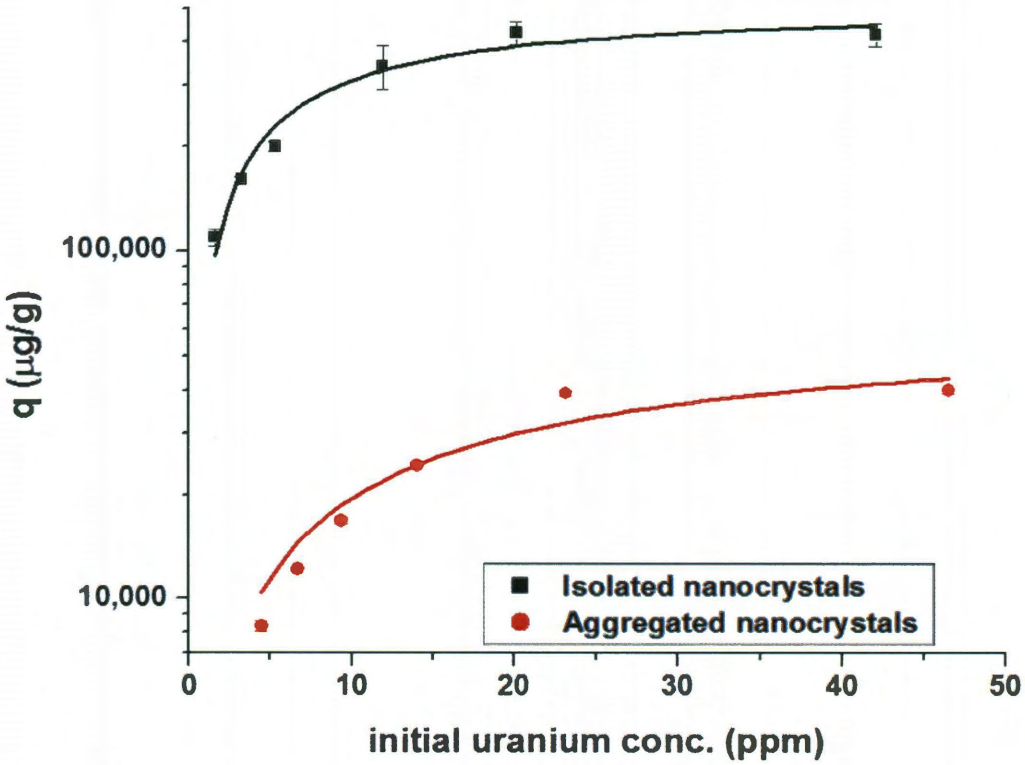

Figure 7.8 The sorption isotherms for uranyl and iron oxide nanocrystals
Oleic acid stabilized nanocrystals have a maximum uranyl sorption capacity near 30 wt% compared to 3.8 wt% for commercially available nanoscale magnetite (pH 5, room temp, 24 hr equilibration). In some cases, the error bars are not larger than the symbol height. For these experiments the concentration factors ranged from 67,200 in the most dilute case for non-aggregated materials down to 9,580 for the most concentrated uranium sample.

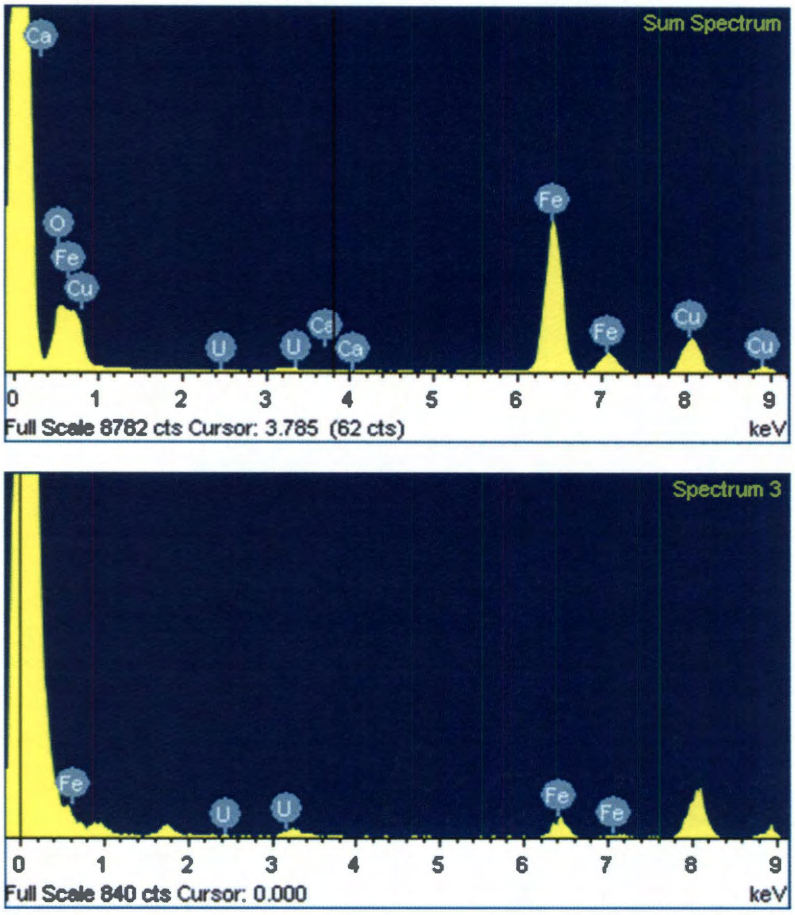

A

Element	Weight%	Atomic%
Fe K	94.74	98.72
U L	5.26	1.28
Totals	100.00	

B

Element	Weight%	Atomic%
Fe K	47.81	79.61
U L	52.19	20.39
Totals	100.00	

Figure 7.9 EDS data for uranium coated magnetite
The EDS data shows that uranium and iron are present in both (A) the commercial magnetite and (B) the laboratory synthesized magnetite. This data also demonstrates that the laboratory synthesized magnetite has a higher uranium/iron ratio.

Data of the type shown in Figure 7.8 was used to calculate a typical factor by which uranium could be concentrated onto the iron oxide nanoparticles.[194] For example, in one experiment uranium in dilute solution (1.53 ppm) was exposed to iron oxide particles; analysis of the particles after the adsorption experiment revealed the 500 μg sample contained 10.2 w/w% uranium corresponding to a concentration factor of 67,200. Experimental factors such as equilibration time, uranium starting concentration and mass of added iron oxide can all affect the concentration factor to some extent. The lowest observed in Figure 7.8 was 9,580 corresponding to a starting solution concentration of 30 ppm.

Generally the concentration factor decreased with increasing concentrations of uranium as detailed in the figure caption. Also notable is the observation that the aggregated particles had concentration factors from 800 to 1,900. These lower values as compared to the isolated materials are due, in part, to their lower available surface areas.

The resulting nanocrystal-uranium complexes were separated from the sample matrix either through the application of an external magnetic field or through the use of a physical filter. Both methods provided yields of over 90% as measured by the solution iron concentration before and after. However, in some cases the acidification of the samples to dissolve uranium oxides or expel carbonates precluded the direct introduction of iron oxide into the matrix; separation and pH adjustment was performed on the supernatants in those instances before the addition of iron oxides. Conventional analytical tools such as ICP-OES or ICP-MS were applied to quantify uranium in supernatants and recovered solids alike. Such data was the basis for analyzing the uranium sorption of these materials as shown in Figure 7.8. Interestingly, during the separation processes for non-aggregated nanocrystals, we observed the formation of dense, visually uniform films. SEM images of these residues showed they were dense on the nanometer scale, with a highly even and smooth surface. In contrast, the commercial materials formed loose powders that were thick and heterogeneous (Figure 7.10). Highly aggregated nanocrystals in solution do not pack efficiently when concentrated into residues; in contrast, isolated, and uniform nanocrystals are the ideal starting point for forming dense, homogeneous arrays of particles.[195]

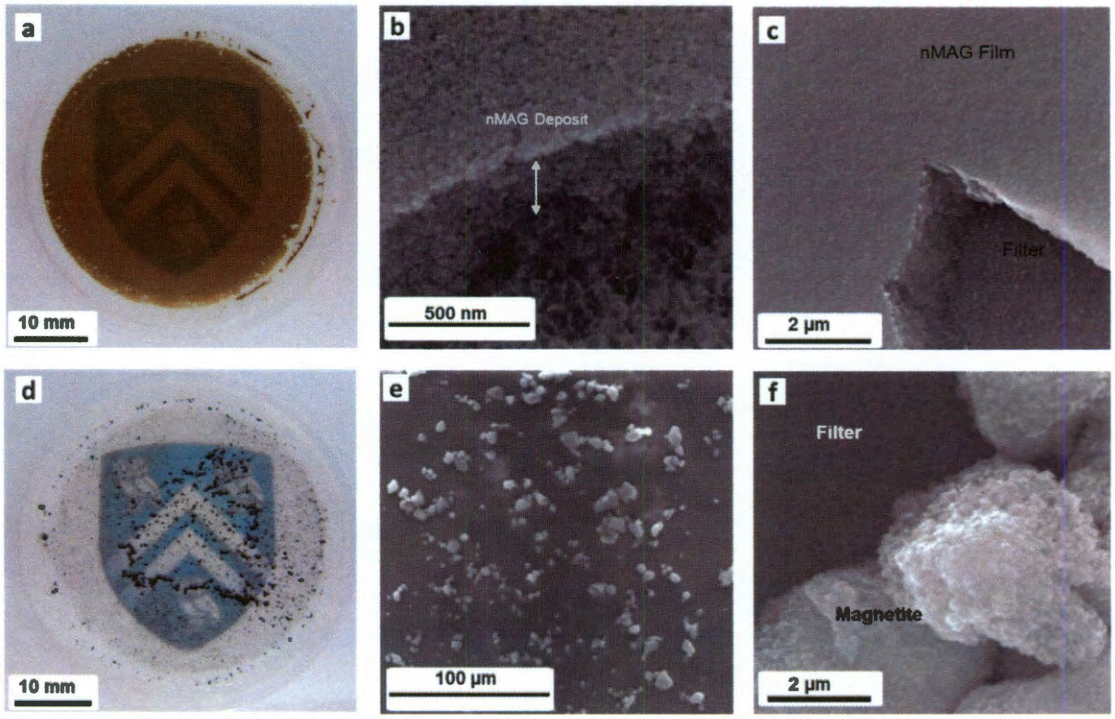

Figure 7.10 Morphology of concentrated deposits of uranium-loaded nanocrystals
(a) Deposition of isolated nanoparticles, and (b,c) SEM analysis of isolated nanoparticles with sorbed uranium as residues for α-particle analysis. For surface stabilized materials, the film thickness is estimated at 800 nm (0.40 mg material). (d) Commercial magnetite deposition, and (e,f) SEM analysis of aggregated nanoscale magnetite with sorbed uranium as prepared residues for α-particle analysis (10 mg material). The particles aggregate and do not form a uniform film.

The thin film geometry shown in Figure 7.10 is ideal for highly sensitive solid state scintillation counting of uranium-containing materials. We found that microgram quantities of sorbed uranium in these films could be quantified within hours (Figure 7.11). Residues loaded with increasing amounts of uranium were examined via α-counting, and the measurements compared to the mass of uranium in the residue as measured by ICP-OES. Our detection limit for uranium in these films, for a 2.5 hour sampling time, was 8.5 µg. The counts measured increased linearly with the amount of uranium adsorbed onto the nanocrystals, which enabled a reliable calibration and the quantification of total uranium in the concentrated sample. This detection method would be the most sensitive for iron oxide nanocrystals nearly saturated with uranium (e.g. at more than 10 w/w% loading). However,

even when residues are only partially loaded, as they were in some of these experiments, it is possible to detect microgram quantities of uranium. For comparison, the counts measured in the aggregated nanocrystal sample are shown on the same scale. Because this sorbent forms thicker, heterogeneous deposits, α-particles are more often absorbed and, as a result, scintillation counting is only feasible for residues containing milligram quantities of uranium. The data in Figure 7.12 demonstrates that approximately 35 mg of uranium coated magnetite can be used before α-particle self-absorption effects are observed for the commercial magnetite system.

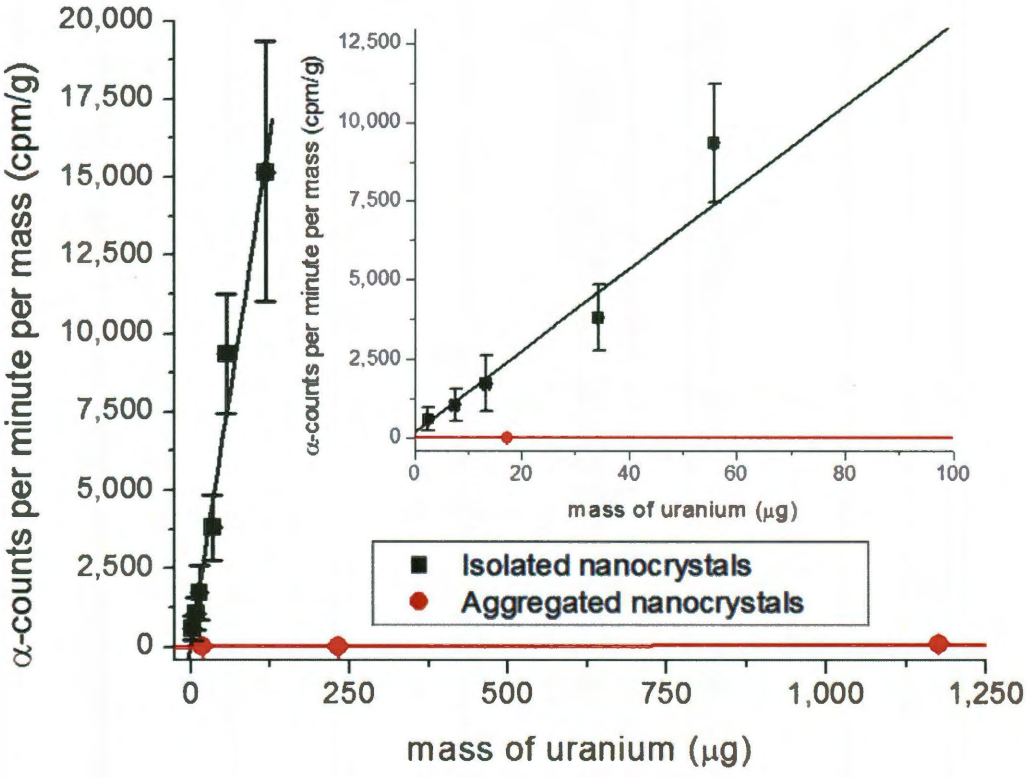

Figure 7.11 Solid state scintillation counting of uranium-loaded nanocrystal films
α-particle counting (counts per minute) as a function of uranium loading (sorption) onto the nanoscale iron oxide particles (normalized to the mass of sample). Total sample mass for these experiments was roughly 0.40 mg for the oleic acid stabilized nanocrystals and 10 mg for the commercial material. The isolated nanocrystals are clearly a more sensitive uranium detection platform, and for 400 μg of recovered iron oxide particles it is possible to detect as little as 8.5 μg of uranium.[196]

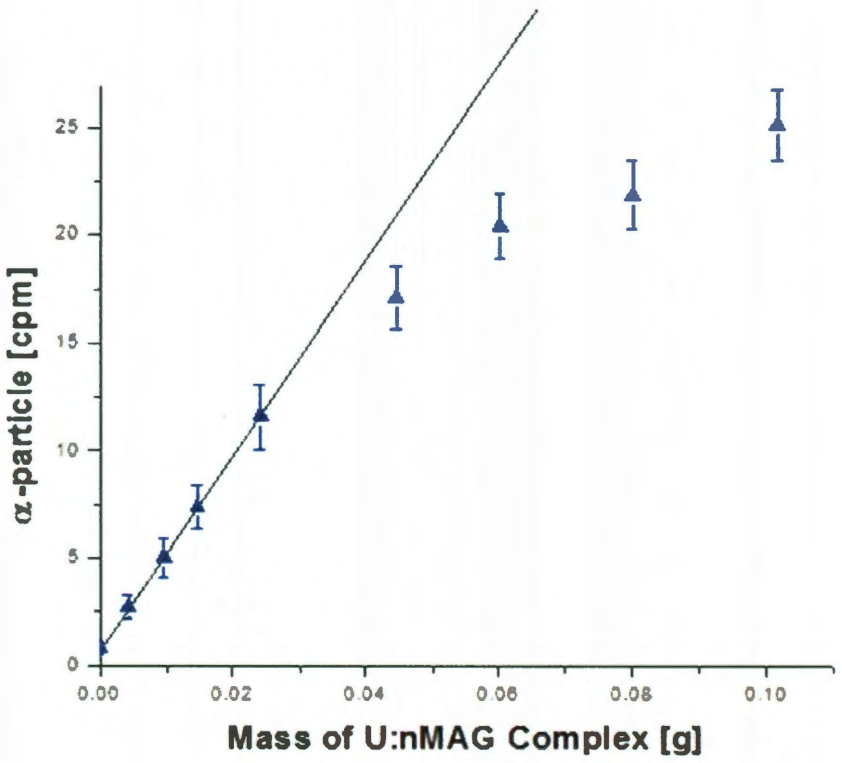

Figure 7.12 α-particle self-absorption from nanoscale magnetite
This plot of α-particle counts per minute versus the total mass of a uranium coated commercial magnetite sample, demonstrates significant α-particle self-absorption at approximately 35 mg.

Taken together, this work illustrates the three distinct advantages of using highly crystalline, non-aggregated nanocrystals for uranium collection and detection. First, the high surface area to volume ratios of the materials coupled with favorable enthalpic interactions between uranium and iron oxide allow for large sorption capacities.[49] Our 30 wt% sorption capacity (pH 5) is significantly higher than other materials used for uranium sorption.[26, 32, 197] This characteristic permits a higher degree of concentration from a number of dilute starting matrices, and provides more resistance to competing ions that block surface sorption sites. We note that our maximum sorption capacities show that 10 mg of isolated nanocrystalline

iron oxide can remove 4.28 mg of uranium from a sample (Figure 7.8). As an example, this is more than enough material to treat one liter of a 1 ppm solution of uranium.

Second, the controlled size and magnetic properties of the nanocrystalline iron oxide allow for low energy, highly efficient, and magnetically specific aqueous separations. Physical filtration removed more than 98.9% of the iron in the sample; a 48 hour magnetic separation with a handheld magnet was comparably efficient and removed 93% of the iron in the sample. For iron oxide materials with diameters below 11 nm the magnetic moment is significantly less, leading to less efficient separations.[18] Simultaneous material optimization for both sorption and magnetic separation in water is best achieved within a range of 10 to 12 nm diameter.[18] Finally, these uranyl-loaded materials remain isolated in solution and during separation, concentrate to form dense films under a micron in thickness. As a result, α-particles emitted from only micrograms of uranium can be effectively detected from the entire thickness of the film because of the minimization of self-shielding.

The ultimate impact of nanocrystal collectors for uranium analysis and remediation will depend on whether the concentration factors remain high under more realistic water and soil conditions. Environmental samples contain interfering constituents (natural organic matter, ions, etc) and solid phases that could, in principle, affect the concentration factors. As a starting point for evaluating these issues, we considered the concentration of uranium from sand, ground, and surface water samples. When uranyl salt was extracted from a pure sand matrix with 1 % HNO_3, >99.5 % of the dissolved uranium was recovered with nanocrystalline iron oxides after adjusting the pH to 5. Aqueous samples derived from surface (Braes Bayou) and ground (280 feet, gulf coast region, Richmond, TX) waters collected from in and around Houston, TX were spiked with uranyl nitrate and then acidified

with HNO_3 (evolving interfering carbonates). Separation efficiencies of 75 % (for a 7.5 ppb uranium spike) for a local surface water sample, and 86 % (4.9 ppb uranium spike) for the ground water sample could be achieved using the laboratory synthesized material. These data compare well to the 99 % (4.8 ppb uranium spike) uranium recovery for the control (Millipore® water, 18.2 Ω, 0.22 μm) using oleic acid stabilized nanocrystals (50 mg/L). The concentration factors for these more dilute and environmentally relevant samples ranged from 15,000 to almost 20,000, which are comparable to those reported in Figure 7.8. Such concentration factors, coupled with the ability to optimize solid state scintillation counting, suggest it would be possible to analyze and reclaim dilute (> 1 ppb) uranium in diverse water and soil media. Moreover, this approach should be applicable to other radionuclides that have strong interactions with iron oxide interfaces.

7.4 Conclusion

The data presented here demonstrates a complete process for the detection and remediation of uranium from complex environmental matrices. For soil contamination, 1 % HNO_3 effectively removes uranyl ions which can then be adsorbed onto nanoscale iron oxides. Homogeneous, well-dispersed magnetite nanocrystals can bind up to 30 wt% uranium, outperforming the commercial magnetite by an order of magnitude. The uranyl-magnetite complex can be magnetically or physically separated from the contaminated aqueous solution. For laboratory studies, magnetic separation provides preliminary preparation for ICP analysis. To perform in the field investigation, filtration creates a thin film of uranium coated magnetite that can be analyzed using an α-particle detector. The oleic acid coated magnetite creates uniform films that improve the sensitivity of α-particle

detection over the commercial magnetite by 1,000 times, primarily due to the improved film formation. The entire process could be feasible with minimal equipment making it potentially field deployable.

CHAPTER 8: URANIUM ADSORPTION CHEMISTRY AT THE nMAG SURFACE

8.1 Introduction

Heavy metals, such as uranium, exist as regulated contaminants of drinking water in many areas across the world.[64] Due to the adverse health effects of heavy metal exposure, many technologies have been explored to perform remediation of harmful contaminants, including biomineralization,[198] adsorption,[73] and in-situ permeable reactive barriers.[199] In particular, iron oxides have received significant attention due to their high sorption capacities for transition and actinide metals.[34, 177-179] Nanoscale iron oxides provide a promising material for the remediation of heavy metals due to their large surface area to volume ratio and their magnetic properties in the presence of an external magnetic field.[33] While significant effort has been invested into developing iron oxides as a material for the remediation of heavy metals, optimization of this new technology is paramount. The purpose of this research is to fundamentally understand how uranium is binding to the surface of the engineered nanoscale iron oxides under various conditions relevant to material optimization.

Understanding how uranium interacts with nMAG is of vital importance to improving nMAG as part of a water purification system. By understanding the nature of the surface chemistry, the sorption efficiency of the nMAG can be optimized. In this chapter, several questions about the interaction between uranium and nMAG are investigated. Binding between the uranium and both the magnetite and surrounding organic stabilizing agents will be explored. Additionally, detailed information will be provided about the nature of how uranium binds to the iron oxide surface.

8.2 Experimental Methods

8.2.1 Instrumentation

The nanoscale iron oxides were imaged by a 2100 JEOL Field Emission Gun Transmission Electron Microscope (FEG-TEM) operated at 200 kV. Probe sonication for phase transfer was performed with a Branson Digital Sonifier. An Oxford Energy Dispersive Spectrometer (EDS) backscatter detector, used for elemental analysis, was incorporated with the FEG-TEM and was used to determine if uranium is bound to the nMAG system. A Beckman Coulter Optima™ XL-A Analytical Ultracentrifuge was used to analyze density differences in uranium loaded magnetite. The instrumentation utilized to determine if the uranium binds to the iron oxide or to the organic stabilizing agents include a Renishaw inVia Raman Microscope, and a SPEX FluoroLog-3 Spectrofluorometer with UV-Vis. The instrumentation utilized to determine how the uranium binds to the iron oxide was a PHI Quantera XPS X-ray Photoelectron Spectrometer (XPS).

8.2.2 Materials

The required materials for the nMAG synthesis, including FeO(OH) (Iron(III) Oxide, hydrated; catalyst grade, 30-50 mesh; cat. #371254), oleic acid (90% technical grade), and 1-octadecene (90% technical grade), were purchased from Sigma-Aldrich. Hexanes (certified ACS grade) were purchased from Fisher Scientific. The Igepal CO-X series of surfactants (where X = 530, 610, 630, 660, 710, 720, 730, 850, 887, 890, 970) were obtained as samples from Rhodia. Commercially available nanoscale magnetite (Sigma-Aldrich, Iron (II,III)

oxide, nanopowder, <50 nm, 98+ %) was used as a comparison for Raman studies. Gold colloid (20 nm, BBI international) was used for surface-enhanced Raman spectroscopy.

8.2.3 Synthesis and Preparation of Magnetite Nanocrystals

Fe_3O_4 nanocrystals were produced by a one-pot synthesis taking as seen in Yu et al.[22] A mixture of 20.02 g FeO(OH), 255g oleic acid, and 1 L 1-octadecene were heated with stirring at 320°C for two hours. The Fe_3O_4 nanocrystals were then purified several times by flocculation in acetone, sedimentation by centrifugation, and redispersion in a minimal amount of hexanes. Nanoparticles were then made water-soluble by adding 50 mL Fe_3O_4 nanocrystals in hexanes to separate 200 mL 0.1 M solutions of each of the Igepal CO-X series (where X = 530, 610, 630, 660, 710, 720, 730, 850, 887, 890, 970). Each sample was then shaken and probe sonicated for 10 minutes. The samples were left to settle for 5 days and then centrifuged twice at 4150 rpm for 1 hour, removing excess surfactant from the top and sedimented aggregates from the bottom of the solution. The nanoparticle suspensions were then centrifuged twice at 30,000 rpm for 2 hours, decanting excess surfactant in water and retaining the settled nMAG, redispersing in water. Finally the solutions were then centrifuged at 4150 rpm for 10 minutes, discarding the pellet of aggregates at the bottom. The final 10.84 nm magnetite samples were analyzed by FEG-TEM (Figure 8.1) and DLS (Figure 8.2).

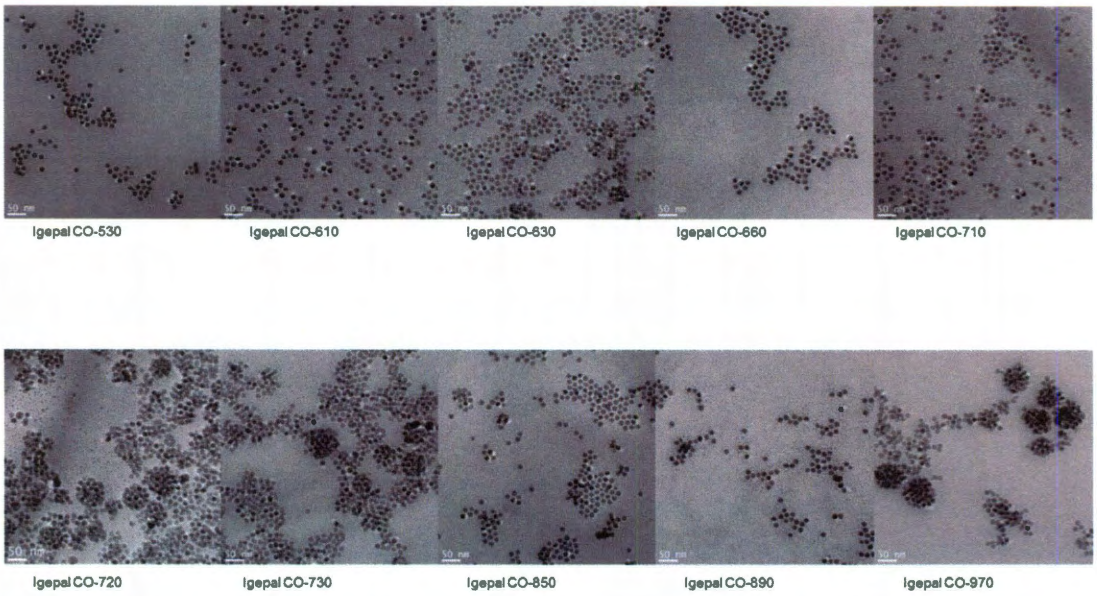

Figure 8.1 FEG-TEM images of magnetite nanoparticles coated with the Igepal CO-series

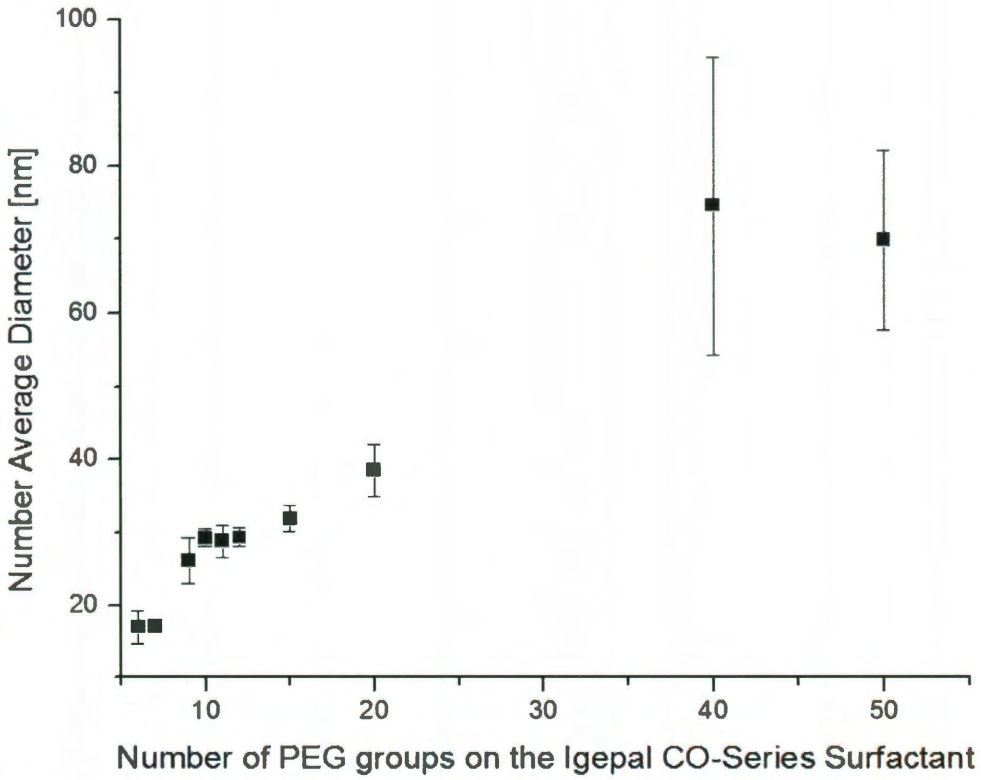

Figure 8.2 DLS results from magnetite nanoparticles coated with the Igepal CO-series

8.2.4 Uranium Adsorption Study Utilizing Igepal CO-series Surfactants

In methods similar to those previously described,[18, 27, 33] uranyl sorption isotherms were characterized for the 10.84 nm magnetite systems coated with the Igepal CO-X series of surfactants (where X = 530, 610, 630, 660, 710, 720, 730, 850, 890, 970). The sorption behavior of these laboratory prepared iron oxide nanomaterials was compared by adding them to aqueous solutions containing various uranium concentrations at pH 5 and allowing adsorption to occur over 24 hours. The solution volumes were 1 mL, containing 0.1 g/L iron oxide, and the uranium concentrations in these dilute samples ranged from ~1 to 40 ppm. Upon equilibrium under oxic conditions, the suspensions were filtered and analyzed by ICP-MS to determine the amount of uranium remaining in solution. The sorption capacity, q, was then determined by dividing the amount of uranium sorbed onto the particles by the mass of the particles. All experiments were performed in triplicate.

8.2.4 Characterization of Adsorbed Uranium on nMAG

To characterize the interactions of uranium with both nMAG and the stabilizing surfactant, analysis of uranium adsorbed nMAG was performed by EDS, analytical ultracentrifugation, Raman spectroscopy, surface-enhanced Raman spectroscopy, fluorescence spectrophotometry, and XPS. To study the changes in nanoparticle density due to the adsorbed uranium on nMAG, samples were prepared for analytical ultracentrifugation by adding solutions from 1-35 ppm uranium to Igepal CO-630 coated nMAG. The nanoparticle solutions were allowed to react for 5 days while tumbling end-over-end at 4 rpm.

Aqueous solutions of uranyl nitrate are fluorescent.[200] Iron(II) is known to quench this fluorescence.[201] Using this concept, uranium solutions from ~1-35 ppm were added to

Igepal CO-630 coated nMAG and allowed to react for 5 days while tumbling end-over-end at 4 rpm. These samples were then analyzed by a fluorescence spectrometer. In this setup, the samples were excited at 337 nm and detected at 514 nm. These samples were then magnetically separated and the magnetite free solution was analyzed under similar conditions.

FEG-TEM equipped with an EDS detector can provide the elemental composition of a selected area or point within an FEG-TEM image. A sample of 0.1 g/L nMAG coated in Igepal CO-610 or Igepal CO-850 was prepared with 25 ppm uranium and allowed to adsorb for 2 weeks. This sample was then analyzed by EDS.

The Raman microscope was used to detect changes in the vibrational spectra of uranium, Igepal CO-630 and uranium, and 0.1 g/L nMAG coated with Igepal CO-630 and uranium, in an effort to better understand the binding of uranium to the nMAG. Solutions of 25 ppm uranium were combined individually with water, 1 % Igepal CO-630, and Igepal CO-630 coated nMAG. These solutions were allowed to react for 1 month while tumbling end-over-end at 4 rpm and then deposited on a quartz slide that contained 20 nm gold colloid to improve the signal of the low concentration samples by surface-enhanced Raman spectroscopy with the 785 nm laser.

The Raman microscope was also used to compare the vibrational spectrum of uranium in either Igepal CO-630 or 18-crown-6. Solutions of 10 g/L uranium were made individually in 42.4 mM Igepal CO-630 or 18-crown-6, allowed to react for 4 weeks, and then deposited on a quartz slide for analysis by the Raman microscope with the 785 nm laser.

To quantify the oxidation state of the uranium bound to both the nMAG and stabilizing surfactant, a sample of 0.1 g/L magnetite coated in Igepal CO-610 was prepared in

50 ppm uranium and was deposited on a gold coated silicon wafer. XPS was also used to compare the oxidation states of uranium in either Igepal CO-630 or 18-crown-6. Solutions of 25 ppm uranium solutions were combined individually with 42.4 mM Igepal CO-630 or 18-crown-6 and were allowed to react for 1 month before being deposited on a silicon wafer sputter coated with gold for XPS analysis.

8.3 Results and Discussion

While it is known that the uranyl ion has a strong affinity for iron oxides,[34] and previous work has shown binding of uranyl to nanoscale magnetite,[75] it is also possible that the uranyl interacts strongly with the polyethylene glycol (PEG) chains of the nMAG stabilizing surfactant. Uranyl readily complexes with 4-6 donor oxygens in the equatorial plane,[200] and studies have shown that PEG chains more than 5 units long form an inclusion complex similar to a crown ether by wrapping around the uranyl ion.[202] All of the Igepal surfactants used here contain PEG chains longer than this (Table 8.1). To further examine the nature of the interactions of uranium with the nanoparticle-surfactant complex, several studies were performed.

Table 8.1 Langmuir isotherm quality of fit for uranium adsorption isotherms

Igepal CO-	# PEG	q max [umol/g]	Standard Error	Reduced Chi-Sqr	Adj. R-Square
530	6	242.19	8.93	0.01757	0.99969
610	7	76.81	14.73	1.13092	0.84925
630	9	306.88	60.19	1.12202	0.93231
660	10	145.97	24.98	0.23588	0.91828
710	11	196.22	54.50	0.58254	0.88508
720	12	147.87	6.97	0.39373	0.99227
730	15	452.16	227.33	1.04448	0.92771
850	20	618.74	83.36	1.17499	0.98557
890	40	379.80	152.12	6.62283	0.86428
970	50	178.06	44.80	1.76196	0.81121

First, to confirm that the uranium is binding to the iron oxide nanoparticle system, analytical ultracentrifugation was performed. Analytical ultracentrifugation is an excellent tool for determining the density of nanoparticles through their sedimentation coefficients.[124] This concept was utilized to determine the density of a series of nMAG samples exposed to various uranium concentrations in a fashion similar to those seen in adsorption experiments.[33, 75] Due to the significantly greater density of uranium over iron, if the uranium is associating with the nanoparticle (binding to the nanoparticle surface or surfactant) rather than simply precipitating out by itself, then the uranium adsorbed on the nMAG should increase with density. Analysis by analytical ultracentrifugation demonstrates that the sedimentation coefficient increases with increased uranium, implying that the uranium is associated with the nMAG-surfactant system (Figure 8.3).

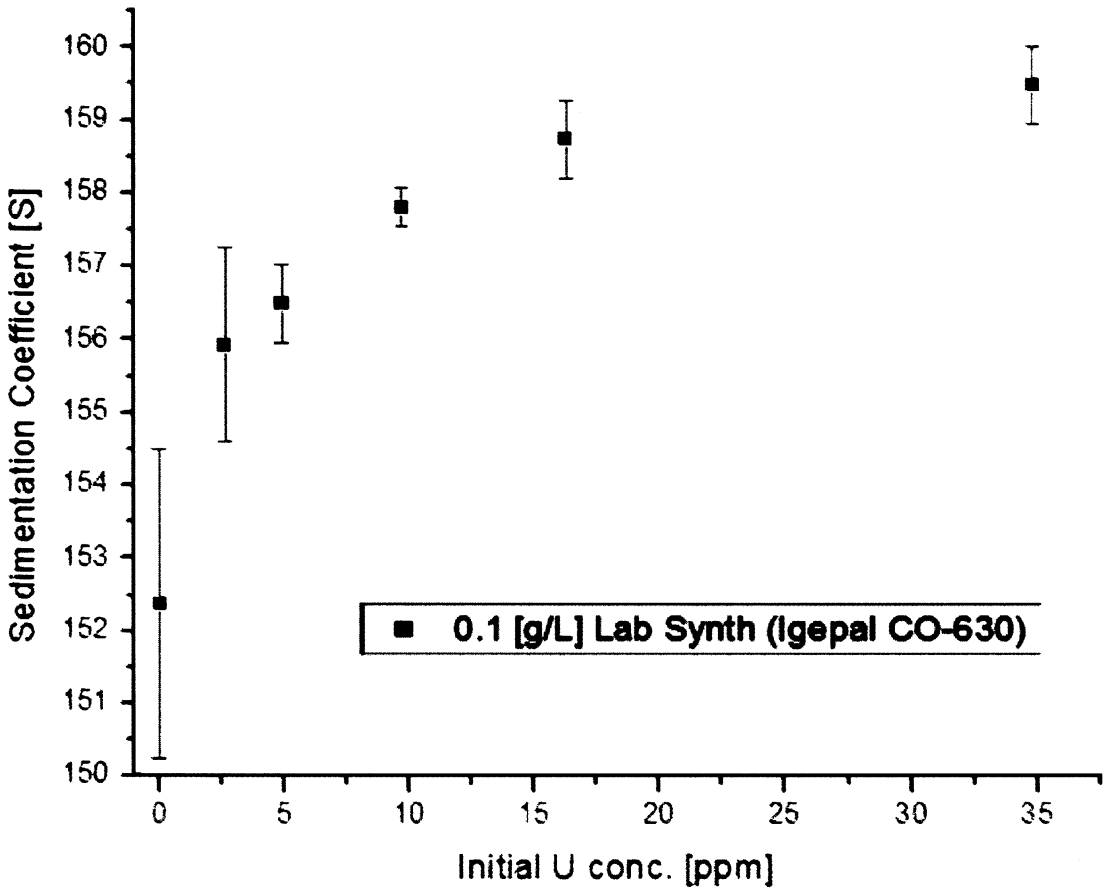

Figure 8.3 Analytical ultracentrifugation of uranium coated nMAG stabilized by Igepal CO-630
The increase in sedimentation with uranium concentration indicates that the nMAG system has become more dense due to the physical association of uranium.

One method of determining whether the uranium is binding to the nMAG is fluorescence spectrophotometry. Aqueous solutions of uranyl nitrate are fluorescent.[200] Iron(II) is known to quench this fluorescence.[201] This concept was utilized to determine the fluorescence of a series of nMAG samples exposed to various uranium concentrations in a fashion similar to those seen in previous adsorption experiments.[33, 75] Analysis by the fluorescence spectrometer demonstrates that adsorption of uranium onto nMAG quenches the fluorescence of the uranium (Figure 8.4). At the lower initial concentrations of uranium, the fluorescence was completely quenched, indicating that all of the uranium was adsorbed onto the nMAG. In contrast, there was some fluorescence at the higher uranium concentrations

where the nMAG was not adsorbing all of the uranium. The magnetite was removed magnetically and analyzed again under similar situations to observe the free uranium in solution (Figure 8.5). The free uranium was separated magnetically and the uranium concentration was determined by ICP-MS. The solution continues to fluoresce, suggesting that the fluorescence comes from the free uranium in while the fluorescence quenches by a quantity relative to that of uranium adsorbed by the nMAG. This offers further proof that uranium is associating with the iron oxide surface.

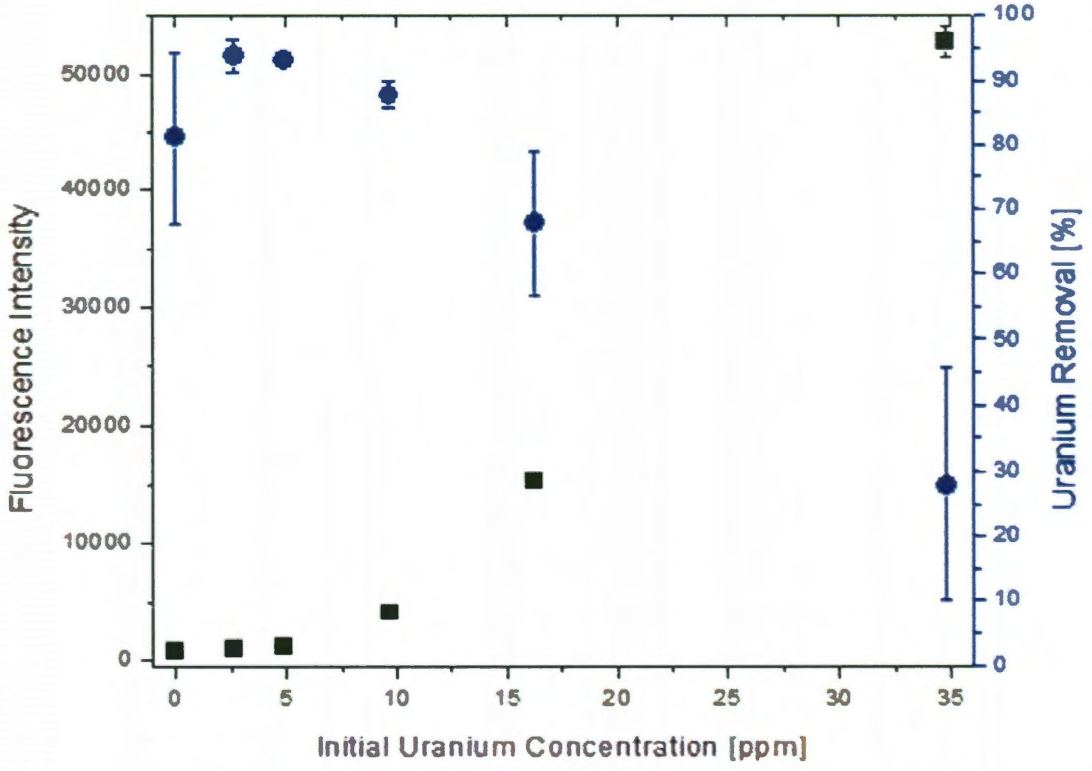

Figure 8.4 Fluorescence effected by the adsorption of uranium onto nMAG
Initially, at lower concentrations the fluorescence is quenched, but as the uranium removal percentage drops due to higher uranium concentrations, the fluorescence intensity increases. Indicating that the uranium fluorescence is quenched when associated with the nMAG.

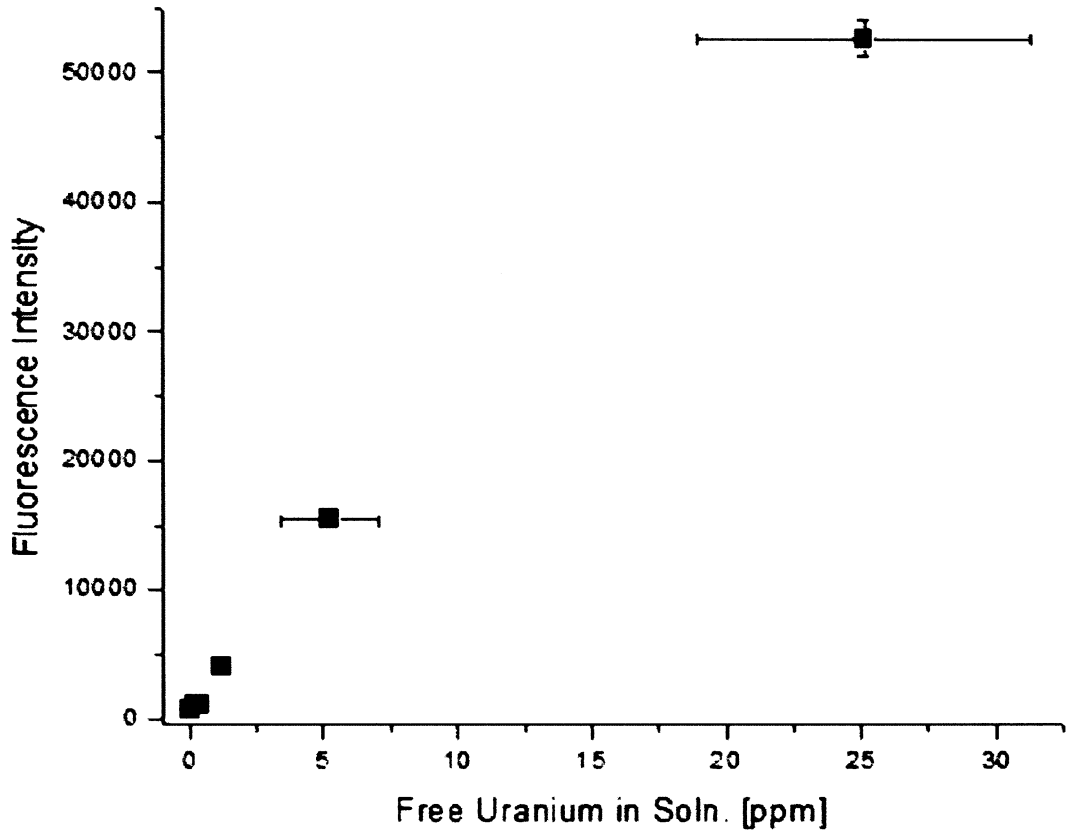

Figure 8.5 Fluorescence intensity of the unbound uranium
The fluorescence of free uranium increases linearly with concentration indicating that the uranium fluoresces as long as it is not bound to the nMAG system.

An FEG-TEM equipped with an EDS detector is a powerful tool for elemental analysis because it can fairly accurately determine the elements present in a small selected area or a single point chosen within or around a nanoparticle. Alongside a corresponding FEG-TEM image of Igepal CO-850 coated nMAG with uranium adsorbed, an EDS elemental map was obtained and demonstrates a correlation between iron and uranium, indicating that the nMAG is associated with the uranium (Figure 8.6). Experiments were also performed with Igepal CO-610 coated magnetite with adsorbed uranium. The EDS elemental spectrum of this sample, corresponding to an area of an FEG-TEM image that contains the nanoparticles, demonstrates that carbon, iron, and uranium are prevalent and likely associated

(Figure 8.7). In another area of an FEG-TEM image that contains only excess Igepal CO-610 and no nanoparticles, an EDS elemental spectrum indicates that carbon, and uranium are prevalent and likely associated even in the absence of the iron oxide nanoparticles (Figure 8.8). While the majority of the uranium seen in the EDS elemental map appear to be associated with the magnetite nanoparticles, there are areas in which it appears the uranium is bound to free surfactant, suggesting both association with the iron oxide surface, as well as binding to the surfactant may occur. These EDS data reinforce the theory that uranyl ions bind to the Igepal surfactants as well as the magnetite nanoparticles.

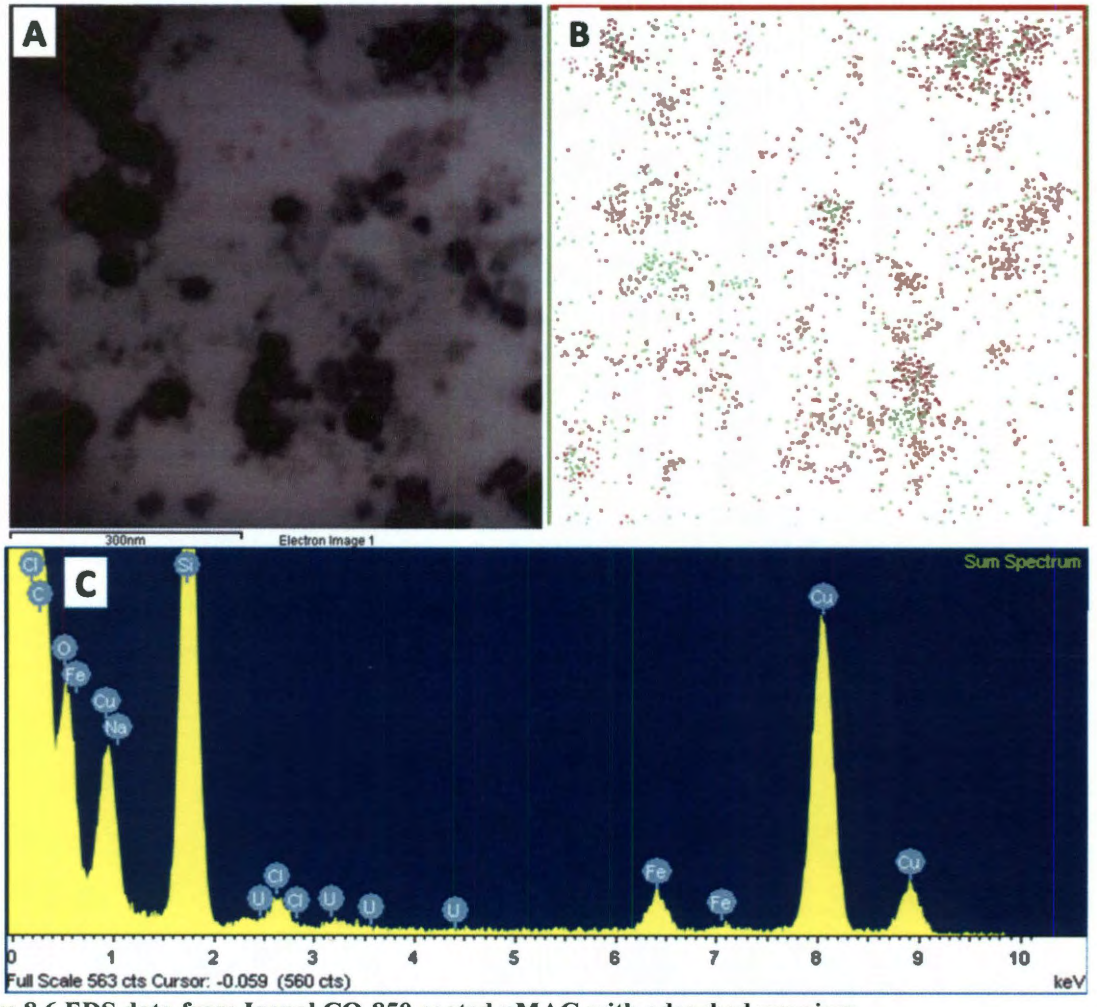

Figure 8.6 EDS data from Igepal CO-850 coated nMAG with adsorbed uranium
(A) An FEG-TEM image of the of the Igepal CO-850 stabilized nMAG is displayed along with (B) an EDS elemental map where green represents uranium and red represents iron and (C) an EDS elemental spectrum where, notably, iron, uranium, and carbon are prevalent.

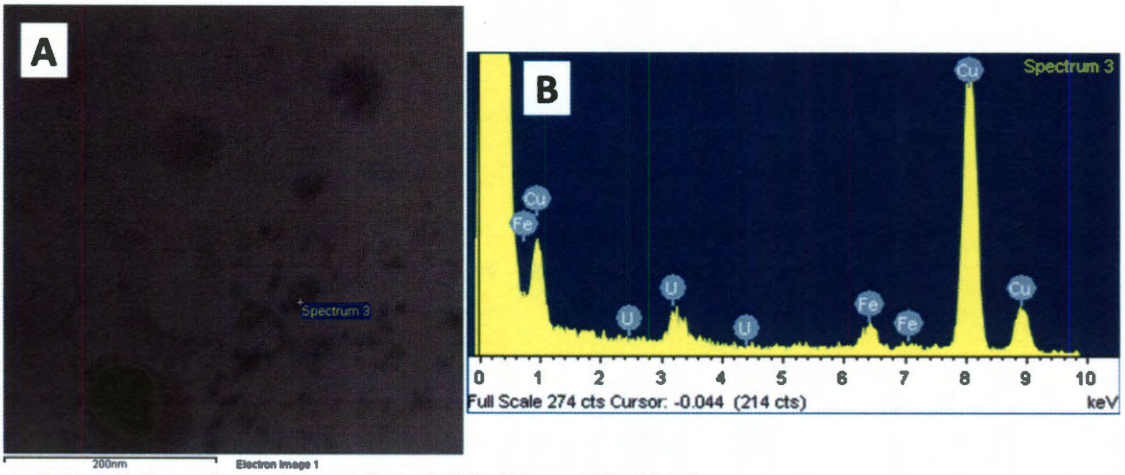

Figure 8.7 EDS data of uranium on Igepal CO-610 coated nMAG
(A) An FEG-TEM image of the of the Igepal CO-610 stabilized nMAG is displayed along with (B) an EDS elemental spectrum from a single point on a magnetite particle where, notably, iron, uranium, and carbon are prevalent.

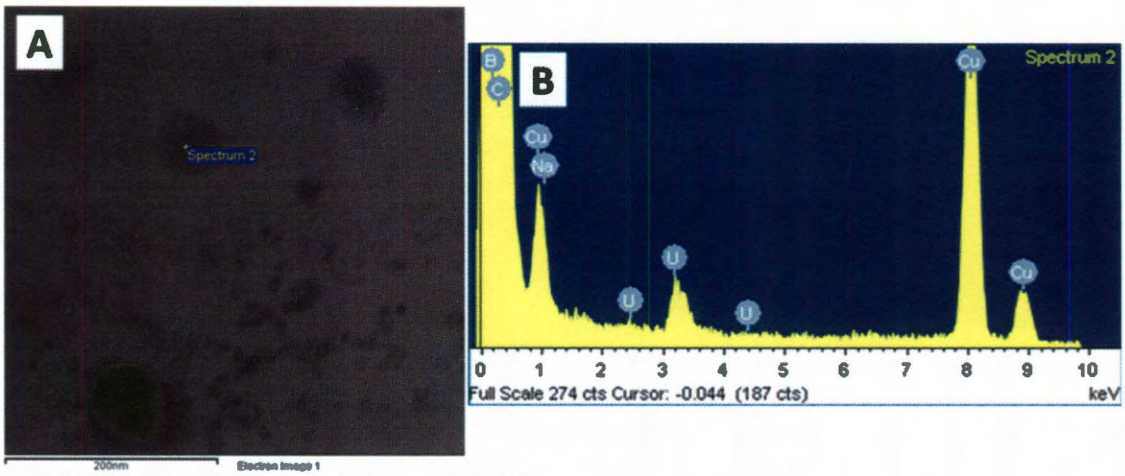

Figure 8.8 EDS data of uranium on Igepal CO-610
(A) An FEG-TEM image of the of the Igepal CO-610 stabilized nMAG is displayed along with (B) an EDS elemental spectrum from a single point on a deposition of excess free Igepal CO-610 where, notably, uranium, and carbon are prevalent, but iron is not.

Uranyl sorption isotherms were characterized for nanoscale magnetite systems coated with the Igepal CO-X series of surfactants (where X = 530, 610, 630, 660, 710, 720, 730, 850, 890, 970). The sorption behavior of these laboratory prepared iron oxide nanomaterials were compared by ICP-MS analysis to determine the amount of uranium adsorbed onto the magnetite. The sorption capacity, q, was then determined by dividing the amount of uranium sorbed onto the particles by the mass of the particles. From this data, uranium adsorption

isotherms were created for each material type (Figure 8.9). To further understand the adsorption of uranium on magnetite, a comparison to the Langmuir isotherm was performed. All adsorption isotherm data were represented by the Langmuir isotherm equation:

Equation 8.1

$$q = \frac{b \times q^{max} \times C}{(1 + b \times C)}$$

where b is the sorption constant (L/μg), q is the sorption density (μg/g), C is a constant, and q^{max} is the maximum sorption density of the solid (μg/g). The data corresponding to the quality of the Langmuir isotherm fit can be seen in Table 8.1. The maximum sorption capacity tended to increase with the surfactant PEG chain length until the two longest PEG chains (Figure 8.10). The increase in sorption capacity is potentially due to an increased number of oxygen binding sites on the PEG chain. The magnetite samples with the two longest PEG chains likely underperformed due to some aggregation. This data seems to support the binding of uranyl to the PEG components of the Igepal surfactants in addition to the nMAG binding previously established.[75]

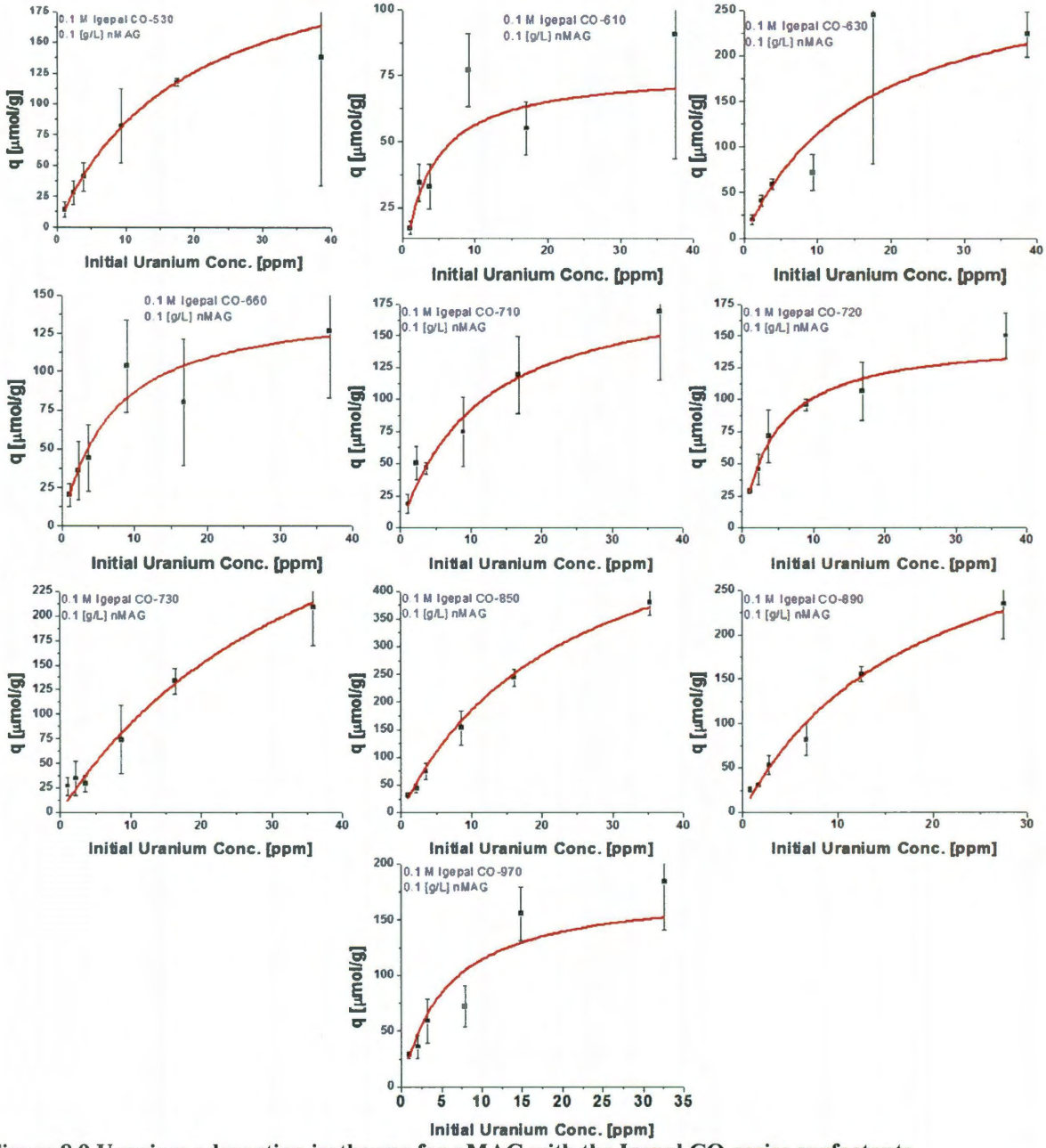

Figure 8.9 Uranium adsorption isotherms for nMAG with the Igepal CO-series surfactants
Laboratory prepared magnetite nanoparticles coated with the Igepal CO-X series of surfactants (where X = 530, 610, 630, 660, 710, 720, 730, 850, 887, 890, 970) were analyzed to obtain their uranium adsorption isotherms.

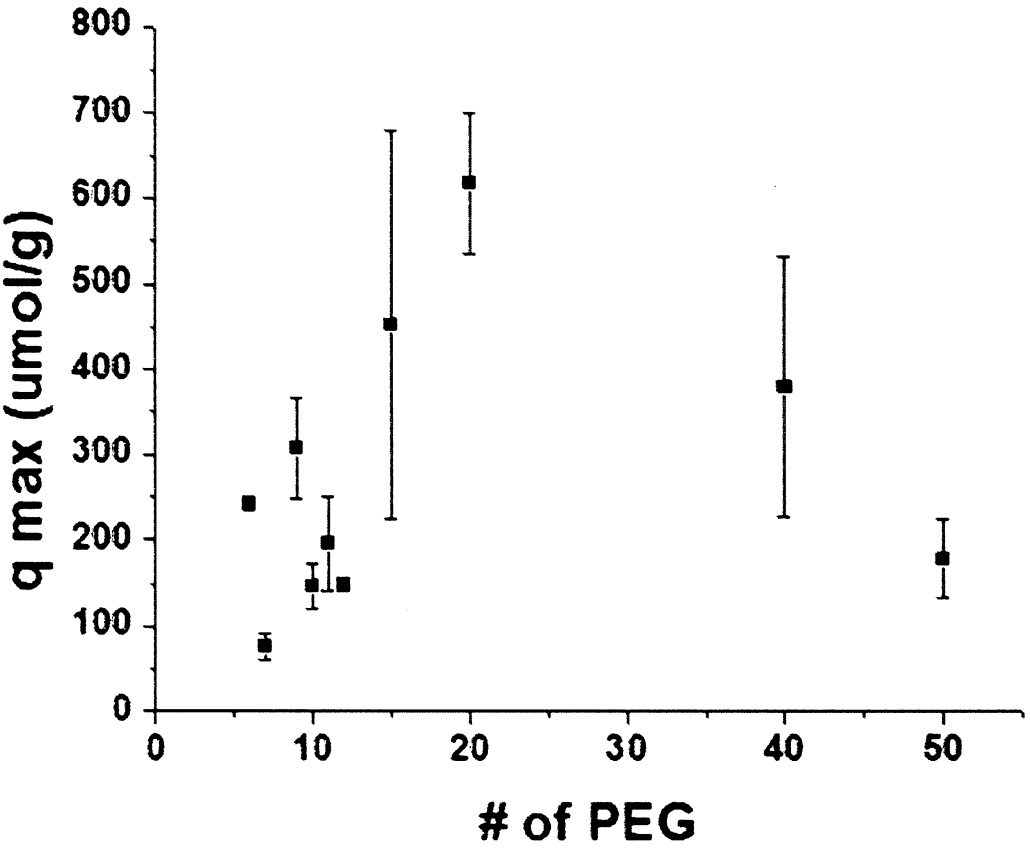

Figure 8.10 Maximum sorption capacities for magnetite coated with the Igepal CO-series of surfactants The maximum sorption capacities tend to increase with PEG chain length except for the two longest. This increase is potentially due to uranyl binding to the oxygens in the PEG component of the Igepal surfactants. The longest two PEG chains did not perform as well and was likely caused by the aggregation that these materials began to experience.

The Raman microscope was used to detect changes in the vibrational spectrum of uranium, Igepal CO-630 with uranium, and Igepal CO-630 coated nMAG with uranium in an effort to better understand the binding of uranium to the nMAG. If similar energies for (uranium), and (uranium, igepal) are observed, but a different energy for (uranium, Igepal-nMAG) is observed, then the uranium must be binding to the nMAG. If similar energies for (uranium, Igepal-nMAG), and (uranium, Igepal) are observed, but a different energy for (uranium) is observed, then the uranium must be binding to the Igepal (Figure 8.11).

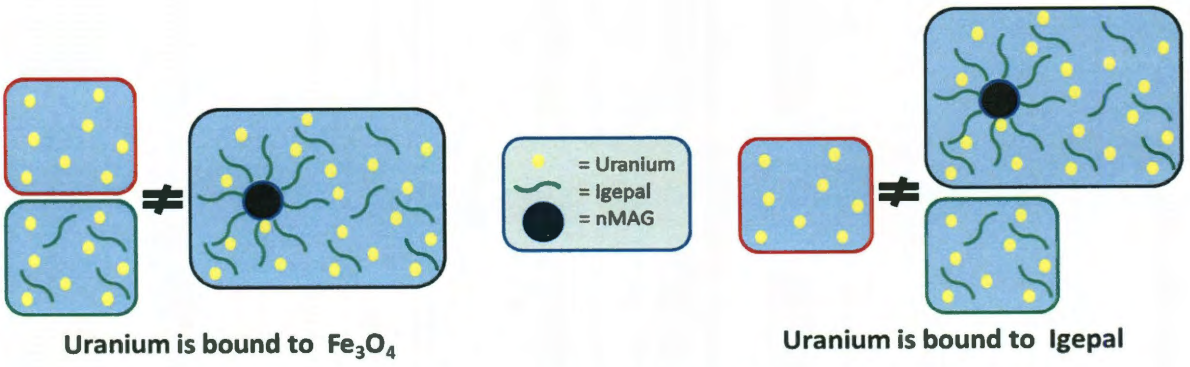

Figure 8.11 Vibrational spectroscopy theory on determining the binding nature of uranium

From the Raman microscope data (Figure 8.12), uranyl nitrate and uranyl nitrate adsorbed on commercial magnetite with no surfactant both exhibit a peak at 833 cm^{-1} corresponding to the UO_2^{2+} symmetrical stretching.[202-207] Uranyl nitrate in Igepal CO-630 and uranyl nitrate in Igepal CO-630 coated laboratory synthesized magnetite exhibit a strong, new peak shifted 13 cm^{-1} to 846 cm^{-1} corresponding to surfactant induced shift of the UO_2^{2+} symmetrical stretching. The uranyl nitrate in Igepal CO-630 coated laboratory synthesized magnetite also exhibits some of the 833 cm^{-1} peak. The fact that the shifted peak is only observed for uranyl in the presence of Igepal CO-630, either free or coating the magnetite, indicates that the Igepal is binding to the uranium. It has been shown that PEG chains, which is a component of Igepal, can equatorially wrap around a uranyl ion, forming an inclusion complex, and can shift the symmetrical stretching peak.[202] The commercial magnetite with no surfactants is known to adsorb the uranium,[75] but does not significantly shift the uranyl Raman peak. It is possible that the binding of uranyl to the iron oxide surface does not significantly affect the symmetrical stretching vibrational mode in relation to the more encompassing Igepal interaction. The Igepal CO-630 coated magnetite contains both peaks, indicating that the uranium is binding to both the iron oxide surface and the Igepal CO-630 surfactant.

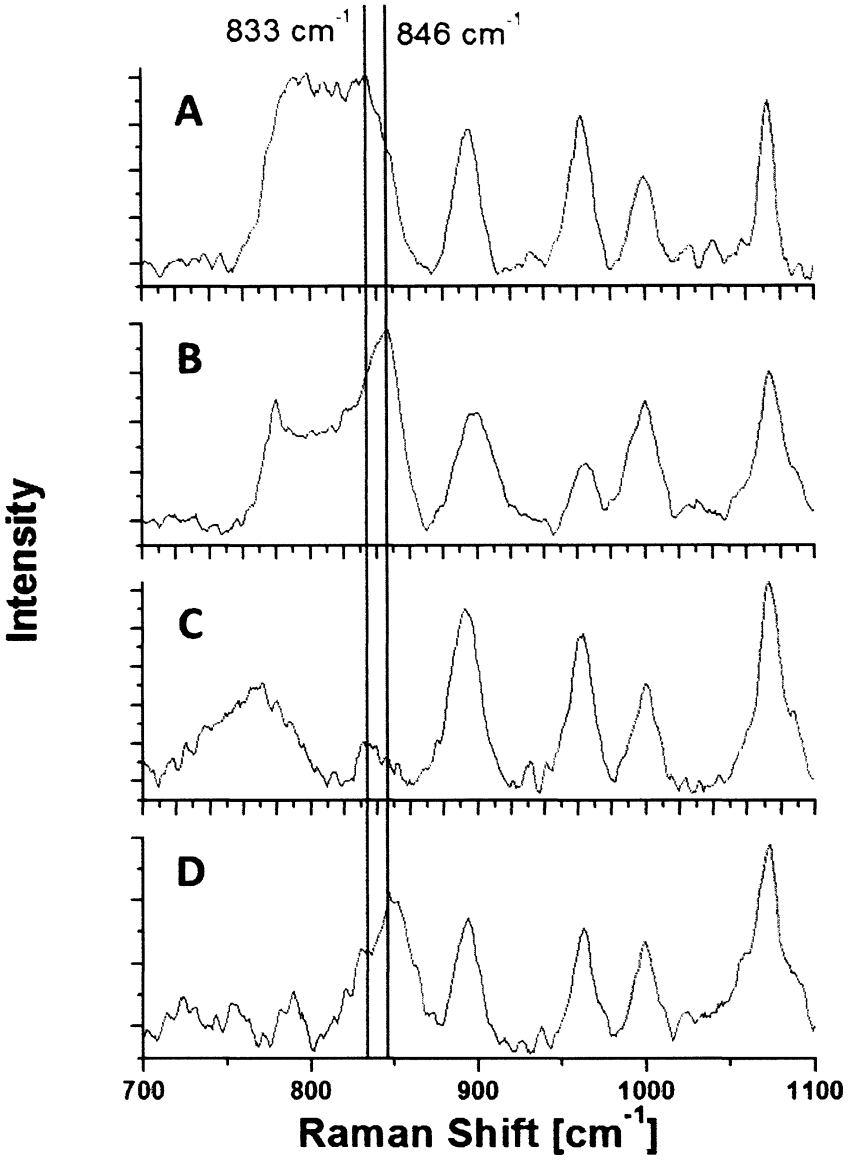

Figure 8.12 Raman spectra of uranyl interactions with magnetite and Igepal CO-630
(A) Uranyl adsorbed on commercial magnetite with no surfactant and (C) uranyl nitrate exhibit a Raman peak at 833 cm^{-1} corresponding to the UO_2^{2+} symmetrical stretching. (B) Uranyl nitrate in Igepal CO-630 and (D) uranyl nitrate in Igepal CO-630 coated laboratory synthesized magnetite exhibit a strong, new peak shifted 13 cm^{-1} to 846 cm^{-1} corresponding to surfactant induced shift of the UO_2^{2+} symmetrical stretching. The uranyl nitrate in Igepal CO-630 coated laboratory synthesized magnetite still exhibits some of the 833cm^{-1} peak.

Assuming that the uranium is binding to the surfactant, the Raman microscope was also used to compare the vibrational spectra of uranium in Igepal CO-630 or 18-crown-6. Due to the fact that uranium can complex with 4 to 6 donor oxygens in the equatorial plane,[200] such as can be provided in a crown ether, a comparison of uranium-bound crown

ether to uranium bound Igepal can demonstrate similarities in the structure of the two complexes. By wrapping the PEG chain of the Igepal surfactant around uranium, a similar structure to a crown ether could be formed. From the Raman data (Figure 8.13), the UO_2^{2+} symmetrical stretching peak shifted from 840 cm^{-1} when complexed with 18-crown-6 to 863 cm^{-1} when complexed with Igepal CO-630. It is reasonable that both 18-crown-6 and Igepal CO-630 can both shift this Raman peak because of the inclusive nature of the complex that alters the molecular symmetry.[202] The peak for uranyl and Igepal CO-630 does not match exactly with the peak in Figure 8.12 likely because of different pH conditions. The shoulder of the 863 cm^{-1} 18-crown-6 peak suggests that occasionally, the crown ether does not fully encompass the uranyl ion, creating similar conditions to the binding of the uranyl and Igepal. From this data, it can be inferred that the Igepal does wrap around the uranyl, but perhaps not in such a complete inclusive complex as a crown ether.

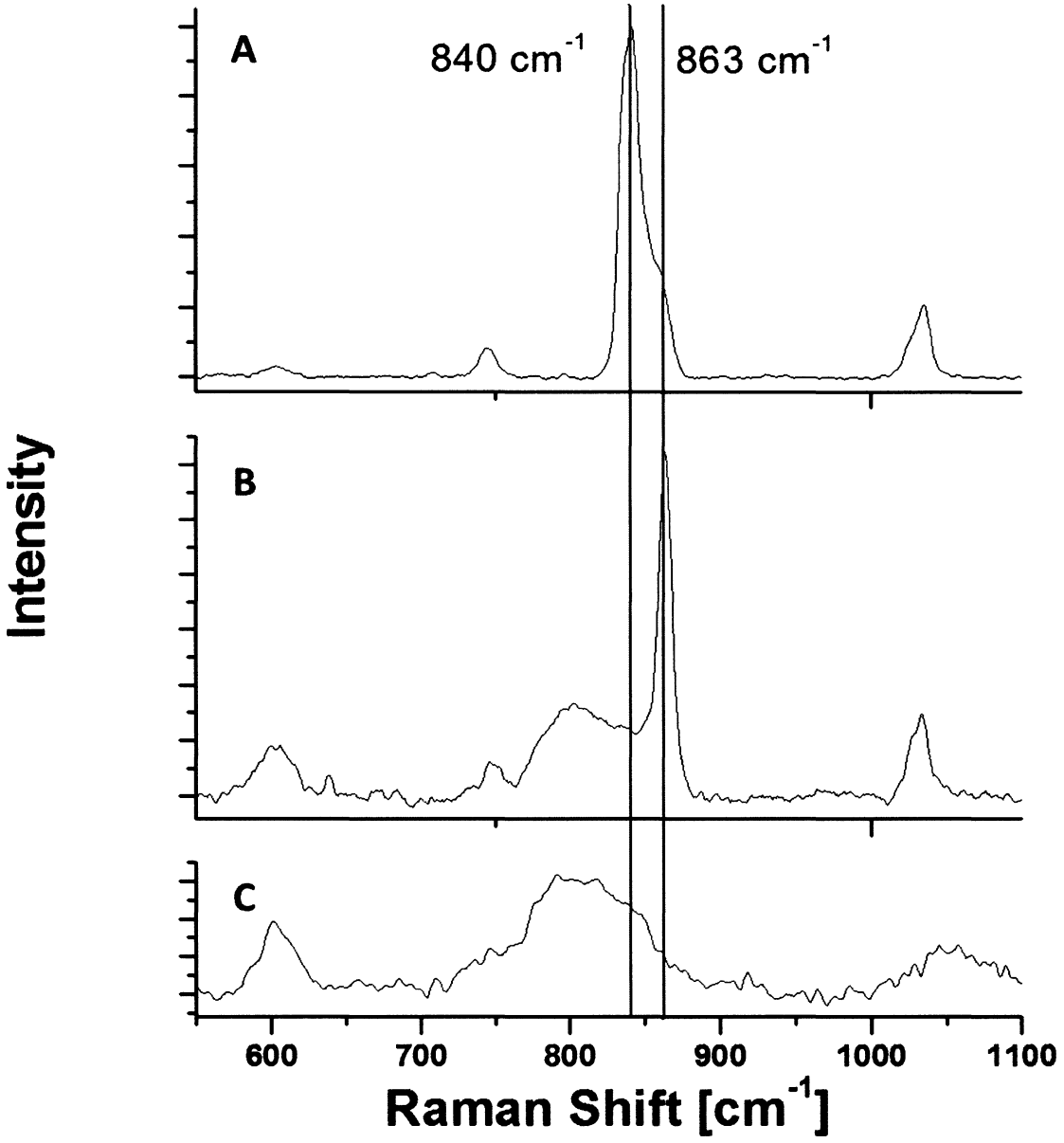

Figure 8.13 Raman spectra of uranyl interactions with 18-crown-6 and Igepal CO-630
Uranyl nitrate in (A) 18-crown-6 and (B) Igepal CO-630 were analyzed by a Raman microscope. The UO_2^{2+} symmetrical stretching peak shifted from 840 cm^{-1} when complexed with 18-crown-6 to 863 cm^{-1} when complexed with Igepal CO-630. (C) No UO_2^{2+} symmetrical stretching peak on the blank slide.

Finally, XPS was also used to compare the oxidation states of uranium in water, Igepal CO-630, or 18-crown-6, along with Igepal CO-610 coated nMAG. This data gave very clear results that indicate uranium undergoes at least a partial reduction of U^{6+} to U^{4+} when allowed to react with Igepal CO-630, 18-crown-6, or Igepal coated nMAG but not when in water alone under similar conditions (Figure 8.14). The partial reduction of uranium

from U^{6+} to U^{4+} in the presence of surfactant alone again suggests at least some of the uranium binding occurs with the Igepal surfactant. The overall slight shift in binding energy of the Igepal coated nMAG sample indicates that some uranium must be bound to the iron oxide surface as well.

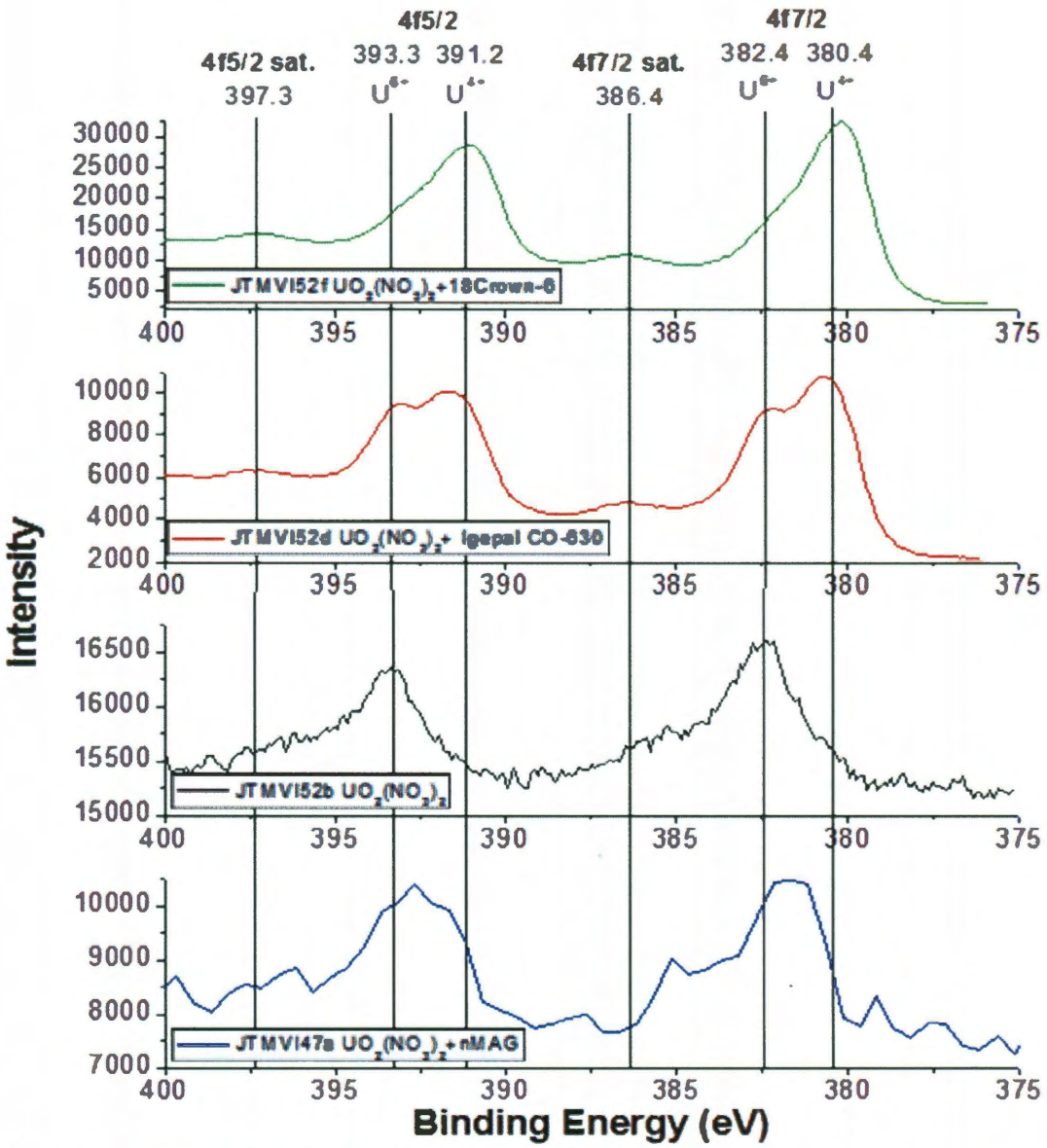

Figure 8.14 Magnetite and surfactant effect on uranium oxidation state
The aqueous solution of uranyl nitrate primarily retained its oxidation state of U^{6+} while Igepal CO-630 and 18-crown-6 solutions under similar conditions demonstrated a partial reduction of U^{6+} to U^{4+}. Igepal coated magnetite also seems to undergo partial reduction of uranium to U^{4+} but the binding energy is slightly shifted.

8.4 Conclusion

The analyses demonstrated here present a strong argument that the uranyl ion does not only adsorb to iron oxide surfaces but to PEG containing surfactants like Igepal as well. The increased sedimentation coefficients for uranium-complexed nMAG indicate a general association of uranium with the nanoparticle-surfactant system. Fluorescence spectroscopy, XPS, and EDS additional evidence was found that the uranyl associates with the iron oxide surface. Through a surfactant study of adsorption isotherms, Raman spectroscopy, XPS, and EDS were able to provide evidence that the uranyl associates with the Igepal surfactant. It was previously known that uranium could bind with iron oxides.[34] Here, a strong argument is presented that the uranyl ion can also bind to the Igepal surfactant. This may be useful in improving the adsorption efficiency of nanoparticles used in remediation applications. Magnetite nanoparticles have been shown to be an excellent material for purification of environmental contamination. The understanding of these nanoparticles as an engineered material can greatly improve their effectiveness in this and other applications.

REFERENCES

1. Cornell, R. M.; Schwertmann, U., *The Iron Oxides: Structure, Properties, Reactions, Occurrences and Uses*. WILEY-VCH: Weinheim, 2003.
2. Anthony, J. W., *Handbook of mineralogy: Halides, hydroxides, oxides*. Mineral Data Pub.: 1997.
3. Harrison, R. J.; Dunin-Borkowski, R. E.; Putnis, A., Direct imaging of nanoscale magnetic interactions in minerals. *Proc. Natl. Acad. Sci. U. S. A.* 2002, 99, 16556-16561.
4. Ceballos, S. F.; Mariotto, G.; Murphy, S.; Shvets, I. V., Fabrication of magnetic STM probes and their application to studies of the Fe3O4(001) surface. *Surface Science* 2003, 523, 131-140.
5. Mills, A. A., The lodestone: History, physics, and formation. *Ann. Sci.* 2004, 61, 273-319.
6. Maher, B. A.; Taylor, R. M., Formation of Ultrafine-Grained Magnetite in Soils. *Nature* 1988, 336, 368-370.
7. Gahlan, H. A.; Arai, S.; Ahmed, A. H.; Ishida, Y.; Abdel-Aziz, Y. M.; Rahimi, A., Origin of magnetite veins in serpentinite from the Late Proterozoic Bou-Azzer ophiolite, Anti-Atlas, Morocco: An implication for mobility of iron during serpentinization. *J. Afr. Earth Sci.* 2006, 46, 318-330.
8. Blakemore, R., Magnetotactic Bacteria. *Science* 1975, 190, 377-379.
9. Frankel, R. B.; Blakemore, R. P.; Wolfe, R. S., Magnetite in Freshwater Magnetotactic Bacteria. *Science* 1979, 203, 1355-1356.
10. Gould, J. L.; Kirschvink, J. L.; Deffeyes, K. S., Bees Have Magnetic Remanence. *Science* 1978, 201, 1026-1028.
11. Walcott, C.; Gould, J. L.; Kirschvink, J. L., Pigeons Have Magnets. *Science* 1979, 205, 1027-1029.
12. Baker, R. R.; Mather, J. G.; Kennaugh, J. H., Magnetic Bones in Human Sinuses. *Nature* 1983, 301, 78-80.
13. Guisbiers, G., Size-Dependent Materials Properties Toward a Universal Equation. *Nanoscale Research Letters* 2010, 5, 1132-1136.
14. Awschalom, D. D.; Divincenzo, D. P., COMPLEX DYNAMICS OF MESOSCOPIC MAGNETS. *Physics Today* 1995, 48, 43-48.
15. LesliePelecky, D. L.; Rieke, R. D., Magnetic properties of nanostructured materials. *Chemistry of Materials* 1996, 8, 1770-1783.
16. Pankhurst, Q. A.; Connolly, J.; Jones, S. K.; Dobson, J., Applications of magnetic nanoparticles in biomedicine. *Journal of Physics D-Applied Physics* 2003, 36, R167-R181.
17. Richter, H. J.; Ranjan, R. Y., Relaxation effects in thin film media and their consequences. *Journal of Magnetism and Magnetic Materials* 1999, 193, 213-219.
18. Yavuz, C. T.; Mayo, J. T.; Yu, W. W.; Prakash, A.; Falkner, J. C.; Yean, S.; Cong, L. L.; Shipley, H. J.; Kan, A.; Tomson, M.; Natelson, D.; Colvin, V. L., Low-field magnetic separation of monodisperse Fe3O4 nanocrystals. *Science* 2006, 314, 964-967.
19. Amendola, V.; Meneghetti, M.; Granozzi, G.; Agnoli, S.; Polizzi, S.; Riello, P.; Boscaini, A.; Anselmi, C.; Fracasso, G.; Colombatti, M.; Innocenti, C.; Gatteschi, D.; Sangregorio, C., Top-down synthesis of multifunctional iron oxide nanoparticles for

macrophage labelling and manipulation. *Journal of Materials Chemistry* 2011, 21, 3803-3813.
20. Kang, Y. S.; Risbud, S.; Rabolt, J. F.; Stroeve, P., Synthesis and characterization of nanometer-size Fe3O4 and gamma-Fe2O3 particles. *Chemistry of Materials* 1996, 8, 2209-2211.
21. Park, J.; An, K. J.; Hwang, Y. S.; Park, J. G.; Noh, H. J.; Kim, J. Y.; Park, J. H.; Hwang, N. M.; Hyeon, T., Ultra-large-scale syntheses of monodisperse nanocrystals. *Nat. Mater.* 2004, 3, 891-895.
22. Yu, W. W.; Falkner, J. C.; Yavuz, C. T.; Colvin, V. L., Synthesis of monodisperse iron oxide nanocrystals by thermal decomposition of iron carboxylate salts. *Chem. Commun.* 2004, 2306-2307.
23. Das, M.; Dhak, P.; Gupta, S.; Mishra, D.; Maiti, T. K.; Basak, A.; Pramanik, P., Highly biocompatible and water-dispersible, amine functionalized magnetite nanoparticles, prepared by a low temperature, air-assisted polyol process: a new platform for bio-separation and diagnostics. *Nanotechnology* 2010, 21.
24. Prakash, A.; Zhu, H. G.; Jones, C. J.; Benoit, D. N.; Ellsworth, A. Z.; Bryant, E. L.; Colvin, V. L., Bilayers as Phase Transfer Agents for Nanocrystals Prepared in Nonpolar Solvents. *Acs Nano* 2009, 3, 2139-2146.
25. Ramirez, L. P.; Landfester, K., Magnetic polystyrene nanoparticles with a high magnetite content obtained by miniemulsion processes. *Macromol. Chem. Phys.* 2003, 204, 22-31.
26. Shuibo, X.; Chun, Z.; Xinghuo, Z.; Jing, Y.; Xiaojian, Z.; Jingsong, W., Removal of uranium (VI) from aqueous solution by adsorption of hematite. *J. Environ. Radioact.* 2009, 100, 162-166.
27. Yean, S.; Cong, L.; Yavuz, C. T.; Mayo, J. T.; Yu, W. W.; Kan, A. T.; Colvin, V. L.; Tomson, M. B., Effect of magnetite particle size on adsorption and desorption of arsenite and arsenate. *J. Mater. Res.* 2005, 20, 3255-3264.
28. Bissen, M.; Frimmel, F. H., Arsenic - a review. - Part 1: Occurrence, toxicity, speciation, mobility. *Acta Hydrochim. Hydrobiol.* 2003, 31, 9-18.
29. Technical Report on Technologically Enhanced Naturally Occurring Radioactive Materials from Uranium Mining Volume 1: Mining and Reclamation Background. Environmental Protection Agency: 2008; Vol. EPA 402-R-08-005.
30. Hossain, M. A.; Sengupta, M. K.; Ahamed, S.; Rahman, M. M.; Mondal, D.; Lodh, D.; Das, B.; Nayak, B.; Roy, B. K.; Mukherjee, A.; Chakraborti, D., Ineffectiveness and poor reliability of arsenic removal plants in West Bengal, India. *Environ. Sci. Technol.* 2005, 39, 4300-4306.
31. Twidwell, L. G.; McCloskey, J.; Miranda, P.; Gale, M., *Technologies and potential technologies for removing arsenic from process and mine wastewater*. Warrendale, PA, 1999; p 1715-1726.
32. Zeng, H.; Singh, A.; Basak, S.; Ulrich, K. U.; Sahu, M.; Biswas, P.; Catalano, J. G.; Giammar, D. E., Nanoscale Size Effects on Uranium(VI) Adsorption to Hematite. *Environ. Sci. Technol.* 2009, 43, 1373-1378.
33. Mayo, J. T.; Yavuz, C.; Yean, S.; Cong, L.; Shipley, H.; Yu, W.; Falkner, J.; Kan, A.; Tomson, M.; Colvin, V. L., The effect of nanocrystalline magnetite size on arsenic removal. *Sci. Technol. Adv. Mater.* 2007, 8, 71-75.

34. Walter, M.; Arnold, T.; Reich, T.; Bernhard, G., Sorption of uranium(VI) onto ferric oxides in sulfate-rich acid waters. *Environ. Sci. Technol.* 2003, 37, 2898-2904.
35. El Aamrani, S.; Gimenez, J.; Rovira, M.; Seco, F.; Grive, M.; Bruno, J.; Duro, L.; de Pablo, J., A spectroscopic study of uranium(VI) interaction with magnetite. *Appl. Surf. Sci.* 2007, 253, 8794-8797.
36. Fendorf, S.; Eick, M. J.; Grossl, P.; Sparks, D. L., Arsenate and chromate retention mechanisms on goethite .1. Surface structure. *Environ. Sci. Technol.* 1997, 31, 315-320.
37. Ding, Y.; Haskel, D.; Ovchinnikov, S. G.; Tseng, Y.-C.; Orlov, Y. S.; Lang, J. C.; Mao, H.-k., Novel pressure-induced magnetic transition in magnetite (Fe(3)O(4)). *Physical Review Letters* 2008, 100.
38. Thornton, S. T.; Rex, A. F., *Modern Physics for Scientists and Engineers*. 3rd ed.; Thomson, Brooks/Cole: 2006.
39. Atkins, P. W.; Paula, J. D., *Physical Chemistry*. 7th ed.; W.H. Freeman: New York, 2002.
40. Qin, J.; Laurent, S.; Jo, Y. S.; Roch, A.; Mikhaylova, M.; Bhujwalla, Z. M.; Muller, R. N.; Muhammed, M., A high-performance magnetic resonance imaging T-2 contrast agent. *Adv. Mater.* 2007, 19, 1874-1878.
41. Hoare, T.; Santamaria, J.; Goya, G. F.; Irusta, S.; Lin, D.; Lau, S.; Padera, R.; Langer, R.; Kohane, D. S., A Magnetically Triggered Composite Membrane for On-Demand Drug Delivery. *Nano Letters* 2009, 9, 3651-3657.
42. Zhang, H. Y.; Lee, M. Y.; Hogg, M. G.; Dordick, J. S.; Sharfstein, S. T., Gene Delivery in Three-Dimensional Cell Cultures by Superparamagnetic Nanoparticles. *ACS Nano* 2010, 4, 4733-4743.
43. Hyeon, T., Chemical synthesis of magnetic nanoparticles. *Chem. Commun.* 2003, 927-934.
44. Ross, C., Patterned magnetic recording media. *Annual Review of Materials Research* 2001, 31, 203-235.
45. Yavuz, C. T.; Prakash, A.; Mayo, J. T.; Colvin, V. L., Magnetic separations: From steel plants to biotechnology. *Chemical Engineering Science* 2009, 64, 2510-2521.
46. Lee, W.; Batchelor, B., Abiotic reductive dechlorination of chlorinated ethylenes by iron-bearing soil minerals. 1. Pyrite and magnetite. *Environ. Sci. Technol.* 2002, 36, 5147-5154.
47. Liang, X. M.; Philp, R. P.; Butler, E. C., Kinetic and isotope analyses of tetrachloroethylene and trichloroethylene degradation by model Fe(II)-bearing minerals. *Chemosphere* 2009, 75, 63-69.
48. Katsumata, H.; Kaneco, S.; Inomata, K.; Itoh, K.; Funasaka, K.; Masuyama, K.; Suzuki, T.; Ohta, K., Removal of heavy metals in rinsing wastewater from plating factory by adsorption with economical viable materials. *Journal of Environmental Management* 2003, 69, 187-191.
49. Missana, T.; Maffiotte, U.; Garcia-Gutierrez, M., Surface reactions kinetics between nanocrystalline magnetite and uranyl. *J. Colloid Interface Sci.* 2003, 261, 154-160.
50. Hirschbein, B. L.; Brown, D. W.; Whitesides, G. M., MAGNETIC SEPARATIONS IN CHEMISTRY AND BIOCHEMISTRY. *Chemtech* 1982, 12, 172-179.
51. Moeser, G. D.; Roach, K. A.; Green, W. H.; Hatton, T. A.; Laibinis, P. E., High-gradient magnetic separation of coated magnetic nanoparticles. *Aiche Journal* 2004, 50, 2835-2848.

52. Hubbuch, J. J.; Matthiesen, D. B.; Hobley, T. J.; Thomas, O. R. T., High gradient magnetic separation versus expanded bed adsorption: a first principle comparison. *Bioseparation* 2001, 10, 99-112.
53. Chang, S. C.; Anderson, T. I.; Bahrman, S. E.; Gruden, C. L.; Khijniak, A. I.; Adriaens, P., Comparing recovering efficiency of immunomagnetic separation and centrifugation of mycobacteria in metalworking fluids. *Journal of Industrial Microbiology & Biotechnology* 2005, 32, 629-638.
54. Fletcher, D., FINE PARTICLE HIGH-GRADIENT MAGNETIC ENTRAPMENT. *Ieee Transactions on Magnetics* 1991, 27, 3655-3677.
55. Dunlop, D. J., SUPERPARAMAGNETIC AND SINGLE-DOMAIN THRESHOLD SIZES IN MAGNETITE. *Journal of Geophysical Research* 1973, 78, 1780-1793.
56. De Las Cuevas, G.; Faraudo, J.; Camacho, J., Low-gradient magnetophoresis through field-induced reversible aggregation. *Journal of Physical Chemistry C* 2008, 112, 945-950.
57. Ferguson, J. F.; Gavis, J., A review of the arsenic cycle in natural waters. *Water Res.* 1972, 6, 1259-1274.
58. *Arsenic in Drinking Water*; International Agency for Research on Cancer: Lyon, France, 2004; p 267.
59. EPA, National Primary Drinking Water Regulations; Arsenic and Clarifications to Compliance and New Source Contaminants Monitoring. In *40 CFR Parts 9, 141 and 142*, 2001.
60. Emsley, J., *Nature's Building Blocks*. Oxford University Press Inc.: New York, 2001.
61. Birke, M.; Rauch, U.; Lorenz, H.; Kringel, R., Distribution of uranium in German bottled and tap water. *Journal of Geochemical Exploration* 2010, 107, 272-282.
62. Kurttio, P.; Auvinen, A.; Salonen, L.; Saha, H.; Pekkanen, J.; Makelainen, I.; Vaisanen, S. B.; Penttila, I. M.; Komulainen, H., Renal effects of uranium in drinking water. *Environ. Health Perspect.* 2002, 110, 337-342.
63. Raymond-Whish, S.; Mayer, L. P.; O'Neal, T.; Martinez, A.; Sellers, M. A.; Christian, P. J.; Marion, S. L.; Begay, C.; Propper, C. R.; Hoyer, P. B.; Dyer, C. A., Drinking water with uranium below the US EPA water standard causes estrogen receptor-dependent responses in female mice. *Environ. Health Perspect.* 2007, 115, 1711-1716.
64. WHO, Guidelines for Drinking-water Quality: Third Edition Incorporating the First and Second Addenda. 3rd ed.; WHO Press: Geneva, Switzerland, 2008; Vol. 1, p 306.
65. Reimann, C.; Bjorvatn, K.; Frengstad, B.; Melaku, Z.; Tekle-Haimanot, R.; Siewers, U., Drinking water quality in the Ethiopian section of the East African Rift Valley I - data and health aspects. *Sci. Total Environ.* 2003, 311, 65-80.
66. Hristovski, K.; Westerhoff, P.; Crittenden, J., An approach for evaluating nanomaterials for use as packed bed adsorber media: A case study of arsenate removal by titanate nanofibers. *J. Hazard. Mater.* 2008, 156, 604-611.
67. Shipley, H. J.; Yean, S.; Kan, A. T.; Tomson, M. B., ADSORPTION OF ARSENIC TO MAGNETITE NANOPARTICLES: EFFECT OF PARTICLE CONCENTRATION, pH, IONIC STRENGTH, AND TEMPERATURE. *Environ. Toxicol. Chem.* 2009, 28, 509-515.
68. Shipley, H. J.; Yean, S.; Kan, A. T.; Tomson, M. B., A sorption kinetics model for arsenic adsorption to magnetite nanoparticles. *Environmental Science and Pollution Research* 2010, 17, 1053-1062.
69. Masel, R. I., *Principles of adsorption and reaction on solid surfaces*. Wiley: 1996.

70. Sheindorf, C.; Rebhun, M.; Sheintuch, M., A FREUNDLICH-TYPE MULTICOMPONENT ISOTHERM. *J. Colloid Interface Sci.* 1981, 79, 136-142.
71. Feenstra, L.; Erkel, J. v.; Vasak, L. *Arsenic in groundwater: Overview and evaluation of removal methods*; International Groundwater Resources Assessment Centre: Utrecht, The Netherlands, 2007.
72. Mohan, D.; Pittman, C. U., Arsenic removal from water/wastewater using adsorbents - A critical review. *J. Hazard. Mater.* 2007, 142, 1-53.
73. Crane, R. A.; Dickinson, M.; Popescu, I. C.; Scott, T. B., Magnetite and zero-valent iron nanoparticles for the remediation of uranium contaminated environmental water. *Water Res.* 2011, 45, 2931-2942.
74. Das, D.; Sureshkumar, M. K.; Koley, S.; Mithal, N.; Pillai, C. G. S., Sorption of uranium on magnetite nanoparticles. *J. Radioanal. Nucl. Chem.* 2010, 285, 447-454.
75. Fortner, J.; Mayo, J. T.; Prakash, A.; Lewicka, Z.; Benoit, D.; Colvin, V. L., Iron Oxide Nanoparticles for Uranium Concentration and Detection in Environmental Samples. *ACS Nano* 2011, *Under Review*.
76. Che, Y. H.; Li, Y. B.; Slavik, M.; Paul, D., Rapid detection of Salmonella typhimurium in chicken carcass wash water using an immunoelectrochemical method. *Journal of Food Protection* 2000, 63, 1043-1048.
77. Haukanes, B. I.; Kvam, C., APPLICATION OF MAGNETIC BEADS IN BIOASSAYS. *Bio-Technology* 1993, 11, 60-63.
78. Kularatne, B. Y.; Lorigan, P.; Browne, S.; Suvarna, S. K.; Smith, N. O.; Lawry, J., Monitoring tumour cells in the peripheral blood of small cell lung cancer patients. *Cytometry* 2002, 50, 160-167.
79. Levine, B. L.; Cotte, J.; Small, C. C.; Carroll, R. G.; Riley, J. L.; Bernstein, W. B.; Van Epps, D. E.; Hardwick, R. A.; June, C. H., Large-scale production of CD4+ T cells from HIV-1-infected donors after CD3/CD28 costimulation. *Journal of Hematotherapy* 1998, 7, 437-448.
80. Lui, G.; Manches, O.; Chaperot, L.; Ducrot, T.; Molens, J. P.; Sotto, J. J.; Bensa, J. C.; Plumas, J., Preparation of purified lymphoma cells suitable for therapy. *Cytotherapy* 2004, 6, 235-243.
81. Molday, R. S.; Mackenzie, D., IMMUNOSPECIFIC FERROMAGNETIC IRON-DEXTRAN REAGENTS FOR THE LABELING AND MAGNETIC SEPARATION OF CELLS. *Journal of Immunological Methods* 1982, 52, 353-367.
82. Morisada, S.; Miyata, N.; Iwahori, K., Immunomagnetic separation of scum-forming bacteria using polyclonal antibody that recognizes mycolic acids. *Journal of Microbiological Methods* 2002, 51, 141-148.
83. Mura, C. V.; Becker, M. L.; Orellana, A.; Wolff, D., Immunopurification of Golgi vesicles by magnetic sorting. *Journal of Immunological Methods* 2002, 260, 263-271.
84. Nakayasu, C.; Yoshitomi, T.; Oyamatsu, T.; Okamoto, N.; Ikeda, Y., Separation of carp (Cyprinus carpio L) thrombocytes by using a monoclonal antibody, and their aggregation by collagen. *Veterinary Immunology and Immunopathology* 1997, 57, 337-346.
85. Raghavarao, K. S. M. S.; Dueser, M.; Todd, P.; Scheper, T., Multistage magnetic and electrophoretic extraction of cells, particles and macromolecules. *Advances in Biochemical Engineering Biotechnology; New products and new areas of bioprocess engineering* 2000, 139-190.

86. Richards, A. J.; Roath, O. S.; Smith, R. J.; Watson, J. H., High purity, recovery, and selection of human blood cells with a novel high gradient magnetic separator. *J Hematother* 1996, 5, 415-26.
87. RootsWeiss, A.; Papadimitriou, C.; Serve, H.; Hoppe, B.; Koenigsmann, M.; Reufi, B.; Oberberg, D.; Thiel, E.; Berdel, W. E., The efficiency of tumor cell purging using immunomagnetic CD34(+) cell separation systems. *Bone Marrow Transplantation* 1997, 19, 1239-1246.
88. Tibbe, A. G. J.; de Grooth, B. G.; Greve, J.; Liberti, P. A.; Dolan, G. J.; Terstappen, L., Optical tracking and detection of immunomagnetically selected and aligned cells. *Nature Biotechnology* 1999, 17, 1210-1213.
89. Zigeuner, R. E.; Riesenberg, R.; Pohla, H.; Hofstetter, A.; Oberneder, R., Isolation of circulating cancer cells from whole blood by immunomagnetic cell enrichment and unenriched immunocytochemistry in vitro. *Journal of Urology* 2003, 169, 701-705.
90. Bucak, S.; Jones, D. A.; Laibinis, P. E.; Hatton, T. A., Protein separations using colloidal magnetic nanoparticles. *Biotechnol. Prog.* 2003, 19, 477-484.
91. Dunnill, P.; Lilly, M. D., PURIFICATION OF ENZYMES USING MAGNETIC BIO-AFFINITY MATERIALS. *Biotechnology and Bioengineering* 1974, 16, 987-990.
92. Franzreb, M.; Siemann-Herzberg, M.; Hobley, T. J.; Thomas, O. R. T., Protein purification using magnetic adsorbent particles. *Applied Microbiology and Biotechnology* 2006, 70, 505-516.
93. Halling, P. J.; Dunnill, P., MAGNETIC SUPPORTS FOR IMMOBILIZED ENZYMES AND BIOAFFINITY ADSORBENTS. *Enzyme and Microbial Technology* 1980, 2, 2-10.
94. Heeboll-Nielsen, A.; Choe, W. S.; Middelberg, A. P. J.; Thomas, O. R. T., Efficient inclusion body processing using chemical extraction and high gradient magnetic fishing. *Biotechnol. Prog.* 2003, 19, 887-898.
95. Heeboll-Nielsen, A.; Dalkiaer, M.; Hubbuch, J. J.; Thomas, O. R. T., Superparamagnetic adsorbents for high-gradient magnetic fishing of lectins out of legume extracts. *Biotechnology and Bioengineering* 2004, 87, 311-323.
96. Heeboll-Nielsen, A.; Justesen, S. F. L.; Hobley, T. J.; Thomas, O. R. T., Superparamagnetic cation-exchange adsorbents for bioproduct recovery from crude process liquors by high-gradient magnetic fishing. *Sep. Sci. Technol.* 2004, 39, 2891-2914.
97. Holschuh, K.; Schwammle, A., Preparative purification of antibodies with protein A - an alternative to conventional chromatography. *Journal of Magnetism and Magnetic Materials* 2005, 293, 345-348.
98. Hubbuch, J. J.; Thomas, O. R. T., High-gradient magnetic affinity separation of trypsin from porcine pancreatin. *Biotechnology and Bioengineering* 2002, 79, 301-313.
99. Khng, H. P.; Cunliffe, D.; Davies, S.; Turner, N. A.; Vulfson, E. N., The synthesis of sub-micron magnetic particles and their use for preparative purification of proteins. *Biotechnology and Bioengineering* 1998, 60, 419-424.
100. Lai, J. J.; Nelson, K. E.; Nash, M. A.; Hoffman, A. S.; Yager, P.; Stayton, P. S., Dynamic bioprocessing and microfluidic transport control with smart magnetic nanoparticles in laminar-flow devices. *Lab on a Chip* 2009, 9, 1997-2002.
101. Liao, M. H.; Chen, D. H., Fast and efficient adsorption/desorption of protein by a novel magnetic nano-adsorbent. *Biotechnol. Lett.* 2002, 24, 1913-1917.

102. Liu, X. Q.; Guan, Y. P.; Liu, H. Z.; Ma, Z. Y.; Yang, Y.; Wu, X. B., Preparation and characterization of magnetic polymer nanospheres with high protein binding capacity. *Journal of Magnetism and Magnetic Materials* 2005, 293, 111-118.
103. Ma, Z. Y.; Guan, Y. P.; Liu, H. Z., Synthesis of monodisperse nonporous crosslinked poly(glycidyl methacrylate) particles with metal affinity ligands for protein adsorption. *Polym. Int.* 2005, 54, 1502-1507.
104. Meyer, A.; Hansen, D. B.; Gomes, C. S. G.; Hobley, T. J.; Thomas, O. R. T.; Franzreb, M., Demonstration of a strategy for product purification by high-gradient magnetic fishing: Recovery of superoxide dismutase from unconditioned whey. *Biotechnol. Prog.* 2005, 21, 244-254.
105. O'brien, S. M.; Sloane, R. P.; Thomas, O. R. T.; Dunnill, P., Characterisation of non-porous magnetic chelator supports and their use to recover polyhistidine-tailed T4 lysozyme from a crude E-coli extract. *J. Biotechnol.* 1997, 54, 53-67.
106. O'brien, S. M.; Thomas, O. R. T.; Dunnill, P., Non-porous magnetic chelator supports for protein recovery by immobilised metal affinity adsorption. *J. Biotechnol.* 1996, 50, 13-25.
107. Peng, Z. G.; Hidajat, K.; Uddin, M. S., Adsorption and desorption of lysozyme on nano-sized magnetic particles and its conformational changes. *Colloid Surf. B-Biointerfaces* 2004, 35, 169-174.
108. Robinson, P. J.; Dunnill, P.; Lilly, M. D., PROPERTIES OF MAGNETIC SUPPORTS IN RELATION TO IMMOBILIZED ENZYME REACTORS. *Biotechnology and Bioengineering* 1973, 15, 603-606.
109. Tong, X. D.; Xue, B.; Sun, Y., A novel magnetic affinity support for protein adsorption and purification. *Biotechnol. Prog.* 2001, 17, 134-139.
110. Yang, C. L.; Liu, H. Z.; Guan, Y. P.; Xing, J. M.; Liu, J. G.; Shan, G. B., Preparation of magnetic poly(methylmethacrylate-divinylbenzene-glycidylmethacrylate) microspheres by spraying suspension polymerization and their use for protein adsorption. *Journal of Magnetism and Magnetic Materials* 2005, 293, 187-192.
111. Chen, H. T.; Kaminski, M. D.; Liu, X. Q.; Mertz, C. J.; Xie, Y. M.; Torno, M. D.; Rosengart, A. J., A novel human detoxification system based on nanoscale bioengineering and magnetic separation techniques. *Medical Hypotheses* 2007, 68, 1071-1079.
112. Qu, L. H.; Peng, X. G., Control of photoluminescence properties of CdSe nanocrystals in growth. *Journal of the American Chemical Society* 2002, 124, 2049-2055.
113. Nacci, A.; Cioffi, N., Special Issue: Nano-Catalysts and Nano-Technologies for Green Organic Synthesis. *Molecules* 2011, 16, 1452-1453.
114. Rao, C. N. R.; Cheetham, A. K., Science and technology of nanomaterials: current status and future prospects. *Journal of Materials Chemistry* 2001, 11, 2887-2894.
115. Buschow, K. H. J., *Handbook of Magnetic Materials*. Elsevier: 2006.
116. Peng, X. G.; Manna, L.; Yang, W. D.; Wickham, J.; Scher, E.; Kadavanich, A.; Alivisatos, A. P., Shape control of CdSe nanocrystals. *Nature* 2000, 404, 59-61.
117. Peng, X. G.; Wickham, J.; Alivisatos, A. P., Kinetics of II-VI and III-V colloidal semiconductor nanocrystal growth: "Focusing" of size distributions. *Journal of the American Chemical Society* 1998, 120, 5343-5344.
118. Peng, Z. A.; Peng, X. G., Formation of high-quality CdTe, CdSe, and CdS nanocrystals using CdO as precursor. *Journal of the American Chemical Society* 2001, 123, 183-184.

119. Peng, Z. A.; Peng, X. G., Nearly monodisperse and shape-controlled CdSe nanocrystals via alternative routes: Nucleation and growth. *Journal of the American Chemical Society* 2002, 124, 3343-3353.
120. Qu, L. H.; Peng, Z. A.; Peng, X. G., Alternative routes toward high quality CdSe nanocrystals. *Nano Letters* 2001, 1, 333-337.
121. Qu, L. H.; Yu, W. W.; Peng, X. P., In situ observation of the nucleation and growth of CdSe nanocrystals. *Nano Letters* 2004, 4, 465-469.
122. Yu, W. W.; Peng, X. G., Formation of high-quality CdS and other II-VI semiconductor nanocrystals in noncoordinating solvents: Tunable reactivity of monomers. *Angewandte Chemie-International Edition* 2002, 41, 2368-2371.
123. Yu, W. W.; Qu, L. H.; Guo, W. Z.; Peng, X. G., Experimental determination of the extinction coefficient of CdTe, CdSe, and CdS nanocrystals. *Chemistry of Materials* 2003, 15, 2854-2860.
124. Jamison, J. A.; Krueger, K. M.; Yavuz, C. T.; Mayo, J. T.; LeCrone, D.; Redden, J. J.; Colvin, V. L., Size-Dependent Sedimentation Properties of Nanocrystals. *ACS Nano* 2008, 2, 311-319.
125. Demortiere, A.; Panissod, P.; Pichon, B. P.; Pourroy, G.; Guillon, D.; Donnio, B.; Begin-Colin, S., Size-dependent properties of magnetic iron oxide nanocrystals. *Nanoscale* 2011, 3, 225-232.
126. Ahmed, M. F.; Ahuja, S.; Alauddin, M.; Hug, S. J.; Lloyd, J. R.; Pfaff, A.; Pichler, T.; Saltikov, C.; Stute, M.; van Geen, A., Epidemiology - Ensuring safe drinking water in Bangladesh. *Science* 2006, 314, 1687-1688.
127. Bhattacharjee, Y., Toxicology - A sluggish response to humanity's biggest mass poisoning. *Science* 2007, 315, 1659-1661.
128. Asokan, S.; Krueger, K. M.; Alkhawaldeh, A.; Carreon, A. R.; Mu, Z. Z.; Colvin, V. L.; Mantzaris, N. V.; Wong, M. S., The use of heat transfer fluids in the synthesis of high-quality CdSe quantum dots, core/shell quantum dots, and quantum rods. *Nanotechnology* 2005, 16, 2000-2011.
129. Sapra, S.; Rogach, A. L.; Feldmann, J., Phosphine-free synthesis of monodisperse CdSe nanocrystals in olive oil. *Journal of Materials Chemistry* 2006, 16, 3391-3395.
130. Basu, S.; Weil, D. N., Appropriate technology and growth. *Q J Econ* 1998, 113, 1025-1054.
131. Hazeltine, B.; Bull, C., *Field guide to appropriate technology*. Academic Press: London, 2003.
132. Pursell, C., THE RISE AND FALL OF THE APPROPRIATE TECHNOLOGY MOVEMENT IN THE UNITED-STATES, 1965-1985. *Technology and Culture* 1993, 34, 629-637.
133. Schumacher, E. F., Small is beautiful : economics as if people mattered. Harper & Row: New York, 1975; Vol. P352, p 305 p.
134. Benkler, Y., *The Wealth of Networks: How Social Production Transforms Markets and Freedom*. Yale University Press: 2007.
135. Kelty, C. M., *Two bits: the cultural significance of free software*. Duke University Press: 2008.
136. Weber, S., *The success of open source*. Harvard University Press: Cambridge, MA, 2004; p viii, 312 p.

137. Bullen, C. R.; Mulvaney, P., Nucleation and growth kinetics of CdSe nanocrystals in octadecene. *Nano Letters* 2004, 4, 2303-2307.
138. http://www.sigmaaldrich.com/. (accessed July 28 2011).
139. Kim, D. K.; Zhang, Y.; Voit, W.; Rao, K. V.; Muhammed, M., Synthesis and characterization of surfactant-coated superparamagnetic monodispersed iron oxide nanoparticles. *Journal of Magnetism and Magnetic Materials* 2001, 225, 30-36.
140. Yavuz, C. T.; Mayo, J. T.; Suchecki, C.; Wang, J.; Ellsworth, A. Z.; D'Couto, H.; Quevedo, E.; Prakash, A.; Gonzalez, L.; Nguyen, C.; Kelty, C.; Colvin, V. L., Pollution magnet: nano-magnetite for arsenic removal from drinking water. *Environmental Geochemistry and Health* 2010, 32, 327-334.
141. Mattson, F. H.; Lutton, E. S., SPECIFIC DISTRIBUTION OF FATTY ACIDS IN THE GLYCERIDES OF ANIMAL AND VEGETABLE FATS. *Journal of Biological Chemistry* 1958, 233, 868-871.
142. Torres, M. M.; Maestri, D. M., The effects of genotype and extraction methods on chemical composition of virgin olive oils from Traslasierra Valley (Cordoba, Argentina). *Food Chemistry* 2006, 96, 507-511.
143. Gan, H. L.; Man, Y. B. C.; Tan, C. P.; NorAini, I.; Nazimah, S. A. H., Characterisation of vegetable oils by surface acoustic wave sensing electronic nose. *Food Chemistry* 2005, 89, 507-518.
144. Roca, A. G.; Morales, M. P.; Serna, C. J., Synthesis of monodispersed magnetite particles from different organometallic precursors. *Ieee Transactions on Magnetics* 2006, 42, 3025-3029.
145. Asami, K.; Kikuchi, M., In-depth distribution of rusts on a plain carbon steel and weathering steels exposed to coastal-industrial atmosphere for 17 years. *Corrosion Science* 2003, 45, 2671-2688.
146. Jana, N. R.; Chen, Y. F.; Peng, X. G., Size- and shape-controlled magnetic (Cr, Mn, Fe, Co, Ni) oxide nanocrystals via a simple and general approach. *Chemistry of Materials* 2004, 16, 3931-3935.
147. Yin, M.; Willis, A.; Redl, F.; Turro, N. J.; O'Brien, S. P., Influence of capping groups on the synthesis of gamma-Fe2O3 nanocrystals. *J. Mater. Res.* 2004, 19, 1208-1215.
148. Yu, W. W.; Chang, E.; Falkner, J. C.; Zhang, J. Y.; Al-Somali, A. M.; Sayes, C. M.; Johns, J.; Drezek, R.; Colvin, V. L., Forming biocompatible and nonaggregated nanocrystals in water using amphiphilic polymers. *Journal of the American Chemical Society* 2007, 129, 2871-2879.
149. Wang, C.-L.; Fang, M.; Xu, S.-H.; Cui, Y.-P., Salts-Based Size-Selective Precipitation: Toward Mass Precipitation of Aqueous Nanoparticles. *Langmuir* 2010, 26, 633-638.
150. Al-Somali, A. M.; Krueger, K. M.; Falkner, J. C.; Colvin, V. L., Recycling size exclusion chromatography for the analysis and separation of nanocrystalline gold. *Anal. Chem.* 2004, 76, 5903-5910.
151. Sweeney, S. F.; Woehrle, G. H.; Hutchison, J. E., Rapid purification and size separation of gold nanoparticles via diafiltration. *Journal of the American Chemical Society* 2006, 128, 3190-3197.
152. Liu, G. D.; Wang, J.; Kim, J.; Jan, M. R.; Collins, G. E., Electrochemical coding for multiplexed immunoassays of proteins. *Anal. Chem.* 2004, 76, 7126-7130.

153. Agrawal, A.; Sathe, T.; Nie, S. M., Single-bead immunoassays using magnetic microparticles and spectral-shifting quantum dots. *Journal of Agricultural and Food Chemistry* 2007, 55, 3778-3782.
154. Beveridge, J. S.; Stephens, J. R.; Latham, A. H.; Williams, M. E., Differential Magnetic Catch and Release: Analysis and Separation of Magnetic Nanoparticles. *Anal. Chem.* 2009, 81, 9618-9624.
155. Ditsch, A.; Lindenmann, S.; Laibinis, P. E.; Wang, D. I. C.; Hatton, T. A., High-gradient magnetic separation of magnetic nanoclusters. *Ind. Eng. Chem. Res.* 2005, 44, 6824-6836.
156. Parker, M. R., HIGH-GRADIENT MAGNETIC SEPARATION. *Physics in Technology* 1981, 12, 263-268.
157. Ma, M.; Wu, Y.; Zhou, H.; Sun, Y. K.; Zhang, Y.; Gu, N., Size dependence of specific power absorption of Fe3O4 particles in AC magnetic field. *Journal of Magnetism and Magnetic Materials* 2004, 268, 33-39.
158. Malynych, S. Z.; Tokarev, A.; Hudson, S.; Chumanov, G.; Ballato, J.; Kornev, K. G., Magneto-controlled illumination with opto-fluidics. *Journal of Magnetism and Magnetic Materials* 2010, 322, 1894-1897.
159. Butter, K.; Bomans, P. H. H.; Frederik, P. M.; Vroege, G. J.; Philipse, A. P., Direct observation of dipolar chains in iron ferrofluids by cryogenic electron microscopy. *Nat. Mater.* 2003, 2, 88-91.
160. Krass, A. S.; Boskma, P.; Elzen, B.; Smit, W. A., *Uranium Enrichment and Nuclear Weapon Proliferation.* Taylor & Francis Ltd: London, 1983.
161. Pierce, M. L.; Moore, C. B., Adsorption of Arsenite and Arsenate on Amorphous Iron Hydroxide. *Water Res.* 1982, 16, 1247-1253.
162. Raven, K. P.; Jain, A.; Loeppert, R. H., Arsenite and arsenate adsorption on ferrihydrite: Kinetics, equilibrium, and adsorption envelopes. *Environ. Sci. Technol.* 1998, 32, 344-349.
163. Manceau, A., The Mechanism of Anion Adsorption on Iron-Oxides - Evidence for the Bonding of Arsenate Tetrahedra on Free Fe(O,OH)(6) Edges. *Geochim. Cosmochim. Acta* 1995, 59, 3647-3653.
164. Waychunas, G. A.; Rea, B. A.; Fuller, C. C.; Davis, J. A., Surface-Chemistry of Ferrihydrite .1. Exafs Studies of the Geometry of Coprecipitated and Adsorbed Arsenate. *Geochim. Cosmochim. Acta* 1993, 57, 2251-2269.
165. Carabante, I.; Grahn, M.; Holmgren, A.; Kumpiene, J.; Hedlund, J., Adsorption of As (V) on iron oxide nanoparticle films studied by in situ ATR-FTIR spectroscopy. *Colloids and Surfaces a-Physicochemical and Engineering Aspects* 2009, 346, 106-113.
166. Kanel, S. R.; Manning, B.; Charlet, L.; Choi, H., Removal of arsenic(III) from groundwater by nanoscale zero-valent iron. *Environ. Sci. Technol.* 2005, 39, 1291-1298.
167. Moeser, G. D.; Roach, K. A.; Green, W. H.; Laibinis, P. E.; Hatton, T. A., Water-based magnetic fluids as extractants for synthetic organic compounds. *Ind. Eng. Chem. Res.* 2002, 41, 4739-4749.
168. EPA, Clean Water Act. EPA, Ed. 1972.
169. EPA, Uranium Mill Tailings Radiation Control Act. EPA, Ed. 1978.
170. EPA, Low-Level Radioactive Waste Policy Act. EPA, Ed. 1980.
171. EPA, Clean Air Act. Agency, E. P., Ed. US: 1990.

172. EPA, Use of Uranium Drinking Water Standards under 40 CFR 141 and 40 CFR 192 as Remediation Goals for Groundwater at CERCLA sites *CERCLA* 1999.
173. Liu, J. W.; Brown, A. K.; Meng, X. L.; Cropek, D. M.; Istok, J. D.; Watson, D. B.; Lu, Y., A catalytic beacon sensor for uranium with parts-per-trillion sensitivity and millionfold selectivity. *Proc. Natl. Acad. Sci. U. S. A.* 2007, 104, 2056-2061.
174. Peurrung, A., Material science for nuclear detection. *Materials Today* 2008, 11, 50-54.
175. Brumfiel, G., The meltdown that wasn't. *Nature* 2011, 471, 417-418.
176. Butler, D., Fukushima health risks scrutinized. *Nature* 2011, 472, 13-14.
177. Novikov, A. P.; Kalmykov, S. N.; Utsunomiya, S.; Ewing, R. C.; Horreard, F.; Merkulov, A.; Clark, S. B.; Tkachev, V. V.; Myasoedov, B. F., Colloid transport of plutonium in the far-field of the Mayak Production Association, Russia. *Science* 2006, 314, 638-641.
178. Rathore, N. S.; Pabby, A. K.; Venugopalan, A. K., Removal of actinides and fission products activity from intermediate alkaline waste using inorganic exchangers. *J. Radioanal. Nucl. Chem.* 2004, 262, 543-549.
179. Stumpf, S.; Stumpf, T.; Dardenne, K.; Hennig, C.; Foerstendorf, H.; Klenze, R.; Fanghanel, T., Sorption of Am(III) onto 6-line- ferrihydrite and its alteration products: Investigations by EXAFS. *Environ. Sci. Technol.* 2006, 40, 3522-3528.
180. Goldstein, S. J.; Stirling, C. H., Techniques for measuring uranium-series nuclides: 1992-2002. In *Uranium-Series Geochemistry*, Mineralogical Soc America: Washington, 2003; Vol. 52, pp 23-57.
181. Ku, T. L., Uranium-Series Methods of Age-Determination. *Annu Rev Earth Pl Sc* 1976, 4, 347-379.
182. Matthews, K. M.; Kim, C.-K.; Martin, P., Determination of Po-210 in environmental materials: A review of analytical methodology. *Appl. Radiat. Isot.* 2007, 65, 267-279.
183. Silberberg, M., *Chemistry: the molecular nature of matter and change*. McGraw-Hill: 2000.
184. Decarvalho, H. G.; Yagoda, H., The Range of Alpha-Particles in Water. *Phys Rev* 1952, 88, 273-278.
185. Matsumoto, S.; Kobayashi, H., A New Type Hygrometer Using a Double Ionization-Chamber with Alpha-Rays. *Nucl Instrum Meth A* 1987, 255, 290-292.
186. Barshick, C. M.; Turner, M. L.; Smith, D. H.; Patch, K. D., A fieldable instrument for waterborne radionuclide detection. *Proceedings of SPIE-The International Society for Optical Engineering* 1997, 2933, 133-142.
187. Surbeck, H., Alpha spectrometry sample preparation using selectively adsorbing thin films. *Appl. Radiat. Isot.* 2000, 53, 97-100.
188. Bojanowski, R.; Radecki, L.; Burns, K., Determination of radium and uranium isotopes in natural waters by sorption on hydrous manganese dioxide followed by alpha-spectrometry. *J. Radioanal. Nucl. Chem.* 2005, 264, 437-443.
189. Donia, A. M.; Atia, A. A.; Moussa, E. M. M.; El-Sherif, A. M.; El-Magied, M. O. A., Removal of uranium(VI) from aqueous solutions using glycidyl methacrylate chelating resins. *Hydrometallurgy* 2009, 95, 183-189.
190. Fiedor, J. N.; Bostick, W. D.; Jarabek, R. J.; Farrell, J., Understanding the mechanism of uranium removal from groundwater by zero-valent iron using X-ray photoelectron spectroscopy. *Environ. Sci. Technol.* 1998, 32, 1466-1473.

191. Moyes, L. N.; Parkman, R. H.; Charnock, J. M.; Vaughan, D. J.; Livens, F. R.; Hughes, C. R.; Braithwaite, A., Uranium uptake from aqueous solution by interaction with goethite, lepidocrocite, muscovite, and mackinawite: An X-ray absorption spectroscopy study. *Environ. Sci. Technol.* 2000, 34, 1062-1068.
192. Phenrat, T.; Saleh, N.; Sirk, K.; Kim, H. J.; Tilton, R. D.; Lowry, G. V., Stabilization of aqueous nanoscale zerovalent iron dispersions by anionic polyelectrolytes: adsorbed anionic polyelectrolyte layer properties and their effect on aggregation and sedimentation. *Journal of Nanoparticle Research* 2008, 10, 795-814.
193. Missana, T.; Garcia-Gutierrez, M.; Fernndez, V., Uranium(VI) sorption on colloidal magnetite under anoxic environment: Experimental study and surface complexation modelling. *Geochim. Cosmochim. Acta* 2003, 67, 2543-2550.
194. Terada, K., PRECONCENTRATION OF TRACE-ELEMENTS BY SORPTION. *Analytical Sciences* 1991, 7, 187-198.
195. Jiang, P.; Bertone, J. F.; Hwang, K. S.; Colvin, V. L., Single-crystal colloidal multilayers of controlled thickness. *Chemistry of Materials* 1999, 11, 2132-2140.
196. Harris, D. C., *Quantitative Chemical Analysis*. Seventh ed.; W. H. Freeman and Company: New York, 2007.
197. Yusan, S.; Akyil, S., Sorption of uranium(VI) from aqueous solutions by akaganeite. *J. Hazard. Mater.* 2008, 160, 388-395.
198. Rotter, B. E.; Barry, D. A.; Gerhard, J. I.; Small, J. S., Modeling the effectiveness of U(VI) biomineralization in dual-porosity porous media. *Journal of Hydrology* 2011, 402, 14-24.
199. Fuller, C. C.; Bargar, J. R.; Davis, J. A.; Piana, M. J., Mechanisms of uranium interactions with hydroxyapatite: Implications for groundwater remediation. *Environ. Sci. Technol.* 2002, 36, 158-165.
200. Cotton, F. A.; Wilkinson, G.; Murillo, C. A.; Bochmann, M., Advanced Inorganic Chemistry. 6th ed.; Cotton, F. A., Ed. Wiley: New York, 1999.
201. Taha, I. A.; Morawetz, H., CATALYSIS OF IONIC REACTIONS BY POLYELECTROLYTES .3. QUENCHING OF URANYL ION FLUORESCENCE BY IRON(II) IONS IN POLY(VINYLSULFONIC ACID) SOLUTION. *Journal of the American Chemical Society* 1971, 93, 829-&.
202. Servaes, K.; De Houwer, S.; Gorller-Walrand, C.; Binnemans, K., Spectroscopic properties of uranyl crown ether complexes in non-aqueous solvents. *Physical Chemistry Chemical Physics* 2004, 6, 2946-2950.
203. Bullock, J. I., RAMAN AND INFRARED SPECTROSCOPIC STUDIES OF URANYL ION - SYMMETRIC STRETCHING FREQUENCY FORCE CONSTANTS AND BOND LENGTHS. *Journal of the Chemical Society a -Inorganic Physical Theoretical* 1969, 781-&.
204. Conn, G. K. T.; Wu, C. K., An investigation of the Raman and infrared spectra of certain uranyl salts, with conclusions on the structure of the uranyl group. *Transactions of the Faraday Society* 1938, 34, 1483-1491.
205. Costes, R. M.; Folcher, G.; Keller, N.; Plurien, P.; Rigny, P., COMPLEX OF A CYCLIC POLYETHER 18 - CROWN - 6 WITH URANYL-NITRATE. *Inorganic & Nuclear Chemistry Letters* 1975, 11, 469-473.

206. Costes, R. M.; Folcher, G.; Plurien, P.; Rigny, P., NEW URANIUM AND THORIUM CROWN ETHER COMPLEXES. *Inorganic & Nuclear Chemistry Letters* 1976, 12, 13-21.
207. Maya, L.; Begun, G. M., A RAMAN-SPECTROSCOPY STUDY OF HYDROXO AND CARBONATO SPECIES OF THE URANYL(VI) ION. *Journal of Inorganic & Nuclear Chemistry* 1981, 43, 2827-2832.